5-2014

Transport Resistance in Polymer Electrolyte Fuel Cells

Jon Patrick Owejan
University of Tennessee - Knoxville, jowejan@utk.edu

To the Graduate Council:

I am submitting herewith a dissertation written by Jon Patrick Owejan entitled "Transport Resistance in Polymer Electrolyte Fuel Cells." I have examined the final electronic copy of this dissertation for form and content and recommend that it be accepted in partial fulfillment of the requirements for the degree of Doctor of Philosophy, with a major in Mechanical Engineering.

Matthew M. Mench, Major Professor

We have read this dissertation and recommend its acceptance:

Thomas A. Zawodzinski, Feng-Yuan Zhang, Dibyendu Mukherjee

Accepted for the Council:

Carolyn R. Hodges

Vice Provost and Dean of the Graduate School

(Original signatures are on file with official student records.)

Transport Resistance in Polymer Electrolyte Fuel Cells

A Dissertation Presented for the
Doctor of Philosophy
Degree
The University of Tennessee, Knoxville

Jon Patrick Owejan
May 2014

Acknowledgements

I would like to express my gratitude to my wife Jeanette for her support and guidance during my tenure in graduate school. Jeanette is a true scientist who values rigor and objective reporting of scientific results; this is just one of many ways in which she inspires me. My deepest appreciation and thanks are to my advisor Dr. Matthew Mench, who has been a tremendous mentor for me. I would like to thank Dr. Mench for enabling me to pursue this degree and encouraging my research. His advice, balanced with humility and wisdom, is invaluable to me. I would also like to thank my committee members, Dr. Zawodzinski, Dr. Zhang, and Dr. Mukherjee, for sharing their knowledge and time. I would also like to recognize a longtime mentor and friend, Dr. Thomas Trabold, for believing in me and giving me the confidence and opportunities to keep moving forward professionally. Finally I wish to thank Kathy Williams for her support and goodwill related to the many administrative issues we overcame.

The US Department of Energy is acknowledged for providing funding for this research through award DE-0000470.

Abstract

Fuel cells offer the potential for high efficiency energy conversion with only water and heat as significant products of the electrochemical reaction. For a cost-competitive product, fuel cell researchers are exploring the limits of the Pt catalyst loading in parallel with performance and durability trade-offs. A significant portion of the performance loss in low-cost PEMFCs is associated with the partial pressure of oxygen (for an air cathode) at the Pt surface. This dissertation explores the main components of oxygen transport resistance which are associated with diffusion through partially saturated porous media and the ionomer coating in the catalyst layer.

Under typical proton exchange membrane fuel cell (PEMFC) operating conditions, temperature gradients through the porous gas diffusion layer (GDL) can result in product water condensation. As a result, non-uniform partial saturation of the GDL changes the local effective porosity and tortuosity encountered by oxygen diffusing to the catalyst layer. This work establishes the impact of saturation on practical fuel cell system efficiency losses related to shutdown purge time and overall stack resistance. The transport resistance is further investigated in two-dimensions using limiting current experiments with simultaneous neutron imaging. The analysis of these data results in a diffusion coefficient vs. saturation relationship for two common GDL carbon fiber substrates.

A significant oxygen transport limitation also occurs near the Pt surface. This is investigated here with loading studies that fix electrode thickness and bulk properties. The impact of Pt dispersion is probed by varying the average distance between Pt particles. Results elucidate how the electrode structure impacts local transport loss. It is demonstrated that local transport loss is not fully captured with a normalized Pt area. Additional geometric considerations that account for ionomer surface area relative to the Pt particles are required to resolve performance loss at low Pt loading as electrode structure varies. Furthermore, within this ionomer layer an interfacial resistance at both the gas and Pt interfaces is required to account for performance trends observed. These results demonstrate that residual performance loss associated with low cathode Pt loading can be mitigated by minimizing oxygen flux through the gas/ionomer interface.

Table of Contents

List of Tables

List of Figures

1. Chapter 1 - Introduction

1.1. Energy Storage and Fuel Cells

Humans have more impact on the planet, good and bad, than all other species combined. This dominance is directly related to the technology that has been co-evolving with us. At its core, our innovation has been focused on leveraging human energy to accomplish life sustaining tasks. Over time we have made remarkable progress extracting energy and consequently have become increasing reliant on this additional energy as the fabric of our societies relies first and foremost on high-yield harvests and rapid distribution of food. Therefore, we all share in concerns that the current rate of energy consumption is not sustainable. The current energy paradigm will require significant political, social, and economic momentum to reduce the amount of energy leverage the average human has. Or perhaps, like all evolutionary processes observed to date, a deviation from the current paradigm will require an adaptation to a changing environment. This poses a most interesting challenge to humankind: Will self-awareness, rationality, and sapience drive change before the environment forces it?

The energy we seek is often misrepresented as originating from several sources, but the fact is that all energy that we know how to use results from nuclear fusion in the core of stars and there is no "alternative." Most of life on earth is supported by the sun through photosynthesis and cyclic heating of the earth's surface. The pertinent question we now face is related only to the balance of how this energy is stored relative to the rate it is consumed. The majority of our current energy commodity comes from compressed organic matter that results from millions of climatic cycles (growth seasons) and a smaller, but significant, portion that is harvested from fissile material that is created only under conditions present during the collapse of a star. In either case, our rate of energy usage is much faster than the rate of storage in these materials by any measure, even if the current rate of biomass conversion is included. Rotation of electro-mechanical generators by convection of water and air due to heating effects from solar radiation and direct photoelectric conversion are presently our main methods of sustainable conversion. Since these real-time (sustainable) energy sources only account for less than 10% of the average power consumption in the world, a means of energy storage from these conversion devices is not of an immediate need. Theoretically, any need for storage in the current electricity grid

represents waste as an effective system would simply reduce the rate of conversion of non-sustainable feedstock given that any secondary conversion has a thermodynamic penalty.

The reality is, however, that our electricity grids are poorly planned and managed so there is currently a small market for energy storage in some remote locations. On the surface this need highlights systemic issues with the quickly evolving electricity infrastructures of the world but as a convenient consequence it serves to incubate storage technologies that will be essential if sustainable conversion eventually encapsulates a majority stake of a large grid. In some areas of the world this is becoming a highly likely scenario. There are several ways of storing this excess energy, and this of course includes additional energy conversion processes. The most efficient of these is large batteries. Traditional solid-state batteries have limited capacity, but with a small amount of pump work, flow batteries can provide electric capacity only limited by volume. Other less efficient means of storage include pumping water to large reservoirs (most common), and compressing air in large containment vessels. Thermal storage of solar radiation in high heat capacity materials requires no energy conversion; however, its efficiency loss is realized later when electricity is generated by a heat engine.

All these means of storage will rely on the grid of electric transmission lines to consume them because they are large and stationary. However, if the storage means were portable, its marketability and value is significantly increased. The main reason for this is the demand from the transportation sector for portable stored energy. This creates a unique niche for the final method to store sustainable energy, in hydrogen, by various methods involving energy input to water. Hydrogen is already in high demand for many industrial processes and its internal energy can be extracted by chemical or electrochemical reactions with low associated activation energy. For all intents and purposes, hydrogen is a suitable alternative to gasoline for onboard combustion. Moreover, for energy conversion of hydrogen outside the limitations of the Carnot cycle, a fuel cell operating near ambient pressure offers leading efficiency by most measures for transportation power plants. Low temperature fuel cells are of particular interest for transportation because of their high power density and low startup energy. These fuel cells are typically characterized by the polymer electrolyte used, hence polymer electrolyte fuel cells (PEFCs).

The polymer electrolyte both enables and constrains PEFCs. When wet, its high ionic conductivity at low operating temperatures enables high efficiency operation, but this requires additional water input and moderation of the maximum operating temperature such that the polymer doesn't get damaged. The main consequences of PEFCs are that a noble metal catalyst is required to move the electrochemical reactions forward at low temperature with minimal overpotential and large heat exchangers are

required due to small temperature differentials with respect to the ambient. Even considering these tradeoffs, hydrogen fed PEFCs are universally chosen in industry for first-generation light duty transportation applications. Moreover, taking into account the thermodynamic losses associated with hydrolysis or stream reforming and the compression of hydrogen, the high conversion efficiency of current PEFC systems results in a competitive well-to-wheels analysis relative to energy conversion by combustion. However, a combined analysis of performance, cost, and durability of practical systems reveals the current obstacles to significant market penetration [1]. As a result, PEFC research requires a balanced approach to understand the complex interplay of physical and chemical phenomena which need to be characterized, quantified, and theoretically modeled to advance the technology in an effective manner.

It is now well understood that fuel cell performance, durability, and cost are closely linked to the presence of liquid water, which is the product of the electrochemical reaction. Figure 1.1 depicts the relevant fuel cell length scales, nominal pore sizes of each component, and their respective surface properties. Aside from the proton-conducting membrane, the materials must be porous so that gas transport to the catalyst can occur. This catalyst layer must be thin to assure a short diffusion length, thus allowing for high catalyst utilization. The additional porous layers are required in part for transport of reactant gas around the electron conducting lands of the flow distributor channels. The bulk material of this layer is typically carbon fiber paper. An additional microporous layer (MPL) must be applied between the catalyst layer and the carbon fiber paper (or gas diffusion layer, GDL) for optimal fuel cell performance. The thermal resistance of these layers can impose a significant temperature gradient from the cathode electrode to the gas channels as heat generated at the catalyst layer is dissipated by liquid coolant in the flow distribution plates and carried out with the exiting reactant flow mixture.

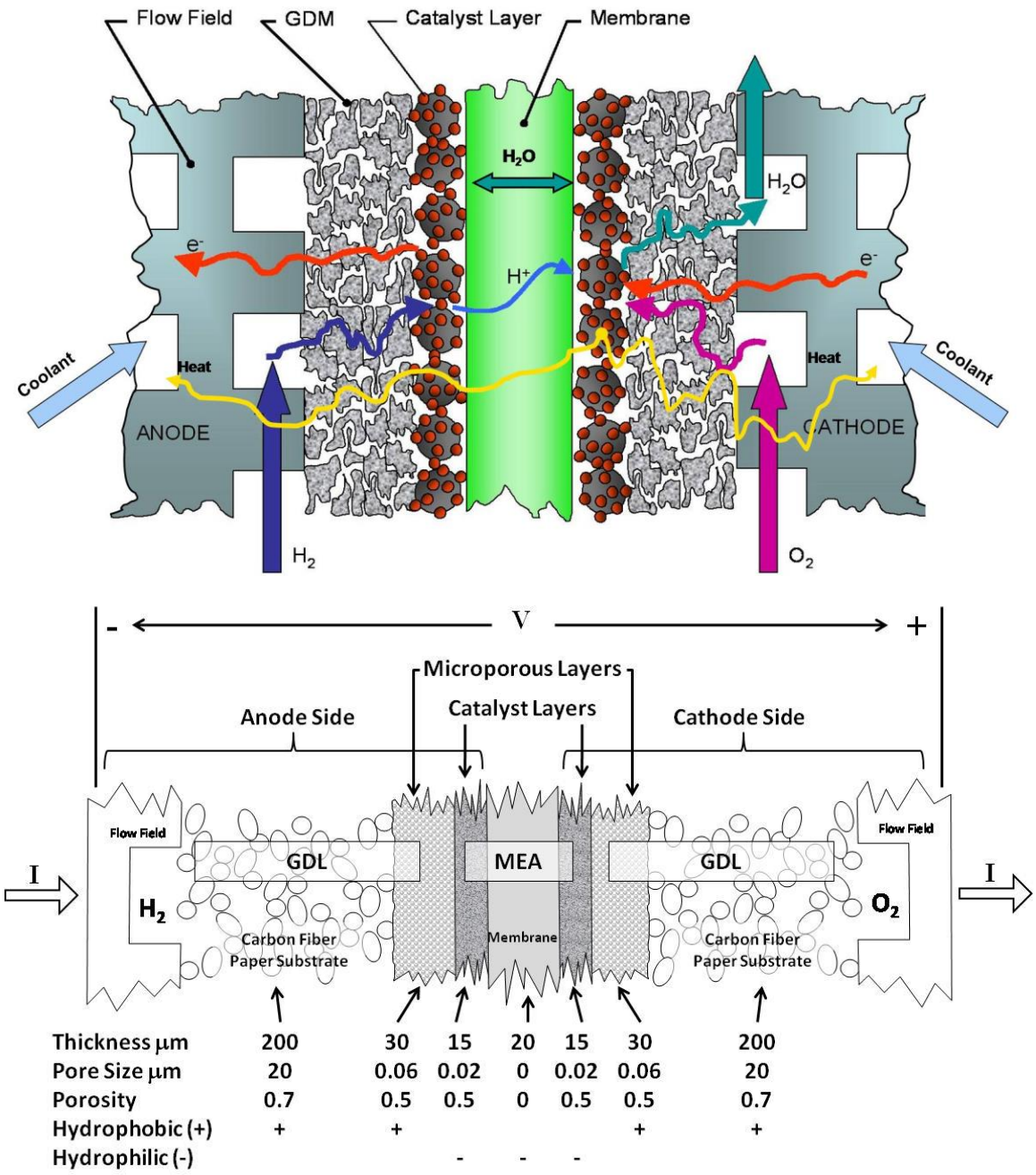

Figure 1.1: Cross-sectional schematic diagrams of key transport paths and length scales in a hydrogen fuel cell. Note that water is produced by the oxygen reduction reaction at the cathode electrode.

To achieve acceptable fuel cell performance, some minimum level of hydration is required to facilitate efficient ionic conductivity in the proton exchange membrane. However, excess liquid water is associated with a variety of performance and durability problems, including voltage loss at high current density due to reactant gas mass transport limitations [2], voltage instability at low current density [3],

unreliable start-up under freezing conditions and the associated material degradation effects [4], and corrosion of the carbon catalyst support due to hydrogen starvation [5]. Therefore, PEFC materials, hardware design and operating conditions must achieve a proper balance between too little and too much water. Advancement of fuel cell technology to the ultimate goal of efficient, cost-effective, zero-emissions electrification requires new measurements and models to quantify micro-scale transport processes within bulk materials and at critical material interfaces. Resolution at small length scales is necessary to fully understand performance and durability issues of "traditional" fuel cell materials, and to develop and refine new materials that have the potential to achieve stringent system cost targets.

1.2. Irreversible Voltage Loss in PEFCs

The most common way to obtain electrical energy is using turbines driven by fuel burning, wind or falling water etc., where mechanical energy is transferred into electricity. In the chemistry domain, converting energy from fuels into electricity is of most interest. There are at least three types of energy transfer occurring in this process, namely: (a) from chemical energy into heat energy, (b) from heat energy into mechanical energy and (c) from mechanical energy into electricity. Suppose the first and third transfers are ideally 100%, the whole efficiency of transfer would be limited by the second transfer. The highest efficiency during this type of transfer between a hot reservoir at temperature T_1 and a cold reservoir at T_2 is constrained by the Carnot cycle and this efficiency can be expressed as

$$\eta_{th,rev} = 1 - \frac{T_2}{T_1} \quad . \qquad (1)$$

This equation clearly demonstrates the Second Law of Thermodynamics where energy must always be converted to heat for the process to be spontaneous and, in practice, real efficiency is always much lower than the value given by Carnot cycles.

However, fuel cells are not confined by the Carnot limitation since they do not undergo direct conversion of heat to other usable energy form. Take hydrogen and oxygen, for example. At standard conditions (298.15 K and 1 atm), the following reaction (Equation 2) has enthalpy Δh° = -285.83 kJ/mol and Gibbs free energy Δg° = -237.09 kJ/mol.

$$H_2 + \frac{1}{2}O_2 \longrightarrow H_2O \qquad (2)$$

The reversible voltage, $E^o_{rev,}$ is determined from the ratio of the number of moles of electrons to reactant n and the Faraday constant F in Equation 3

$$E^o_{rev} = -\frac{\Delta g^o}{nF} \quad . \tag{3}$$

Therefore, it would be theoretically possible to extract 237 kJ/mole of electrical work at 1.23 V from 1 mole of hydrogen, which is only slightly lower than the heat evolved from firing 1 mole of hydrogen. In this case, the efficiency would be 83%, which is much higher than the Carnot cycle and the energy wasted is solely due to the loss of entropy in the reactions.

For a detailed analysis, the reversible voltage must also account for deviation from standard conditions and variation in chemical potential due to the concentration of reactants. For these differences in temperature, pressure, and reactant partial pressure the Nernst equation applied to the hydrogen-oxygen fuel cell reaction is used [6]

$$E_{rev} = E_T - \frac{RT}{2F}\ln\frac{1}{p_{H_2}p_{O_2}^{0.5}} \quad , \tag{4}$$

where E_T is the reversible voltage corrected for temperature

$$E_T = E^o_{rev} + \frac{\Delta s}{nF}(T - T_o) \quad . \tag{5}$$

Once the reversible thermodynamic efficiency is known, the practical fuel cell efficiency can be determined by quantifying the irreversibility that exists in the fuel cell assembly. These irreversible losses are associated with reaction kinetics, proton and electron resistance, and concentration loss due to mass transport resistance. Specifically, this is where the activation loss for the anode hydrogen oxidation reaction (HOR) and the cathode oxygen reduction reaction (ORR) are approximated by the Tafel equation for the case of an irreversible reaction process in which the forward-reaction dominates.

$$\eta_{act} = -\frac{RT}{\propto nF}\ln i_o + \frac{RT}{\propto nF}\ln i \tag{6}$$

The charge transfer coefficient, $\propto$, expresses how the change in the electrical potential across the reaction interface impacts the forward versus reverse activation barrier. The dynamic equilibrium where the net reaction rate is zero is characterized by the exchange current density, i_o. The Tafel equation results in a linear relationship of activation loss, $\eta_{act,}$ vs. current density, i.

The ohmic loss is dominated by protonic resistance through the electrolyte membrane with small components associated with contact resistance in the electron-conducting materials. Additionally, the electrolyte that typically covers the catalyst layer also contributes to ohmic loss. However, this sheet resistance is also a function of current density because utilization through the depth of the catalyst layer decreases at high current output. The ohmic loss, $\eta_{\Omega,}$ that describes these resistances in series is given by

$$\eta_{\Omega} = i\left(R_{\mathrm{C,an}} + R_{mem} + R_{\mathrm{C,cath}} + R^{eff}_{H^+,an} + R^{eff}_{H^+,an}\right) . \qquad (7)$$

Figure 1.2 illustrates the relative magnitude of these losses as they relate to the equilibrium potential, where the resulting cell potential, (E_{cell}), is referenced to the anode.

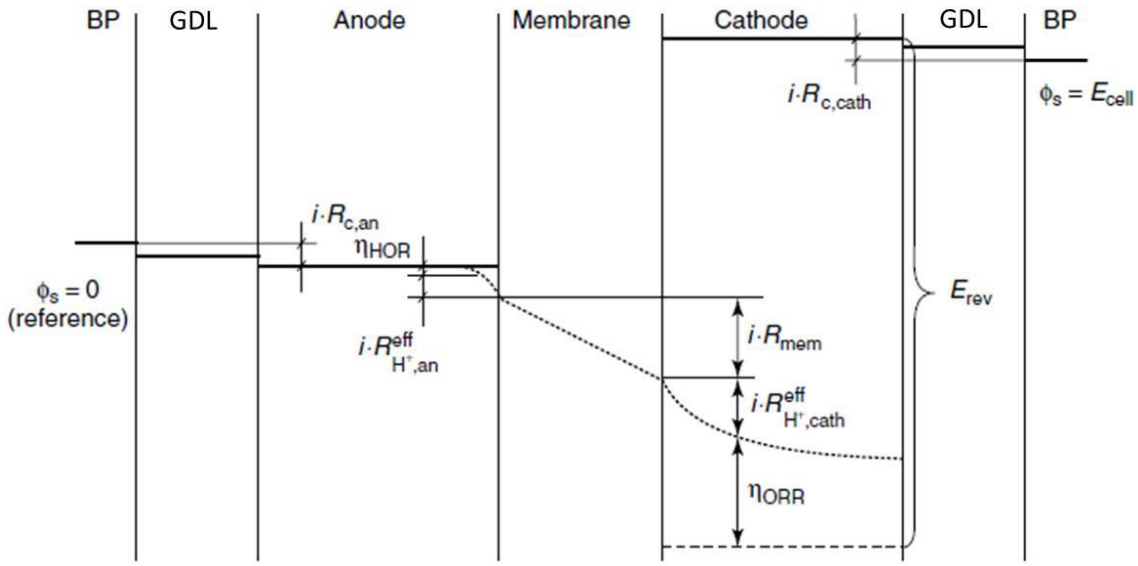

Figure 1.2: Solid phase and ionomer phase potential distributions illustrating the various voltage loss contributions. The solid lines represent potential loss in the solid phase (ϕ_s) through which electrons are transported and the dashed lines are for the potential of the ionomer with which protons are transported [7].

The partial pressures of hydrogen and oxygen in the anode and cathode catalyst layers must be known to predict E_{rev} (Equation 4). Therefore, relative to the concentrations in the channel, the second term in Equation 4 can also be used to predict the voltage loss due to concentration loss during diffusion from the supply to the catalyst layer. It most convenient to do this based on the limiting current density, i_{lim}, defined by Darcy's law,

$$i_{lim} = nFD^{eff}\frac{c_{r,ch}}{\delta} \quad , \tag{8}$$

where an effective reactant diffusivity coefficient, D^{eff}, accounts for the additional diffusion length in the porous GDL and catalyst layer of thickness δ. The difference in reactant concentration is the concentration in the gas delivery channel, $c_{r,ch,}$ as the concentration at the catalyst surface must be zero at the limiting condition. Based on the limiting current density, the voltage loss can be defined as

$$\eta_{conc} = \frac{RT}{nF}\left(1+\frac{1}{\alpha}\right)\ln\frac{i_{lim}}{i_{lim}-i} \quad . \tag{9}$$

Combining Equations 4, 6, 7, and 9 results in a simplified model of fuel cell performance

$$E_{cell} = E_{rev} - \eta_{act} - \eta_{\Omega} - \eta_{conc} \quad , \tag{10}$$

where the definition of these losses highlights the key parameters involved with optimizing fuel cell performance. However, this is deceivingly simple because nearly all terms are a function of temperature and water activity. Permeation through the membrane and electroosmosis further complicate the material balance. As a result, accurate prediction of the temperature and concentration gradients that are illustrated in Figure 1.3 require bulk and interfacial information for each component in the fuel cell assembly to solve the heat and species equations. Additionally, the boundary condition at the channel is dominated by convection, and species concentrations are changing down-the-channel as reactants are consumed and water is generated.

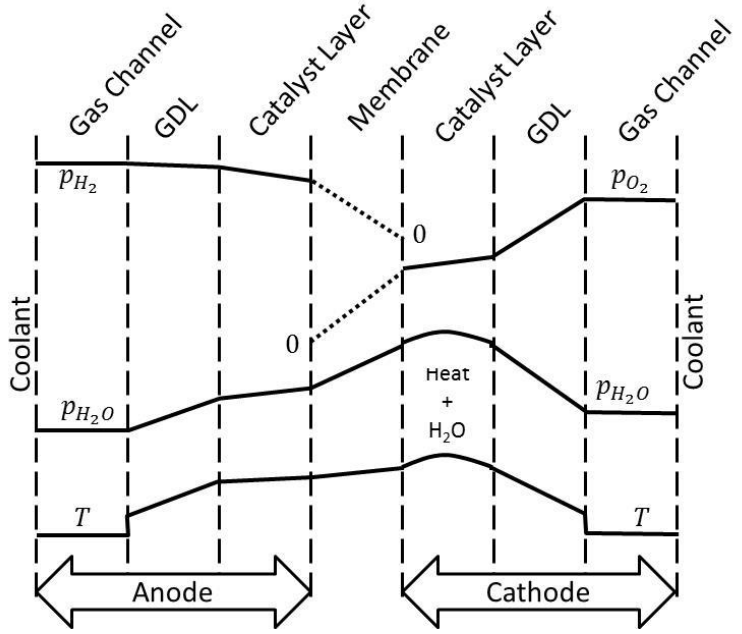

Figure 1.3: Relative gradients in gaseous species partial pressures and temperature through the fuel cell assembly.

There is extensive literature on modeling of transport processes in fuel cells. In many cases, these modeling studies focus on a subset of fuel cell components, with little or no attention given to interactions at material interfaces. Other models attempt to incorporate full three-dimensional representations of every component, but often with weakness in the underlying physics, or such complicated numerical schemes that the model cannot be reasonably applied as a design tool. The approach currently taken by many fuel cell developers is to first develop a comprehensive database from experiments conducted on a well-defined, representative material system. These experiments focus on in-situ and ex-situ measurement methods with resolution normal to the proton exchange membrane to quantify transport processes at critical material interfaces in addition to bulk phase transport.

1.3. Transport Resistance in PEFCs

With regard to transport, researchers are focused on quantifying and modeling the last three transport terms in Equation 1. Electron, ion (proton), and mass transport are all strongly influenced by water activity, and early work in collecting these losses for a comprehensive model was limited to operating conditions where the relative humidity was less than 100% or the impact of liquid water accumulation was not taken into account [7]. Because of the effect of even small temperature gradients on water transport and phase change, the thermal transport resistance and the resulting saturation gradients are now being considered in parametric fuel cell models [6]. The following represents a collection of critical transport parameters being used or currently needed for advanced PEFC performance prediction.

1.3.1 Electronic Resistance

The ohmic loss associated with the mobility of electrons is most strongly influenced by the contact resistances between the various diffusion layers with only a small contribution from the through-plane bulk electrical resistance. For a one-dimensional model, this resistance can be measured using the as-made gas diffusion layer (GDL), which consists of a polytetrafluoroethylene (PTFE) coated carbon fiber substrate along with a carbon black microporous layer (MPL). Two sheets of GDL with the MPLs facing each other are placed in a fixture with compression plates made of the flow field (current collector) material and geometry [8]. Resistance measurements at a given stress result in a lumped electrical resistance that consists of all contact resistances along with the weighted average of the through-plane and in-plane bulk resistances as they apply to the flow field geometry. For a more detailed model or multi-dimensional approaches, the in-plane and contact resistances are measured independently [9]. The bulk electrical resistance in the relatively thin electrode is negligible.

1.3.2 Protonic Resistance

In addition to the electronic resistance through the solid phase, the ohmic resistance includes protonic resistance through the polymer electrolyte membrane. This resistance has a strong dependence on the RH in the adjacent electrodes and is only a weak function of temperature [10]. The membrane conductance as it varies with RH can be characterized by in-situ [11] or ex-situ [12] methods.

Furthermore, the sum of the electronic and protonic resistances is normally validated with AC impedance at high frequency during fuel cell experiments at various operating conditions.

Resistance to proton transfer also occurs in the dispersed electrodes where a thin film of electrolyte is responsible for a lateral transport relative to the membrane plane. In addition to being a function of RH as with the membrane, this resistance is also dependent on current density due to the variation in electrode utilization depth as current draw increases [13]. The electrode effectiveness can be modeled theoretically with Tafel kinetics, and this is used to correct an area-based proton resistance in the anode and cathode electrodes, which is commonly measured with H_2/N_2 AC impedance [10] and a transmission line model [14]. This method of characterizing the proton resistance in the electrode requires an assumption of uniform ionomer film thickness and connectivity. The ionomer film is difficult to characterize and if this film were discontinuous or could be described as having significant variations in thickness, the idealized proton resistance proton resistance would under predict the loss associated with proton mobility in the electrode.

1.3.3 Thermal Resistance

All of the voltage loss terms have some functionality with temperature. To accurately predict the reaction kinetics and the gas composition at the catalyst surface, the temperature profile through the fuel cell sandwich must be established. There are several methods for characterizing the bulk and contact resistances of fuel cell components as reviewed by Zamel and Li [15] and Wang et al [16]. The total thermal resistance is used to solve the heat equation in one of two dimensions based on the heat flux from the cathode catalyst layer. At high RH conditions where proton resistance is minimized along with product water flux from the cathode catalyst layer, such an analysis elucidates regions of phase change within the open volume of the diffusion layers and gas delivery channels. Recently researchers have begun to characterize how the resulting saturation impacts the thermal resistivity [17]. Ex-situ investigations of thermal resistance as a function of saturation have shown that this relationship can be accurately approximated by an effective thermal conductivity [18]. To implement this, the saturation distribution must be established by solving the species transport using a series of diffusion resistances.

1.3.4 Diffusion Resistance

There are several length scales for which diffusion resistance must be characterized. For a given total pressure in the flow distribution channel, the first resistance to mass transport is encountered at the GDL interface. The convective mass transfer coefficient, computed from the Sherwood number for a given flow rate and channel geometry, is used for single phase conditions in the channel [19]. The impact of liquid water in the gas channel is accomplished with a modified Sherwood number [20] and by reducing the gas contact area using a surface coverage ratio [21].

Diffusion of reactants from the gas delivery channels using nonwoven carbon fiber paper treated with PTFE and coated with a microporous layer (MPL) located at the catalyst layer interface has shown the best performance, and researchers have focused their transport modeling and experiments on this substrate type as a result. Characterization of diffusion and governing parameters has been accomplished using conductivity cells [22], mercury intrusion porosimetry, cross-sectional scanning electron microscopy, x-ray micro-tomography [23], and Loschmidt diffusion cells [24]. These results are typically compared to the Bruggeman approximation [25] that is based on the geometry characterized by porosity (ε) and tortuosity (τ) of a homogeneous porous medium. The modified Bruggeman approximation that results can be used to estimate the effective diffusion coefficient through the GDL substrate and MPL [26].

In-situ characterization of the oxygen diffusion resistance in the presence of liquid water has been investigated with AC impedance spectroscopy [27] and expanded upon with liquid water visualization methods to quantify saturation [28]. To date, the mass transfer resistance measured with impedance has not been directly correlated to saturation measured with visualization. Such a correlation would be dependent on the transmission line model, which is widely debated for low frequency fitting. A more direct in-situ measurement of oxygen diffusion resistance has been presented in previous work by Baker et al. [19] and Caulk et al. [29] that established a method and analysis using limiting current measurements under dry and oversaturated conditions. These limiting current methods and the corresponding analysis have shown that the effective diffusion coefficient follows a characteristic behavior. With increasing current density, a dry then a wet plateau is observed for several types of carbon fiber GDLs. Although these measurements result in a diffusion resistance while a two-phase condition exists in the fuel cell assembly, the degree of saturation and its distribution is unknown. As a

result, a direct correlation between saturation (*s*) and the resulting change in the diffusion resistance will be required to validate a simplified saturation model.

Intermolecular diffusion accounts for the majority of resistance in the carbon fiber substrate; however Knudsen diffusion in the nano-scale pores of the MPL and catalyst layer must be accounted for. This requires accurate characterization of the pore structure of the layers and an idealized approximation. Alternatively, the limiting current analysis developed by Baker et al. can be used to isolate the pressure independent component of diffusion resistance which accounts from Knudsen effects and interfacial resistance through water/ionomer (combined with Henry's law). Studies have shown that this interfacial resistance is a significant component of voltage loss as it scales with reduced platinum loading and that it is much higher than expected based on oxygen permeability through bulk ionomer [30] [31] [32] [33]. This interfacial resistance at or near the catalyst surface is of critical importance for low cost fuel cells with dispersed catalyst and is the topic of intense fundamental research and detailed catalyst layer modeling. Currently in a parametric model, this resistance is accounted for using by an unrealistically thick ionomer layer with bulk (membrane) transport properties.

1.3.5 Membrane Transport

Accurate prediction of the reactant partial pressure at the catalyst surface requires the solution of species throughout the fuel cell assembly. Although the thermal, electronic, protonic, and gas-phase transport resistances can be characterized, the water balance between the anode and cathode due to water permeation through the electrolyte must be accounted for. This water balance also complicates the prediction of phase change and most of the components of transport resistance are a function of the local liquid water content. Water diffusion coefficients measured with bare membrane material by various methods as a function of water uptake have been the subject of significant debate amongst fuel cell researchers [34] [35] [36] [37] [38] [39] [40] [41] [42] [43]. Most recently, Caulk et al. [44] found no significant interfacial resistance and a monotonic increase of the membrane diffusion coefficient with increasing membrane hydration. Water transport through the membrane is further complicated by electroosmosis associated with the motion of protons from the anode to cathode through the membrane. The value of this electroosmotic drag coefficient also varies significantly in literature [45] [46] [47], and since it scales with current density, it plays a critical role in predicting the water balance. Given these difficulties, many parametric models use an empirical effective drag coefficient to account

for the decrease in back diffusion of product water from the cathode to the anode in order to counteract electroosmosis.

1.3.6 Down-the-Channel Solution

The various resistances described above are assembled in a through-plane model with boundary conditions at the flow distributors that include total pressure, species concentration, temperature, and a reference potential of 0 V at the anode current collector. The cathode current collector potential is calculated based on Equation 1 where electronic and protonic resistances are used to predict the ohmic losses and the diffusion and thermal resistances are used to predict the species partial pressures and temperature in the catalyst layers for calculation of the half-cell potentials, reaction kinetics and membrane transport . This can be solved one-dimensionally with average values over the geometric features or two-dimensionally accounting for anisotropy.

Practical fuel cell stacks have significant variation in the channel boundary conditions from the inlet to the outlet. To account for this, the parametric model is applied down-the-channel, assuming equipotential current collectors or by using a correlation for lateral potential difference through the current collector. This solution requires an accurate prediction of flow resistance in the channel. Although straight forward for single phase conditions, a two-phase pressure differential correlation is required once the flow distributor condition exceeds 100% RH [48] [49] [50] [51]. Additionally, fuel cell systems typically operate with hydrogen stoichiometric ratios greater than 1.0, which require a methodology for recirculating exhaust anode flow. In this case, the nitrogen and water content in the anode flow distributor due to membrane crossover must be accounted for as the diluted hydrogen feed stream will impact performance.

1.4. Scope of Proposed Research

The previous section outlined the key parameters required to characterize transport in PEFCs. The current work is aimed at a subset of these parameters that has been chosen based on their impact to the current state-of-the-art technology and identified shortfalls in the public domain (peer-reviewed literature).

1. The first is diffusion resistance inside the porous electrodes subjected to saturated conditions.
    a. **Goal:** A validated correlation between diffusion resistance and local liquid water content.
    b. **Significance:** Validation work is needed to rectify discrepancies between the more fundamental pore network models and the simplified approach that utilizes diffusion resistance based on average porosity reduction. PEFCs operate at the highest efficiency near saturation, where the ionic conductor is fully hydrated. At these conditions the liquid water that accumulates has the highest impact on the overpotential associated with diffusion loss.
    c. **Approach:** Using limiting current experiments with simultaneous neutron imaging, oxygen transport and liquid water content are measured. These data are used in a diffusion simulation to determine the effective diffusivity as a function of local saturation.
    d. **Current Hypothesis:** Effective diffusion theory over estimates the level of saturation in current GDL materials. This is a result of the heterogeneous pore structure where small volumes of liquid water block diffusion through larger dry pores.
2. The next item of interest relates to the overall water balance- how it can be controlled passively with diffusion resistance studied in the previous goal.
    a. **Goal:** Create and validate a novel diffusion layer material design for manipulating the water balance to improve system efficiency.
    b. **Significance:** Due to progress that mitigates chemical degradation of the membrane, PEFC developers are now able to use thinner materials which reduce ohmic resistance associated with proton transport. However, thinner membranes also promote diffusion of nitrogen and water toward the anode, both of which are undesirable from a system standpoint since managing water and nitrogen in the anode subsystem results in both

efficiency and durability penalties. A material solution to manage diffusion toward the anode is highly desired as it could incorporate lower cost materials, improve performance, and reduce shutdown purge drying time.

c. **Approach:** First the practical impact of liquid water saturation on PEFC performance is established from a system perspective by considering the relationship between liquid water along with proton transport resistance and shutdown purge effectiveness using distributed current measurements and neutron imaging. Next, a gas diffusion substrate with high diffusion resistance (maintaining desired thermal, electrical, and mechanical properties) is developed. This material is applied asymmetrically on the anode side with a commonly used low diffusion resistance GDL on the cathode. Validation of the performance and water balance of this configuration is demonstrated for a wide array of PEFC operating conditions.

d. **Current Hypothesis:** The increased diffusion resistance on the anode will have a negligible impact on performance but can limit water flux into the anode under a wide range of operating conditions. This is feasible due to the hydrogen concentration, which is high and the diffusivity is fast, relative to oxygen in air on the cathode.

3. Accurate characterization of diffusion resistance in the relatively thick GDL enables researchers to deconvolute the second transport resistance of focus which occurs through the thin ionomer coating at the catalyst interface.

   a. **Goal:** Compare relative impact of interfacial vs. bulk oxygen transport resistance through thin ionomer coatings in dispersed Pt nanoparticle catalyst structures.

   b. **Significance:** As Pt loading is decreased and oxygen flux per unit Pt surface area increases, a significant transport loss occurs. There is much debate about physical nature of this resistance as it is much higher than measured in the bulk material. Many research groups use agglomerate models to resolve the transport limitation; however, these models are hard to use as a design tool because they include many parameters that are difficult, if not impossible, to validate. In situ work to isolate interfacial vs. bulk transport resistance in the thin layer will impact the development direction of ionomer materials and dispersed catalyst structures while providing future direction for modeling approaches.

   c. **Approach:** A parametric study varying ionomer content relative to Pt surface area and ionomer thickness at different Pt catalyst loadings is presented. The pressure

independent component of transport resistance is measured with limiting current experiments. The functionality of this resistance with Pt surface area can be isolated. By varying the distance between Pt nanoparticles at a given loading, the influence of surface area is determined.

d. **Current Hypothesis:** Following a significant body of fundamental research, it is hypothesized that a significant interfacial transport limitation occurs in current polymer electrolytes when constrained in thin films. This can be established by reducing the transport resistance as the ionomer surface area relative to Pt increases.

A detailed survey of literature regarding these critical components of transport research in PEFCs is provided in the following sections.

1.4.1 Transport Resistance in Saturated GDL

Some of the performance losses associated with low-cost PEMFCs are constrained by the reaction activity of a given Pt surface while others are mainly associated with the partial pressure of oxygen (for an air cathode) at this surface and the conductivity of the layers that comprise a fuel cell. Significant loss due to oxygen concentration may be mitigated by minimizing the diffusion length, while ohmic losses may be reduced by careful material selection coupled with proper compression and hydration of the ion conducting membrane. To negate gas transport loss, the oxygen concentration at the cathode surface would ideally be the same as in the supply air. However, in practice, where oxygen flow from the gas distribution system to the catalyst is governed primarily by diffusion through a gas diffusion layer (GDL), any blockage of the diffusion pathway will result in a performance loss. Since the cathode catalyst layer operates at a higher temperature than the lands due to the thermal resistance of the GDL and other media [6], and proton resistance is minimized near 100% relative humidity [12], condensation of product water in the GDL is typical at optimal operating conditions. Consumption of reactants also contributes to condensation, especially in the anode where stoichiometry is typically lower and the initial molar fraction of the fuel is higher.

Fuel cell researchers have a strong interest in characterizing the diffusion resistance through various types of GDL because as the ratio of the bulk diffusion coefficient of oxygen in air, (D), relative to that inside the porous medium (effective diffusion coefficient,D_{eff}) increases from unity, the Nernst potential deceases and the concentration polarization increases. As a result, a highly porous and low

tortuosity substrate is desired. However, such substrates must have several other characteristics needed for the fuel cell assembly that include stiffness, high electrical conductivity, acceptable thermal conductivity, and high capillary pressure to induce liquid water percolation. In the current state-of-the-art, randomly distributed carbon fiber paper treated with polytetrafluoroethylene (PTFE) has shown the best performance, and researchers have focused their transport modeling and experiments on this substrate type as a result. The Bruggeman approximation [25] that is based on the geometry characterized by porosity (ε) and tortuosity (τ) of a homogeneous porous medium (Equation 11) is typically used to approximate diffusivity.

$$\frac{D}{D_{eff}} = \frac{\tau}{\varepsilon} = \varepsilon^{-1.5} \quad (11)$$

For the heterogeneous carbon fiber fuel cell GDLs studied, most researchers present a modified Bruggeman relationship to predict the reported data [52] [53]. There seems to be a general consensus regarding the diffusion resistance measured for a given dry GDL type using these various methods. However, the impact of liquid water saturation on this key parameter is more difficult to elucidate. Some researchers have attempted to validate their empirical fits to these ex-situ measurements by artificially changing the porosity with additional PTFE content [26] [54], but the manner that PTFE will fill pore space relative to liquid water will be geometrically different. Recently, Rosen et al. [23] used micro x-ray tomography of a running fuel cell to characterize the three-dimensional liquid water morphology inside the GDL pores. These data were then used in a numerical simulation to derive an effective diffusion relationship for both the in-plane and through-plane dimensions. However, the cells used for x-ray experiments are limited by size, material, and x-ray exposure time. Additional in-situ characterization is desired such that the critical saturation point [3] and the corresponding distribution of water relative to the flow distributor geometry can be determined for the thermal boundary conditions associated with typical fuel cell materials.

In-situ characterization of the oxygen diffusion resistance in the presence of liquid water has been investigated with AC impedance spectroscopy [27] [55] and expanded upon with liquid water visualization methods to quantify saturation [28]. To date, the mass transfer resistance measured with impedance has not been directly correlated to saturation measured with visualization. Such a correlation would be dependent on the transmission line model, which is widely debated for low frequency fitting. A more direct in-situ measurement of oxygen diffusion resistance has been presented in previous work by Baker et al. [19] and Caulk et al. [29] that established a method and analysis using

limiting current measurements under dry and oversaturated conditions. Using differential channel conditions achieved with high stoichiometry, the dry mole fraction of oxygen was varied between 0.01 and 0.28, resulting in several limiting currents. The channel relative humidity relative to the water production rate was used to control condensation in the diffusion layer. When this condition fell below 100% RH, Baker et al. reported a constant diffusion resistance at all limiting currents. Caulk et al. expanded on this work, using a higher channel RH where condensation would occur as limiting current increased, and it was shown that the effective diffusion coefficient followed a characteristic behavior. With increasing current density, a dry and then a wet plateau is observed for several types of carbon fiber GDLs. The transition from the dry to wet mass transfer resistance occurs at a different current density for each type of GDL investigated, and this transition was directly correlated to the thermal conductivity of the GDL.

The work presented here aims to expand the limiting current method to provide D/D_{eff} as a function of water saturation through high resolution neutron imaging, which enables an accurate measure of the in situ water saturation. Previous work providing D/D_{eff} as a function of limiting current is difficult to apply to semi-empirical fuel cell models because the saturation fraction and its distribution are unknown. Also, comprehensive validation datasets are needed as pore network models that predict phase change and capillary driven transport continue to advance [56].

1.4.2 Passive Water Balance Control with Anode GDL

Although water is the product of the electrochemical reaction, any amount beyond that needed for efficient proton conduction in the membrane and electrodes is detrimental to performance, and likely limits fuel cell durability. Thus, hardware design, material selection and operating conditions must account for the fine balance between too little and too much water, and significant research activity has focused on methods for mitigating liquid water accumulation within the various fuel cell components while maintaining sufficient hydration needed for ionic conductivity.

Much of the previous applied water management research was based upon fundamental studies of the competing effects of electro-osmotic drag (EOD), by which water is transported with protons from the anode to cathode, and back diffusion which accounts for the water concentration gradient driven transport. The EOD and water production by oxygen reduction concentrate water on the cathode side of the membrane-electrode assembly (MEA), while back diffusion usually acts to transport water from

cathode to anode, thus flattening the water concentration profile across the MEA to a degree. As summarized by Ye and Wang [47] and Yan et al. [57], beginning in the 1970s many studies have been conducted to link membrane physical properties to these fundamental water transport processes. Because of the complication of separately measuring EOD and diffusion coefficients through ex-situ experiments which attempt to simulate operating fuel cell conditions, several papers have reported measurements of in-situ water balance which are used to quantify the net amount of product water that leaves the fuel cell by simply condensing and collecting water from the anode and cathode effluent streams [58] [59] [60] [61] [62]. Usually the anode and cathode reactant stream pressures are set equal to eliminate any convective water transport across the MEA, even though this effect would be expected to be small due to the very low hydraulic permeability of proton exchange membranes [63]. In many instances, the EOD coefficient is inferred by subtracting the back diffusion contribution to overall water transport from such in-situ water balance measurements. However, deriving the EOD in this manner requires precise understanding of the actual water concentration gradient across the MEA, for which the local temperature and liquid water accumulation at the membrane-electrode interface are key influencing factors, both of which are quite difficult to quantify in an operating fuel cell.

Recent papers have attempted to derive more detailed information beyond that which can be obtained from the bulk water balance experiments cited above. Lu et al. [64] developed a new straight-channel apparatus that combines segmented measurements of current density and species concentration, from which the spatially resolved water transport coefficient can be computed via material balance. For a co-flowing hydrogen/air cell, the anode water concentration first decreases due to the dominant EOD effect, while the water balance shifts back to the anode near the outlet as product water builds up on the cathode side. To study the effects of gas diffusion layer (GDL) properties on water balance during start-up, Nakajima et al. [65] determined the weight of retained water in the individual components (flow channel, GDL, electrode) of a fuel cell run at 40°C. They found that the combined effects of hydrophobic treatment of the GDL substrate, application of a micro-porous layer, and relatively high GDL air permeability have the effect of shifting retained liquid water from the electrode and GDL to the flow field channels.

Achieving efficient start-up of a fuel cell system under low temperature conditions requires an understanding of the balance and spatial distribution of product water during operation. It is necessary to comprehend the mechanism of water removal during the process of shut-down purge whereby air flows through the cathode flow fields to prepare the stack for the next start-up sequence. Theoretical

and experimental studies have been conducted to understand the fundamentals of the water removal process. Sinha [66] and Wang [67] have developed detailed models which reveal the complex interactions among the initial water saturation level within the fuel cell, and the temperature and air flow rate of the purge stream. These models have advanced the idea that two-dimensional drying occurs: propagation in the stream-wise direction across the active area, coupled with drying through the thickness down to the MEA. It is important to recognize that drying of the membrane and electrode ionomer, which is needed to provide sufficient "buffer" for water during the freeze start process, can only occur once the GDL and MPL adjacent to these components are substantially free of water. In fact, it has been shown that significant water volume is removed in the early part of the purge process before a measurable change in membrane or ionomer water content, as indicated by high-frequency resistance (HFR), is observed [68].

Because of the difficulty of obtaining in-situ measurements of water distributions, even for single cells of full active area, the limited experimental literature addressing the purge process has concentrated on experimental techniques that correlate the purge efficiency to bulk or average quantities. For example, Tajiri et. al. [69] used HFR as an indicator of membrane water content and purge effectiveness. Lee et al. [70] determined the amount of residual water retained in a 3-cell stack after purge by placing the stack under vacuum and then measuring the change in vapor pressure. Other researchers experimentally assessed the effectiveness of an anode purge by measuring the change in flow field pressure drop [71]. Generally, all these studies indicate that liquid water in the anode will slow the shutdown process and using hydrogen gas for purge is generally not considered viable since it decreases system efficiency.

Clearly, there is a very extensive literature on these competing fuel cell water transport mechanisms, and how the net water balance over the entire cell or within individual components is influenced by material properties and operating conditions. What is lacking is a new perspective on the traditional design that considers the practical impact of water balance and how it should be controlled for optimal system level efficiency. This is critical to improve water mitigation strategies for shutdown purge, start-up under freezing conditions, and to minimize the effects of anode hydrogen starvation [72] [73] [74]. Ultimately, a commercial PEFC system needs to handle the majority of product water on the cathode side as managing liquid water with hydrogen on the anode side is expensive. This issue receives little attention in literature but it is important to fuel cell developers as evidenced by the extensive patent activity regarding anode water [75] [76] [77] [78] [79] [80] [81] [82] [83] [84].

In PEFCs the gas diffusion layer is critical for benchmark performance. The obvious functions of the GDL are related to the land/channel geometry of the bipolar plate network of flow distribution channels, where the GDL must provide a diffusion path over the lands and conduction (electron and thermal) over the channels. The GDL must also provide mechanical support such that sufficient contact pressure is applied to the catalyst layer and also so that the GDL does not intrude into the channel. The less obvious function of the GDL is its thermal-diffusive resistance. The ideal GDL will insulate the cathode catalyst layer enough such an optimal thermal gradient will exist. This combined with an appropriate diffusion resistance can provide a diffusive flux that is optimized for flooding vs. ionomer hydration under wet and dry conditions, respectively. Additionally, the GDL is an expensive component because the use of lower cost precursor materials tends to have a negative impact on one of the GDL functions outlined previously. However, in the past these materials were generally considered symmetrically by evaluating performance with low-cost materials on both the cathode and anode. Although stiffness/compressibility and electrical and thermal conductivity requirements are fairly well defined for the anode and cathode sides, the diffusivity requirements will be much different as oxygen diffusion in nitrogen is over 3 times slower than hydrogen in nitrogen (0.18e-4 vs. 0.68e-4 m^2/s). Additionally, the HOR overpotential is less sensitive to hydrogen partial pressure than the ORR is to oxygen partial pressure. Therefore, in the context of passive control of stack water balance, modified anode diffusion resistance relative to cathode is feasible. However, it should be considered that reduced hydrogen partial pressure at the anode catalyst can slightly impact the equilibrium (Nernst) potential in a recirculating anode sub-system.

The goal of the final component of the proposed research is to consider how further increases in anode diffusion resistance can impact water balance. Thicker layers are undesirable at the outset, thus increased tortuosity to porosity ratio is the only feasible way to increase water vapor diffusion resistance. For porous fiber/particle structures like the GDL and MPL, it is difficult to achieve a tortuosity greater than 2 based on geometric constraints. However, a fiber paper with platelets oriented in-plane can increase tortuosity. The design and characterization of this new anode GDL material will provide a new dataset that highlights the influence of diffusion resistance in the overall water balance while serving as a prototype of passive water management.

1.4.3 Transport Resistance in the Ionomer Layer

There are several challenges that arise in practical PEFC systems when Pt is used sparingly. First, when the electrode structure is made thinner to reduce Pt loading, water management, particularly during transients, can limit performance [85] [86]. Second, as local current density at the Pt surface increases with decreased loading, resulting in a lower cell voltage, the oxygen reduction reaction rate stops following simple Tafel kinetics and becomes potential-dependent [87]. Third, for ionomer-coated catalysts, an additional transport resistance from the electrode pore to the Pt surface has been reported that is much higher than oxygen permeability through bulk ionomer [30] [31] [32].

The current work details an investigation of the third challenge - using a series of experiments that attempt to isolate key components of the electrode design that impact local transport performance. Maintaining a constant catalyst layer thickness and macroscopic structure, the impact of loading and Pt dispersion was studied with performance and limiting current methods. These results are then used to consider key parameters that impact the performance loss at low Pt loading. Further insight is obtained by scaling the variations in the total transport resistance measured with limiting current to Pt surface area. For a constant pore structure, this analysis isolates oxygen transport loss at the Pt surface independently of bulk and Knudsen diffusion effects [19]. Additional data dives further into transport loss mechanism, where a constant catalyst layer thickness and macroscopic structure were maintained, and the impact of loading and ionomer to carbon weight ratio was studied with performance and limiting current methods.

There is significant discussion in recent literature about the parameters being studied herein. The most obvious is the oxygen permeability in thin Nafion® films vs. bulk; however, due to the difficult nature of this measurement there are no reported data currently available at the length scales of interest (less than 30 nm). While direct measurements of oxygen transport resistance are elusive, researchers have recently focused on related parameters. Although the change in physical properties of these films is established [88] [89] [90] [91] [92], the water/polymer morphology and related stiffness are not. Research groups have also reported interfacial interactions of thin Nafion® films that are unique to the supporting substrate [93] [94]. These experiments generally report lower uptake in thin films than bulk but there is significant variation in the magnitude of the decrease reported. In more applied experiments, Iden et al. reported similar uptake relative to bulk in actual catalyst layers [95]. Perhaps

analogous to water uptake, there is also significant variation in proton conductivity reported for thin Nafion® films [96] [97] [98].

Understanding local transport resistance also requires consideration of the complex structure of dispersed Pt on carbon and ionomer system. The one-dimensional relationships described previously capture key parameters for an idealized system but the catalyst layer does not have a homogeneous pore structure. In fact, significant heterogeneities exist in the catalyst layer due to mesoscale defects in the primary carbon particle as well as aggregation [99] [100]. These agglomerates introduce new transport domains relative to the assembled macroporous catalyst layer. Unfortunately it is difficult to decouple the impact of the mesoscale structure inside the agglomerate relative to the outer surface that has more direct access to the oxidant within the macro pores of the catalyst layer. This agglomerate relationship is widely studied with transport modeling [101] [102] [103] [104] [105]; however, without direct validation, the physical theory and input parameters vary significantly in these proposed models.

The research described herein is designed to consider the relative influences of parameters related to local transport at the Pt nanoparticle, where samples are designed such that mesoscale and agglomeration effects are consistent across all configurations. To interpret the experimental results, limiting current at an individual Pt particle based on oxygen transport through the ionomer is modeled to consider the role of interfacial resistances. The results elucidate key modeling parameters and the relative importance of the ionomer to Pt surface area.

2. Chapter 2 – Method of Approach

2.1. Summary of Experiments

Experiments were designed around the three goals outlined in Section 1.4. Experiments utilize unique materials, test hardware, and test methods. This section is intended to give a brief introduction to the experimental plan for each goal. The titles of the following Subsections represent the parameters being isolated for the specific experimental campaign and, where possible, these experiments have been kept consistent by using common materials and characterization techniques throughout the research program. The details of the experimental methods mentioned are described in the subsequent sections.

2.1.1 Impact of GDL Saturation on Oxygen Diffusion Resistance

This portion of the experimental work is designed to accomplish Goal 1 in Section 1.4. Experiments were executed using a specially designed 5 cm^2 active area fuel cell operating at limiting current under various differential conditions with simultaneous neutron imaging. Two GDL substrates with different thermal conductivities but similar pore related properties were selected to investigate the impact of liquid water content in the GDL. The high and low thermal conductivity GDLs selected for this study were Toray TGP-H-060 and Mitsubishi Rayon Corp. (MRC) Grafil U-105, respectively. All other experimental and material components kept constant. Limiting current density at various oxygen concentrations in the channel were required to solve the diffusion equation. Spatially resolved liquid water saturation obtained from analyzed neutron images of the through-plane water content was used to specify the local porosity change.

2.1.2 Impact of Anode GDL Transport Resistance on Water Balance

In this portion of the experimental studies for Goal 2 in Section 1.4, the impact of liquid water accumulation in the anode GDL was first established using a PEFC test fixture based on commercial design constraints [68]. Shutdown cathode purge time required for removal of anode water was considered with neutron imaging by artificially filling the anode vs. cathode GDL. The spatial-temporal results of drying enabled convective and diffusive contribution to be evaluated and these data along with analysis can support the determination of an overall mass transfer coefficient. In situ saturation was also measured for comparison of drying time, which was used in later analysis to determine the

actual fraction of water in the anode under realistic PEFC system operating conditions. Since purge time is ultimately constrained by the ionomer water content required for a subsequent startup, the relationship between distributed liquid water and ionic resistance was investigated with distributed high frequency resistance measurements.

The practical impact of liquid water accumulation in the anode gas volume along with transport relationships determined during the course of this research program serves to establish the importance of water balance control. As a result, a novel GDL layer with high diffusion resistance was proposed for the anode. System related active control of water has significant cost penalty and passive material solutions are highly sought after. For this reason, along with the results of the current research, an anode GDL with high transport resistance was considered. The proposed material shown in Figure 2.1 must still maintain the thermal, electrical, and mechanical functions of the widely used carbon fiber substrate. This required significant material development and validation testing to arrive at a suitable prototype, the details of which are described in later sections. Experiments comparing the water mass balance of the anode vs. cathode of the high resistance anode material to symmetric baseline configurations were executed. The results provide validation of a novel design concept which was invented based on the transport resistance relationships developed during this research program.

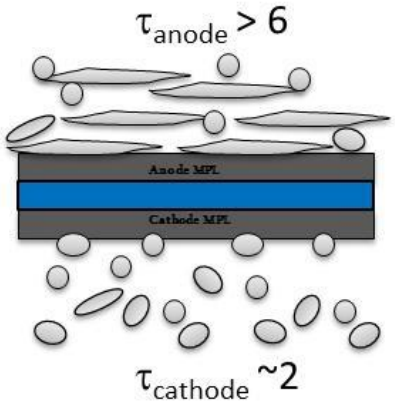

Figure 2.1: Cross-sectional schematic of GDL configuration with a high tortuosity anode composite structure.

2.1.3 Impact of Pt Nano-Particle Dispersion on Oxygen Transport Resistance

These experiments are related to Goal 3 in Section 1.4. Cathode catalyst layer loading and density of platinized aggregates were varied while maintaining thickness by mixing various weight percentages of Pt on Vulcan XC-72® catalysts and the addition of bare Vulcan XC-72® when necessary. The resulting structure, illustrated in Figure 2.2, impacts oxygen flux near the Pt sites while maintaining a similar macroporous catalyst layer structure. This study represents a significant experimental campaign that included 12 cathode electrode configurations, with 3 samples of each run in 3 separate fuel cells with a consistent experimental protocol throughout. Three different test stands and hardware sets were used for each electrode type that enabled a statistical data summary that included test stand and hardware variation. The catalyst layer thickness was kept constant (within capability of the coating method) throughout this experimental campaign to reduce bulk transport differences between the samples. The resulting limiting current densities were used to identify the pressure independent component of transport resistance, which enabled the comparison of the various catalyst structures through analysis. Additional polarization curves under different operating conditions were used to compare performance and model accuracy.

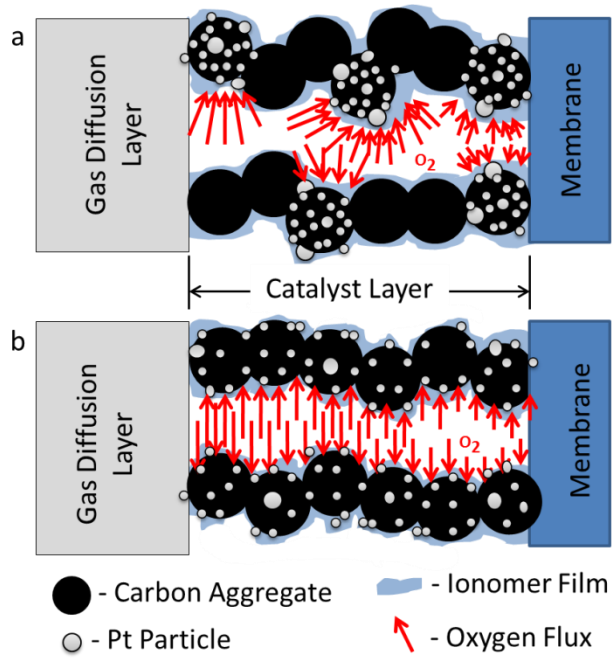

Figure 2.2: Catalyst layer structure resulting from a.) 50% wt. Pt/Vulcan diluted with bare Vulcan, and b.) mixing varied wt.% Pt/Vulcan catalysts. Not to scale, HAD area indicates Pt particles vary as much as 1.5x in low vs. high wt. % Pt/Vulcan catalysts.

2.1.4 Impact of Ionomer Loading on Oxygen Transport Resistance

In this study toward Goal 3 in Section 1.4, one catalyst type was used to study both low-loaded and nominal loaded cathode electrodes. Their performance was isolated as a function of ionomer film thickness (Figure 2.2) by altering the ionomer-to-carbon weight ratio (I/C) in the composite electrode. This ratio, historically studied in order to optimize performance at various operating conditions, especially low relative humidity, has not been thoroughly investigated as a possible contributor to gas transport resistance. A novel fabrication method was utilized in order to ensure uniformity at low coverage levels, and various diagnostic methods were employed to resolve the contribution of the above mentioned voltage loss terms. Limiting current and polarization performance was used to evaluate these samples.

2.2. Experimental Techniques

Several experimental techniques were required to accomplish the research goals outlined previously. Electrochemical techniques of cyclic voltammetry (CV), impedance, and polarization were used to characterize materials and performance. Liquid water content was measured with neutron imaging in both the through-plane and in-plane directions. Spatially resolved current distribution measurements were made using a printed circuit board attached to the flow field plate. Additional characterization tools were used to measure key material parameters not found it literature or those unique to the experimental materials developed for this research (discussed in Section 2.4).

2.2.1 Electrochemical Characterization

All electrochemical test conditions and methods used though the experimental campaigns are listed in Table 2.1. Generally, cyclic voltammetry was used to characterize Pt loading; mass activity of the catalyst was considered with pure oxygen polarization; diffusion resistance was evaluated with limiting current; and performance was assessed with air polarization at conditions with varying RH.

Table 1: Summary of test conditions used for various experiments.

#	Experiment	Details
1	HAD	20°C; H_2 / liquid water; 200 mV/s; 0-600 mV
2	Break-in	Wet and dry cycling between low and high current density
3	Cathode Recovery	2 Hours at 0.300 V; 40°C; 100% RH; 150 kPa
4	O_2 Pol Curve	80°C; 100% O_2; 100% RH; 150 kPa
5	O_2 Pol Curve	95°C; 100% O_2; 100% RH; 200 kPa
6	Air Pol Curve	80°C; 65%RH; 150 kPa
7	Air Pol Curve	80°C; 100%RH; 150 kPa
8	Air Pol Curve	95°C; 65%RH; 250 kPa
9	Air Pol Curve	95°C; 100%RH; 200 kPa
10	Limiting Current	Varied P_{O_2}; 70°C; 77% RH; 300 kPa
11	Limiting Current	Varied P_{O_2}; 80°C; 80% RH; 110 kPa
12	Limiting Current	Varied P_{O_2}; 80°C; 71% RH; 150 kPa
13	Limiting Current	Varied P_{O_2}; 80°C; 67% RH; 200 kPa
14	Limiting Current	Varied P_{O_2}; 80°C; 64% RH; 300 kPa
15	Impedance	H_2/N_2; 35; 50; 75; 122% RH; 0.2 V; const P_{H2} and P_{N2} = 253 kPa
16	Shutdown Condition	33°C; 0% RH; 150 kPa, 0.4 A/cm^2, 2/2 H_2/Air stoichiometry
17	Purge	33°C; 0% RH; 101 kPa, 0.1 A/cm^2, 2/16 H_2/Air stoichiometry
18	Shutdown Condition	76°C; 50% RH; 150 kPa, 0.4 A/cm^2, 2/2 H_2/Air stoichiometry
19	Purge	76°C; 0% RH; 101 kPa, 0.1 A/cm^2, 2/16 H_2/Air stoichiometry

Hydrogen adsorption/desorption (HAD) area was measured with cyclic voltammetry before and after all experiments to be run on each cell build (experiment 1 in Table 1). Cathode Pt-surface area was measured by integrating hydrogen adsorption peaks (assuming 210 µC cm^{-2}_{Pt}). The conditions of CV measurement were 30°C, 100% H_2 in anode and with the cathode channels filled with liquid water. The liquid water that fills the cathode helped maintain hydrogen partial pressure by preventing any hydrogen (crossing over from anode) from diffusing away from the cathode. This prevented the H^+ adsorption peaks (required for Pt surface area analysis) from being masked by the hydrogen evolution current [106]. Shorting resistance and hydrogen evolution current resulting from hydrogen cross-over were also measured in separate experiments with H_2/N_2.

After this initial characterization, several polarization curves were gathered in both oxygen and air to characterize mass activity [107], oxygen diffusion resistance, and consider the relative impact of water activity and temperature in the electrode or GDL (experiments 4-9 in Table 1). The air polarization

conditions were designed for a mixed outlet RH below, near, and above 100%. The high temperature air polarization conditions were designed to evaluate the relative impact of liquid water near the catalyst layer, where at high temperature vapor phase was prevalent. Impedance was used to measure membrane and electrode proton transfer resistances as described by Liu *et al.* [10]. Also shown in Table 1, a voltage recovery step was run periodically throughout the protocol. This step serves to remove contaminants and Pt-oxides from the catalyst surface. For low Pt loading performance studies, a consistent voltage recovery scheme improved consistency between experiments [108].

2.2.2 Limiting Current

The total transport resistance was derived based on limiting current at different total pressures with varied oxygen concentrations. To maintain uniform down-the-channel conditions, high stoichiometries was used. On the anode side, 0.84 slpm of hydrogen was used at all test points, which resulted in stoichiometries that exceed 5. Oxygen stoichiometries exceed 10 at all test points with a 5.0 slpm oxygen/nitrogen mixture flow rate. With the cell maintained at 70°C and 80°C, dry oxygen mole fractions ranging from 0.01 to 0.28 in nitrogen were used on the cathode to measure 10 limiting current values at 0.1 V for each concentration. At each test point the cell voltage is stepped down from 0.9 V and the polarization curve was inspected for a vertical trend near 0.1 V, thus indicating that a limiting current had been reached. At 80°C several anode and cathode total pressures were used to consider pressure dependence (experiments 11-14 in Table 1). At 70°C (experiment 10 in Table 1), total pressure was held constant at 300 kPa while the mixed outlet RH transitions from dry to wet as limiting current increased (at higher oxygen concentrations). These test conditions and the analysis thereof followed that reported in [19] [29].

The limiting current value, i_{lim}, was used to estimate a total resistance to oxygen transfer, R_O, with an assumption that the oxygen concentration at the electrode is zero by Equation 12,

$$R_O = \frac{4Fx_O^{dry-in}}{i_{lim}} \frac{P-P_w^{in}}{RT} \quad , \qquad (12)$$

where *F* denotes the Faraday constant; x_O^{dry-in}, the dry mole fraction of oxygen at the inlet; P, the total pressure; P_w^{in}, the inlet water vapor pressure; *R,* the universal gas constant; and *T,* the absolute temperature. In the experiments where total pressure is varied, the pressure independent component R_O^{PI} ,of R_O ,was determined from the intercept of R_O vs. P per Equation 13:

$$R_O = R_O^{PI} + R_O^{PD} \quad , \tag{13}$$

where pressure independent resistance, R_O^{PI} ,is associated Knudsen diffusion in the nano-scale pores and ionomer interaction that exists mainly in the catalyst layer. R_O^{PI} was determined to be 0.13 s/cm for the cell and electrodes used in the GDL studies. Given that the carbon fiber substrates being used in this study have mean pore diameters of approximately 30 μm, pressure dependent diffusion resistance, R_O^{PD}, dominated by intermolecular collisions will account for the GDL and channels. Mass transfer in the GDL was isolated by subtracting the resistance within the gas supply channels from R_O^{PD}. The channel resistance used was based on a constant convective mass transfer coefficient, (h_m), of 0.056 m/s that was computed from the Sherwood number given in [19]:

$$R_O^{PD} = R_O^{GDL} + R_O^{ch} \quad , \tag{14}$$

where the transport resistance through the GDL (R_O^{GDL}) with thickness, d, was approximated one-dimensionally using a shape factor, f, of 1.5 for the current geometry to account for the average diffusion length over the land (Equation 15).

$$R_O^{GDL} = \frac{fd}{D_{eff}^{GDL}} \tag{15}$$

The functionality of pressure independent transport resistance with the normalized Pt area (*loading × HAD area =* $A_{Pt,\ surf}$ / $A_{active\ area}$) was the focus of the catalyst studies. Based on the limiting current analysis, the pressure independent oxygen transport resistance (R_O^{PI}) is assumed to consist of Knudsen (R_O^{Kn}) and interfacial effects. Since an interfacial resistance would occur at or near the Pt surface, this component of resistance (R_O^{Pt}) is assumed to scale inversely with the normalized Pt area per Equation 16. This assumption is good when the local resistance is high enough to result in relatively uniform reaction current distribution [41]. Based on Equation 16, R_O^{Kn} is determined from the intercept of R_O^{PI} vs. $A_{active\ area}/A_{Pt,\ surf}$ relationship that was generated experimentally by varying Pt loading.

$$R_O^{PI} = R_O^{Kn} + \frac{A_{active\ area}}{A_{Pt,surf}} R_O^{Pt} \tag{16}$$

2.2.3 Purge Drying

A series of ex-situ experiments was developed to identify water in anode versus cathode GDL by comparing removal rates during purge. In these experiments, the anode or cathode GDL was artificially saturated by submersing the GDL in water under vacuum to effectively force water into about half of the open volume, as was confirmed by weighing the saturated GDL. For each experiment, the saturated anode or cathode GDL was assembled into the test hardware with the MEA and the opposite GDL kept free of liquid water. With simultaneous neutron imaging, purge experiments were then conducted with 1.0 slpm dry nitrogen purge flow at 101 kPa on the cathode at 33°C and 76°C; the resulting experimental matrix is shown in Table 2. The higher temperature was selected as it simulates the nominal design point for the fuel cell system being studied. The lower temperature represents, based on earlier experiments [68], a "cold" operating condition with significant liquid water present but at a temperature well above ambient where test section conditions can be confidently controlled. Water removal rates from these experiments were used to assess transport resistance through individual fuel cell components and to identify the location of liquid water during operation.

Table 2: Experimental matrix for ex-situ purge

Cell Temperature	Purged Flow Field	Anode GDL	Cathode GDL
76°C	Cathode	Dry	Saturated
76°C	Cathode	Saturated	Dry
33°C	Cathode	Dry	Saturated
33°C	Cathode	Saturated	Dry

To complement the ex-situ experiments, a series of in-situ preconditions and subsequent purges was developed. Two preconditions were investigated in counter-flow, one at 33°C with dry inlet hydrogen and air (dew point < 0°C, maintained by bypassing the test stand humidifiers) and the second at 76°C with 50% relative humidity inlet hydrogen and air (experiments 16 and 18 in Table 1). All preconditions were operated for 60 minutes at 0.4 A/cm^2, 2/2 anode/cathode stoichiometric ratios, and 150 kPa outlet pressure. A moderate current density was selected for this study because it was determined earlier in the research program that such a condition generally results in relatively high steady-state water content, and is thus a demanding condition for which to assess the dynamics of shutdown air purge. A total of at least 3 test runs were conducted per operating point to establish repeatability and measurement uncertainty.

From the resulting precondition saturation state, cathode purges at either 33 or 76°C were conducted with 1.0 slpm flow of dry nitrogen at 101 kPa. Just before initiating the purge, the fuel cell back pressures were reduced from 150 to 101 kPa (experiments 17 and 19 in Table 1). Lowering the gas pressure would be expected to improve the effectiveness of drying as it increases the vapor carrying capacity of the purge stream. Also, as a consequence of the pressure release, water slugs that resided in the channels were rapidly removed. For the these experiments this provided a convenient and repeatable starting point that was desirable as the GDL water content, its through-plane location, and removal rates were the focus of the investigation. Water slugs in the channels would have potentially confounded the results by causing flow maldistributions, variations in pressure drop, and uneven evaporation. In addition to neutron imaging a spatially resolved current distribution tool was also employed during these experiments.

2.2.4 Distributed Current Measurement

The fuel cell current distribution tool consisted of a printed circuit board with isolated contacts that redirect current through shunt resistors. The circuits were printed on a polytetrafluoroethylene substrate to improve neutron transmission in a similar manner to work reported by Gagliardo *et al.* [109]. As shown in Figure 2.3a, the measurement array consisted of 25 columns down-the-channel with 4 rows across the channels and lands. The voltage response across each shunt was measured with a separate data acquisition channel. The flow field was machined in thin graphite composite resin and bonded to the distributed measurement board (Figure 2.3b). The continuous flow field results in slight "blurring" of current between segments but this will be no larger than the 1.5 mm thickness of the plate. The plate was verified to be isopotential by monitoring voltage along the perimeter at varying distances from an applied current.

To measure the high frequency impedance component associated with the zero-phase resistance, the current was perturbated at a frequency of 1 kHz with a peak-to-peak amplitude of 500 mA. At this high frequency, the voltage and current were assumed to be in phase and ohmic resistance was calculated based on the voltage response, assumed constant for all segments (isopotential plate) relative to the individual current response which varied based on the resistance of each segment.

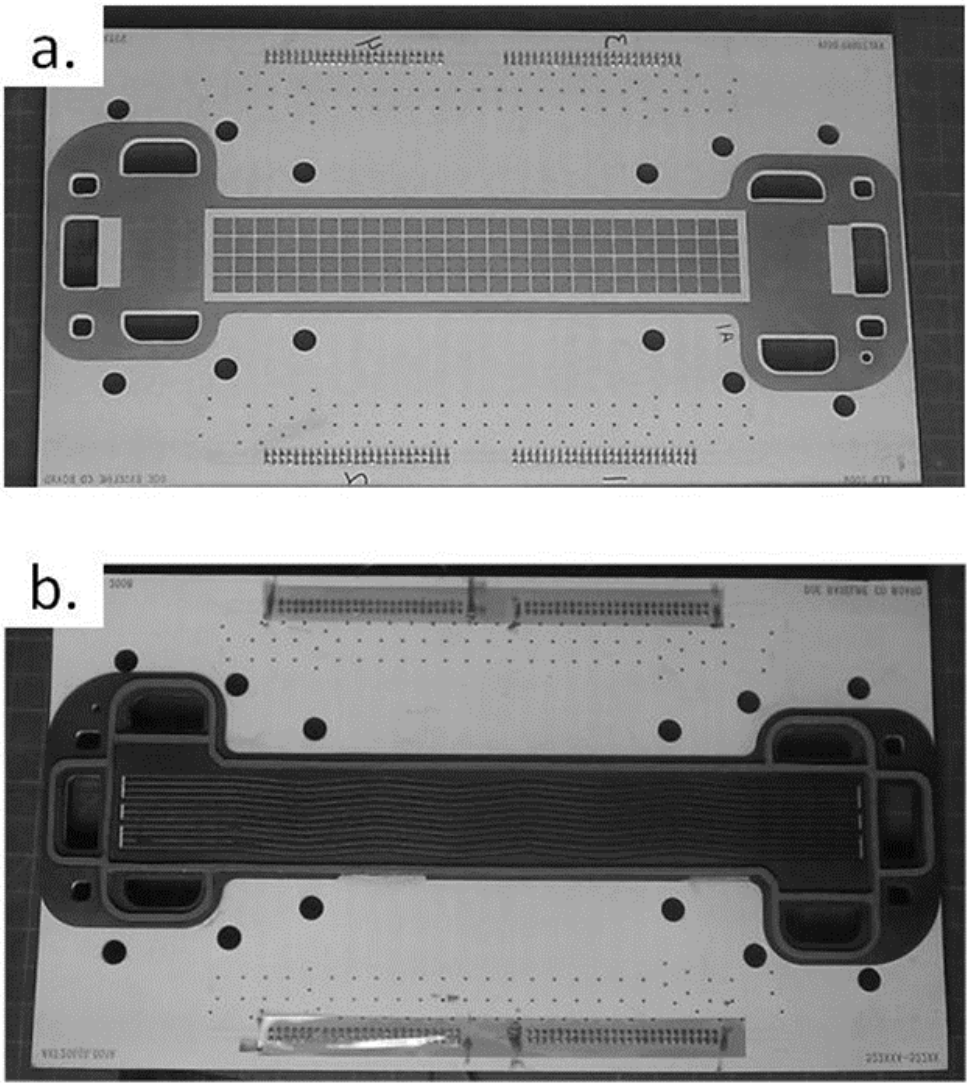

Figure 2.3: Distributed measurement tool, a.) printed circuit board, b.) composite flow field plate bonded to board.

2.2.5 Neutron Imaging of Liquid Water

In-plane liquid water distributions and transport rates were measured with high temporal resolution two-dimensional neutron radiography (Figure 2.4a) at the US National Institute of Standards and Technology (NIST) Center for Neutron Research (NCNR). The systems and methods employed have been previously detailed by Trabold et al. [110] and applied to PEFC research by several organizations. This two-dimensional technique was chosen for the purge experimental campaign because of its large viewing area and relatively high frame rate (1 frame/sec). With this technique the known flow field patterns enable one to distinguish between liquid water in anode and cathode flow field channels, but

an obvious shortcoming of the two-dimensional water thickness measurement is determining the through-plane location of water in the GDL. For this reason high resolution neutron measurements of through-plane water distributions as shown in Figure 2.4b were considered, but these methods are not currently practical for monitoring water transport rates in real-time over the entire active area. For this reason, in-plane water thickness measurements were utilized for transient measurements.

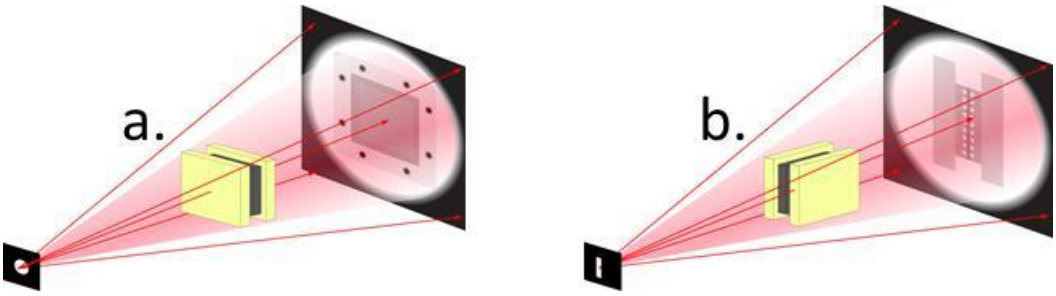

Figure 2.4: Neutron imaging of a.) in-plane, and b.) through-plane liquid water distributions.

For steady state studies of in situ liquid water content at limiting current the high resolution neutron imaging method was desired. Neutron transmittance through the sample was recorded using a second generation micro-channel plate detector with a spatial resolution of 13 μm. During each limiting current test point, images were integrated for 2 minutes and then a series of at least 10 images were averaged to reduce noise. These images were converted to liquid water thickness matrices using best practices described by Hussey et al. [111], and the specific analysis and parameters for this detection scheme detailed Fu et al. [112].

2.3 Hardware Design

Two test fixtures were designed specifically for this research. A 50 cm^2 test cell was used for down-the-channel analysis of liquid water distributions, water balance, and performance. For the limiting current differential analysis of through-plane transport a 5 cm^2 fixture was developed. The 50 cm^2 cell provided an appropriate channel length and pressure drop for low stoichiometric operation that is comparable to commercial designs. The 5 cm^2 cell provided a low pressure drop for the high stoichiometry flow such that a differential pressure in the channel was a good assumption.

2.3.1 50 cm² Active Area PEFC Designed Based on Commercial Systems

In-situ and ex-situ experiments were conducted on a small-scale test section that was specifically designed to simulate full-scale hardware that meets U.S. Department of Energy 2015 specifications for automotive fuel cells [113]. The derivation of hardware dimensions, gas diffusion layer (GDL) type and membrane electrode assembly (MEA) are described in detail by Owejan et al. [68]. In summary, a full-scale system was scaled to a 50 cm^2 active area with a high aspect ratio that enables investigation of the full flow field length. The resulting active area had a stream-wise length of 183 mm and width of 27.3 mm, and all flow field channels were 0.7 mm wide and 0.4 mm deep, with land spacing of 0.5 mm in the cathode flow field and 1.5 mm in anode. The flow field pattern is shown in Figure 2.5, where the observed out-of-phase sinusoidal flow field pattern minimizes GDL shear when the assembly is compressed to 1.7 MPa. This hardware was bonded to the current distribution tool shown in Figure 2.3.

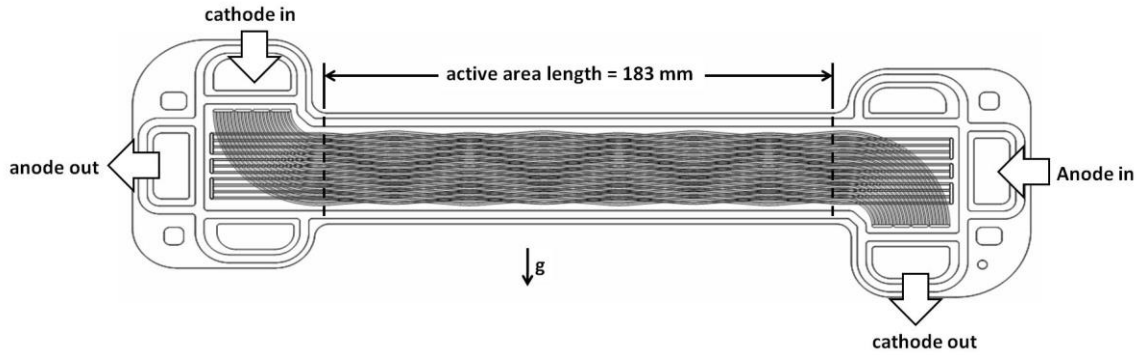

Figure 2.5: Test section flow fields [68]. Internal liquid coolant was not used for these single cell experiments. Orientation shown was used for neutron imaging.

2.3.2 5 cm² Differential Cell

A 5 cm × 1 cm active area straight-pass flow field with a 0.5 mm rib and channel width and a 0.8 mm channel depth shown in Figure 2.6 was used for all differential cell experiments. The short and relatively deep channels resulted in a negligible pressure differential across the active area. When utilized with simultaneous neutron imaging, the active area plane was oriented parallel with the neutron beam such that accumulated liquid water content in the through-plane dimension could be quantified. PTFE seals were used to minimize neutron attenuation.

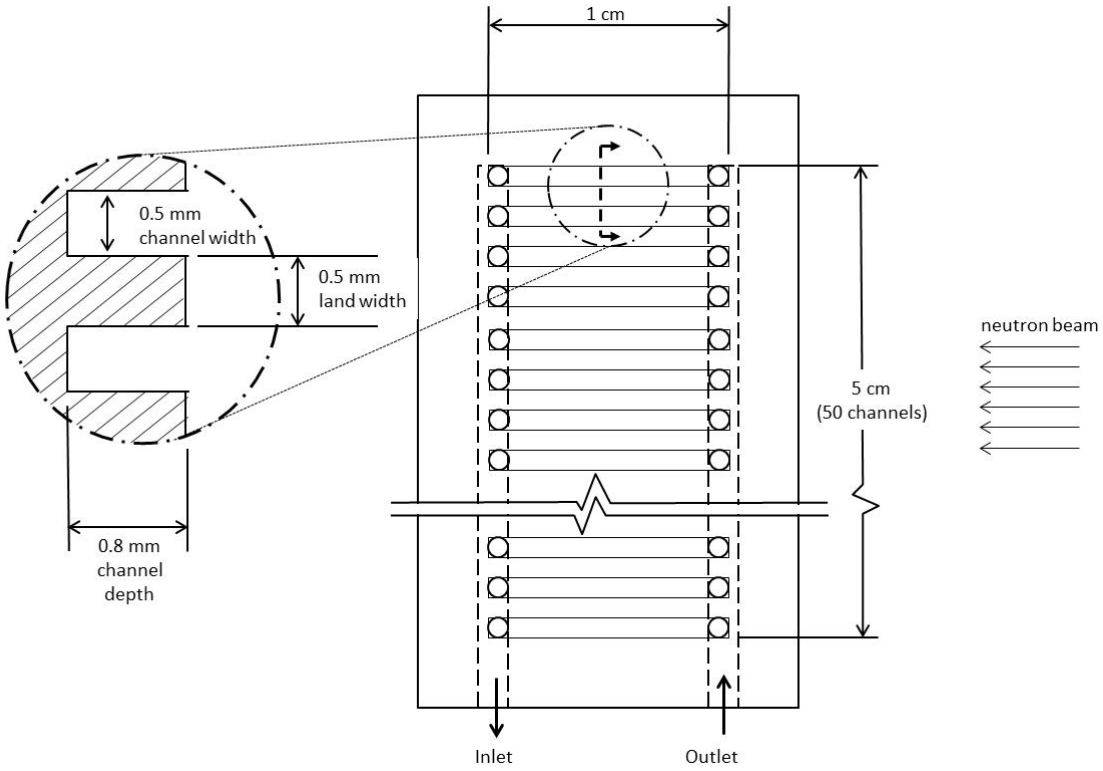

Figure 2.6: Differential cell experimental hardware channel and land geometry.

2.4 Materials

Two carbon fiber paper substrates were selected to consider through-plane thermal gradients. The impact of anode diffusion resistance required a new porous carbon substrate to be developed. All of these substrates were coated with the same microporous layer formulation. The porous carbon substrate with the MPL is called the gas diffusion layer (GDL) throughout this document. All GDL studies utilized the same type of membrane electrode assembly which was an 18 μm thick membrane with 0.2/0.3 mg Pt cm^{-2} anode/cathode catalyst loading electrodes attached manufactured by W.L. Gore.

Catalyst layer studies require custom electrode ink formulations and coatings. The Pt loading was monitored during the fabrication process and in the as-built samples. The resulting catalyst layer thickness and uniformity were also measured. All MEAs with a custom catalyst layer utilized the W. L. Gore 18 μm thick membrane.

2.4.1 Gas Diffusion Layers

Two GDL substrates with different thermal conductivities but similar diffusion resistances were selected to demonstrate how through-plane thermal gradients impact liquid water content in the GDL. By varying the GDL thermal conductivity the fuel cell water content could be altered at a given operating condition, thus establishing the correlation between liquid water quantity and membrane resistance. The high and low thermal conductivity GDLs selected for this study were Toray TGP-H-060 and Mitsubishi Rayon Corp. (MRC) Grafil U-105, respectively. Each sample was prepared with 7% wt. PTFE in the substrate and a 30 μm thick microporous layer consisting of a 8:1:1 carbon:PTFE:FEP ratio. The relevant measured parameters for the resulting GDLs are listed in Table 3. The GDLs were compressed to 20% strain based on the measured uncompressed thickness.

Table 3: Measured diffusion and thermal parameters for the GDL material studied [8] [19] [114].

Parameter	TGP-H-060	Grafil U-105	unit
Thermal Resistivity [13]	3.1 ± 0.3	9.2 ± 0.3	cm^2K/W
Effective Diffusion Coefficient [14]	0.036 ± 0.002	0.037 ± 0.002	cm^2/s
Uncompressed Thickness	225 ± 12	230 ± 10	μm
Resistivity [15]	7.8	13.3	$mOhm* cm^2$
Porosity	66%	73%	-

The high tortuosity anode GDL substrate was fabricated from PAN fibers, phenolic resin, graphite flake, and fibrillated acrylic pulp. The graphite flake, with high aspect ratio, becomes preferentially oriented in the x-y plane of the fiber mat during the laydown of a slurry consisting fiber, pulp and the flake, resulting in increased tortuosity in the z direction, as evidenced in the D/D_{eff} value in Table 4. Because of the high aspect ratio of the flake, the pulp is utilized as a way of anchoring the flake while maintaining low cost (mitigating use of more PAN fibers). Further, the addition of the non-conductive cellulose pulp does not decrease the electrical conductivity or increase thermal resistance; data for these values are shown in Table 4. Representative top down and cross sectional SEM images of this novel GDL are depicted in Figure 2.8.

Table 4: Comparison of key parameters for baseline and concept high diffusion resistance low cost GDLs.

Parameter	MRC U-105	High Tortuosity GDL
D/D_{eff}	2.8	19.1
Thickness (μm)	230	250
Electrical Conductivity (mOhm cm^2)	23	29
Thermal Resistivity (cm^2 K / W)	9.6	5.9

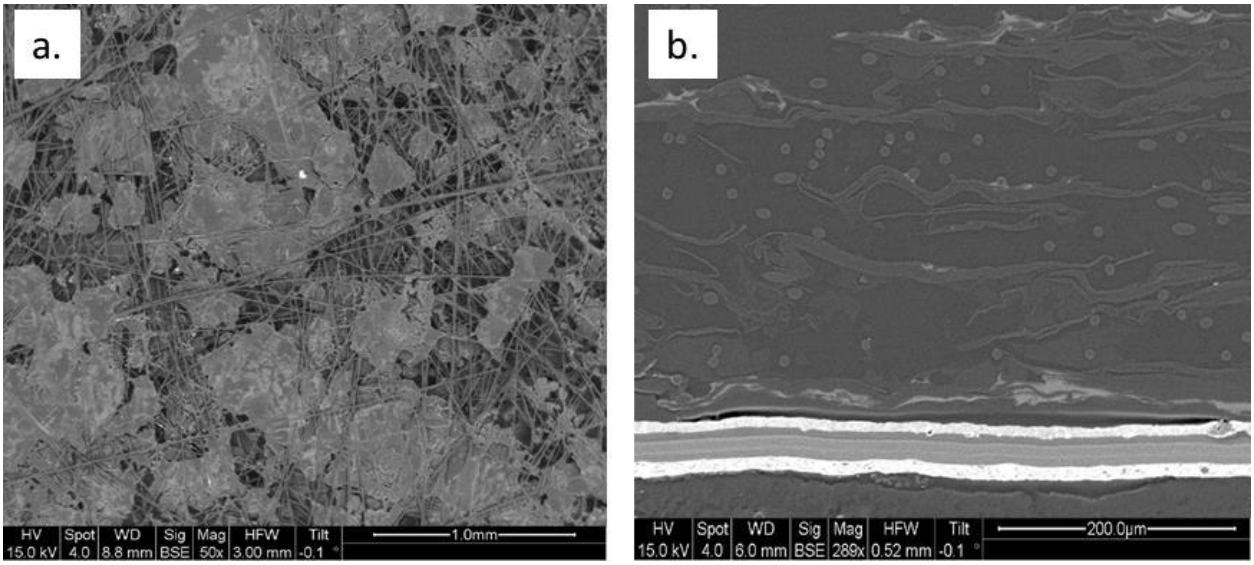

Figure 2.7: High tortuosity carbon fiber paper with platelets oriented in-plane, a.) top down SEM micrograph, b.) freeze fracture cross-sectional SEM micrograph

2.4.2 Varied Pt Dispersion in the Catalyst Layer

Table 5 details key experimental parameters that were constant during the dispersion study. All 5 cm^2 membrane electrode assemblies (MEAs) were fabricated using the decal transfer process, detailed previously [107]. However, all ionomer was kept in the acid form throughout fabrication procedure. Cathode electrodes at the following loadings were fabricated: 0.3, 0.2, 0.1, 0.05, and 0.025 mg_{Pt} cm^{-2}. Starting at 0.1 mg_{Pt} cm^{-2} and for all lower loadings, at least 2 types of cathode electrodes were made. The first was made from a 50 wt% Pt/Vulcan® catalyst and diluted with Vulcan® XC-72 carbon while the others consisted of one or more lower wt.% catalysts such that each carbon particle was platinized and a constant catalyst layer thickness could be maintained. All these electrodes were fabricated using either one or more of the following components: 5, 10, 15, 20, 30, and 50 wt% Pt/Vulcan® (TKK) and Vulcan®

carbon support, along with Dupont® D2020 ionomer at an ionomer to carbon weight ratio of 0.95. To further study the lowest loading, additional 0.025 mg_{Pt}/cm^2 electrodes were made by varying the amount of platinized carbon particles. Thickness was again maintained by adding the Vulcan carbon black to different %wt. Pt/Vulcan catalysts.

Table 5: Constant parameters in Pt dispersion studies

Parameter	Details
Anode Catalyst Layer	0.05mg Pt/cm2, 0.6 ionomer to carbon weight ratio electrode, comprised from a 20 wt% Pt/Vulcan XC-72® catalyst from Tanaka Kikinzoku Kogyo (TKK), Japan, and Nafion®® D2020 ionomer from Dupont (Dupont, USA)
Membrane	W.L. Gore 18 μm
MEA Lamination	146°C, 4 min, 18 kN
Gas Diffusion Layer	Mitsubishi Rayon Co. U-105 (5 wt.% PTFE) with MPL
Gas Flow Distributor	Straight pass, 0.5 mm channel width, 0.5 mm land width, 0.8 mm depth
Active Area	5 cm^2
Cathode Catalyst Layer Ionomer to Carbon	0.95 by weight
Compression	20% strain controlled with fixed displacement

A summary of all cathode catalyst layer formulations used in this study is provided in Table 6. Scanning electron microscope (SEM) images were taken of cross-sections from each decal in 3 locations (5 images per location, for a total of 15 thickness measurements per type) to estimate the catalyst layer thickness and uniformity, also given in Table 6. SEM images were also taken in field emission mode to contrast platinized from bare carbon and open structure. Example images from this SEM cross sectional analysis are given in Figure 2.8. The average cross-sectional area of platinized aggregates was estimated from the field emission SEM images (Figure 2.8b) by counting the number of adjacent high contrast pixels (due to local Pt content) and scaling based on pixel size (Figure 2.8c). This analysis demonstrated that the platinized aggregates have a similar average cross-sectional area and their distribution is uniform through the thickness of the catalyst layer for the various catalyst configurations used. With this established for constant thickness catalyst layers, the influence of wt% of Pt on Vulcan was probed with the assumption that gas phase transport resistance through the catalyst layer is constant in all samples.

Table 6: Catalyst layer formulation variables and SEM characterization.

		Catalyst Layer Formulation				SEM Characterization	
Sample	Pt Loading (mg cm^{-2})	Carbon Dilution	Catalyst Type; fraction of catalyst type in overall catalyst wt. Fraction	Catalyst Type; fraction of catalyst type in overall catalyst wt. Fraction	Bare Carbon wt. Fraction	Thickness (μm)	Average Platinized Aggregate Cross Sectional Area (μm^2)
1	0.3	No	50% Pt/V; 0.80	10% Pt/V; 0.20	-	9.7 ± 0.2	0.016
2	0.2	No	50% Pt/V; 0.56	20% Pt/V; 0.44	-	9.2 ± 0.8	0.014
3	0.1	No	15% Pt/V; 0.71	30% Pt/V; 0.29	-	10.4 ± 1.8	0.012
4	0.1	Yes	50% Pt/V; 0.42	-	0.58	10.9 ± 0.6	0.016
5	0.05	No	10% Pt/V; 1.0	-	-	11.2 ± 1.1	0.012
6	0.05	Yes	50% Pt/V; 0.22	-	0.78	13.1 ± 0.8	0.016
7	0.025	No	5% Pt/V; 1.0	-	-	11.0 ± 1.2	0.015
8	0.025	Yes	5% Pt/V; 0.34	10% Pt/V; 0.34	0.33	10.8 ± 0.3	0.015
9	0.025	Yes	10% Pt/V; 0.51	-	0.49	10.7 ± 0.5	0.012
10	0.025	Yes	15% Pt/V; 0.34	-	0.66	10.4 ± 0.4	0.011
11	0.025	Yes	30% Pt/V; 0.18	-	0.82	11.3 ± 0.5	0.013
12	0.025	Yes	50% Pt/V; 0.11	-	0.89	12.2 ± 0.8	0.016

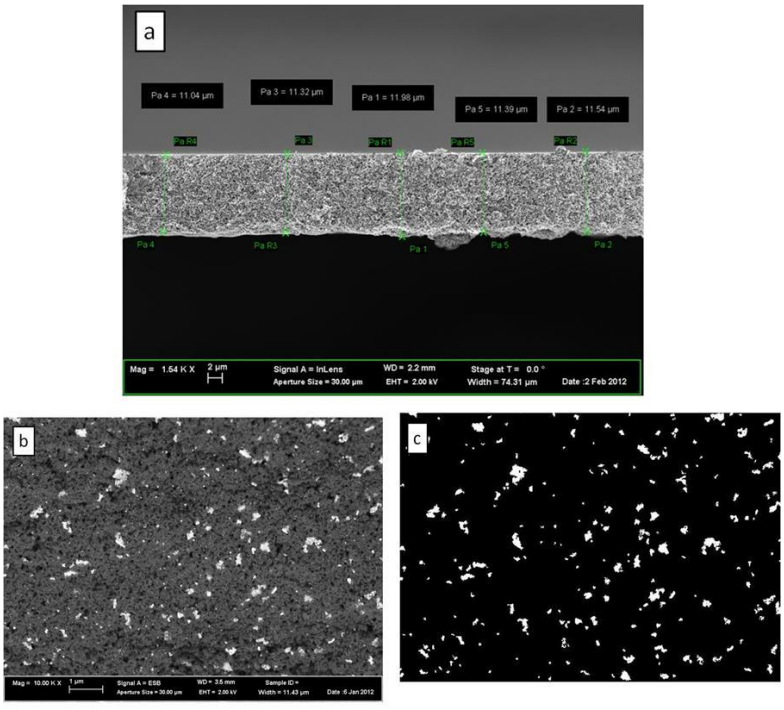

Figure 2.8: Freeze fracture SEM cross-sectional analysis of a.) thickness, b.) field emission mode contrasting Pt to C, c.) platinized aggregate size and distribution analysis. Shown for the 0.025 mgPt cm^{-2} catalyst layer.

2.4.3 Varied Ionomer Thickness in the Catalyst Layer

Cathode inks were fabricated with a 70wt% Pt/V XC-72® catalyst from Tanaka Kikinzoku Kogyo (TKK), Japan, and Nafion® D2020 ionomer from Dupont (Dupont, USA). Ionomer to carbon weight ratios were studied at the following levels: 1.0, 0.6, 0.4, and 0.2 at both 0.4mg Pt/cm^2 and 0.05 mg Pt/cm^2 loadings (eight total electrode variations). Because of the thin nature of both wet and resulting dry films of the low loaded parts, and the difficulties in decal transferring such films, all cathode inks were slot die coated directly onto the NRE 211 membrane. Resulting thicknesses of the cathode electrodes measured via SEM cross section can be viewed in Table 7. The anode electrode was added to all parts by the decal transfer method [107]. Anodes consisted of a 0.05mg Pt/cm^2, 0.6 ionomer to carbon weight ratio electrode, comprised from a 20wt% Pt/Vulcan XC-72® catalyst from TKK, Japan, and Nafion® D2020 ionomer from Dupont (Dupont, USA).

Table 7: Cathode electrode thickness measured by SEM cross-section (error is the standard deviation of 15 measurement points)

Sample	Cathode Loading (mg Pt/cm^2)	Ionomer:Carbon	Thickness (μm)
1	0.40	1.0	4.4 ± 0.3
2	0.05	1.0	0.8 ± 0.3
3	0.46	0.6	5.4 ± 0.1
4	0.05	0.6	0.8 ± 0.3
5	0.42	0.4	7.0 ± 0.1
6	0.04	0.4	0.7 ± 0.2
7	0.43	0.2	5.6 ± 0.2
8	0.05	0.2	0.7 ± 0.2

3. Chapter 3 – Impact of GDL Saturation

3.1 System Efficiency

The research outlined regarding transport resistance in PEFCs is focused on critical needs for characterizing state-of-the-art material sets and operating conditions. As transport loss is considered from the gas delivery channel to the Pt surface, the impact of liquid water saturation on diffusion resistance must be investigated in a manner that can be applied to existing model architectures. During these studies the impact of liquid water on proton resistance in the membrane was first considered as this relationship is the exclusive reason that PEFCs need to operate near saturated conditions where the problematic liquid water will exist. Next, the consequence of liquid water in the GDL relative to removal for shutdown was considered and a novel approach to managing the overall water balance was demonstrated.

3.1.1 Proton Transport Resistance Correlated to Liquid Water Content in GDLs

The GDLs being compared in this study were expected to exhibit different water accumulation behavior at higher temperature operating conditions due to the temperature gradient that exists between the coolant fluid and the cathode catalyst layer. As water condenses in the porous medium, the temperature gradient will dictate the location of the condensing liquid front. Hence, a lower temperature gradient will result in more liquid water volume, all else held constant (diffusion properties, for example). This behavior was confirmed with in-situ neutron imaging) by measuring the integrated liquid water thickness through all layers with the neutron beam perpendicular to the active area plane. Shown in Figure 3.1 and Figure 3.2 is a comparison of liquid water content and performance for the Toray and MRC GDLs at various current densities during a polarization curve acquired at 80°C cell temperature. The similar polarization performance with a nearly factor of two difference in liquid water volume indicates that GDL water content can have an insignificant influence on fuel cell performance for certain operating conditions.

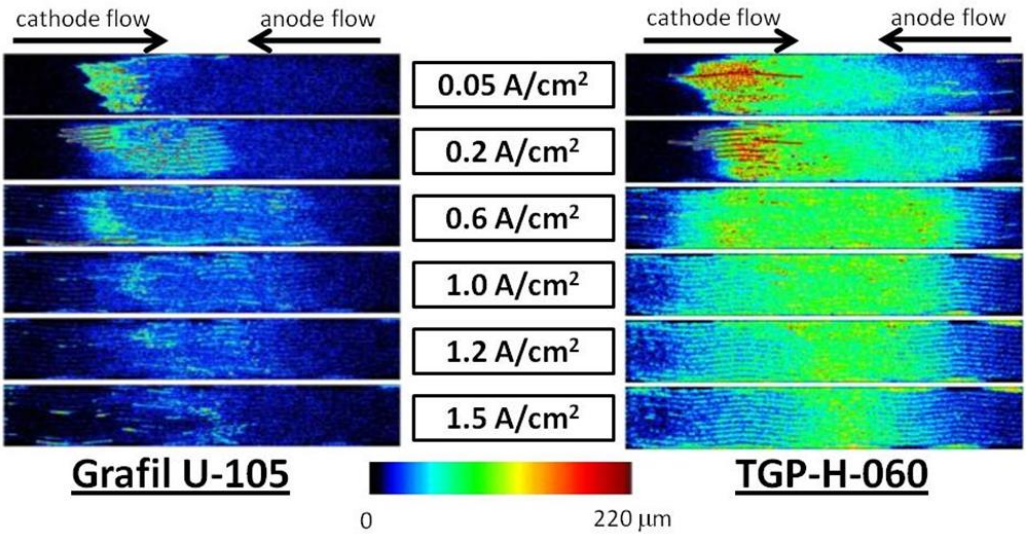

Figure 3.1: Comparison of liquid water accumulation in MRC and Toray GDL (80°C, 1.5/2.0 H_2/air stoichiometry, 95% inlet RH, 200 kPa abs. outlet pressure, counter-flow) [115].

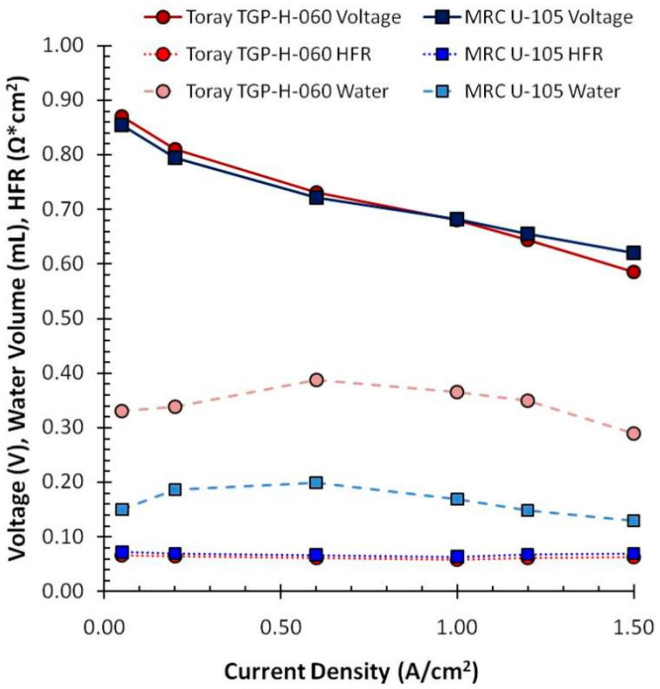

Figure 3.2: Performance comparison of Toray and MRC GDLs (80°C, 1.5/2.0 H_2/air stoichiometry, 95% inlet RH, 150 kPa abs. outlet pressure, counter-flow) [115].

The data shown in Figure 3.2 at 80°C demonstrate the contrast in liquid water accumulation due to the nonlinear relationship between saturation vapor pressure and temperature. As stated above, even though there is a factor of approximately two difference in water content at all current densities for

80°C cell temperature, the voltage and HFR measurements are nearly identical (Figure 3). Only at the 1.5 A cm^{-2} condition is there some evidence of greater mass transport loss in the cell with high thermal conductivity GDL material. To further demonstrate that water accumulation in the bulk of the GDL is mainly related to the induced temperature gradient between the cathode catalyst layer and coolant, the liquid water content at 35 and 80°C is presented in Figure 3.3. For each of these measured water distributions, the associated temperature gradients were calculated based on the thermal resistivities in Table 3 and the heat flux at 1.5 A cm^{-2} determined from the overpotentials in Figure 3.2. At 35°C, a difference of 1.5 kPa in saturation vapor pressure gradient results from temperature gradients of 2 and 6°C for Toray and MRC papers, respectively. Conversely, at 80°C the difference in induced temperature gradient for the two materials results in a difference of 8.8 kPa in saturation vapor pressure gradient. Consequently, the total water content for the Toray material is less dependent on cell temperature. However, the in-plane liquid water content along the channel direction is clearly influenced in Figure 3.3. At 80°C, the liquid water is more concentrated at the center of the active area while the anode and cathode inlet regions remain relatively dry. This temperature dependence is later used to consider variations in GDL water content at the same operating condition.

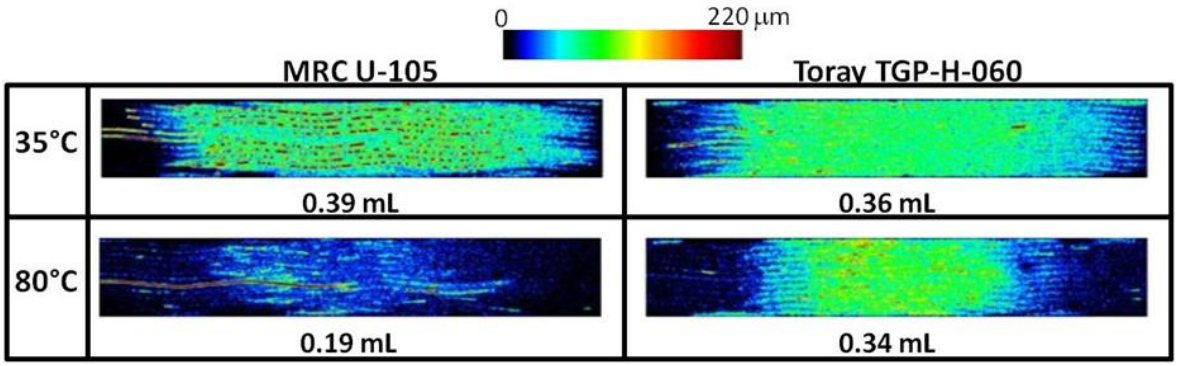

Figure 3.3: Impact of GDL induced thermal gradient on measured water volume at 35 and 80°C (0.4 A cm^{-2}, 1.5/2.0 H_2/air stoichiometry, 95% inlet RH, 150 kPa abs. outlet pressure, counter-flow) [115].

This relationship between accumulated water and performance was explored further by monitoring local HFR relative to liquid water content for the cell assembled with MRC GDL (Figure 3.4). Here, the neutron image was analyzed over discrete areas aligned with the segmentation of the current distribution tool shown in Figure 2.3. Each water thickness measurement is the integrated liquid water measured per pixel that is averaged over an area equivalent to the current measurement segment. The plot shown in Figure 3.4 demonstrates the strong dependence between bulk water in the GDL and

membrane proton resistance that is governed by its hydration level. For this plot, the gradient in water thickness values was achieved by preconditioning the cell at a wet condition (35°C, 0.4 A cm^{-2}, 150 kPa outlet pressure, 2/2 H_2/air stoichiometric ratios) then purging at a drier exit condition (35°C, 0.1 A cm^{-2}, 101 kPa outlet pressure, 2/16 H_2/air stoichiometric ratios). At this low temperature condition, the cathode purge dries the cell slowly (~10 minutes), thus allowing several levels of liquid water thickness to be captured with 30 s neutron integration times in each segment. The inset neutron images and distributed HFR in Figure 3.4 demonstrate this drying, as a front, moving from the cathode inlet to outlet during the length of the purge. These experiments were run under a wide array of conditions, and the same general trend in HFR was observed as integrated liquid water thickness decreased.

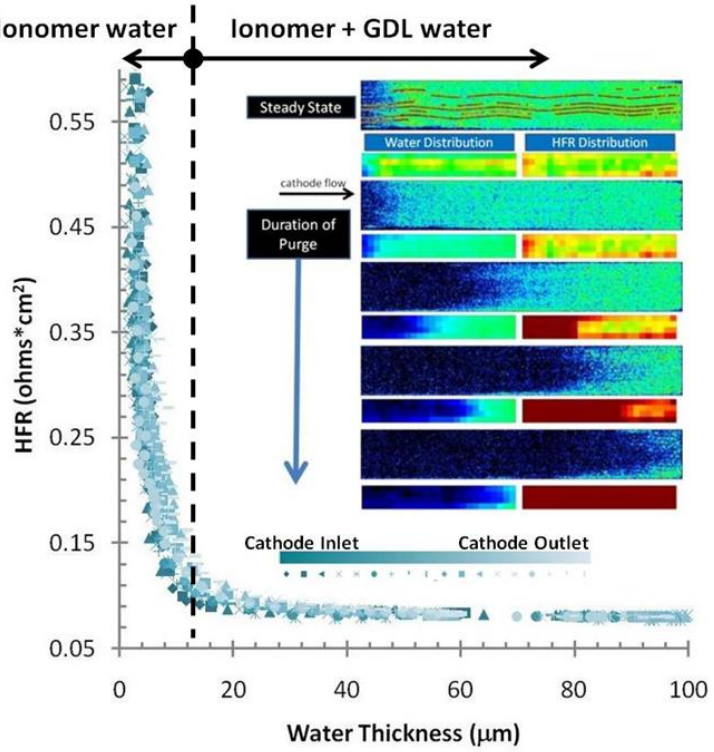

Figure 3.4: HFR response to local water thickness during a slow drying transient; liquid equilibrated equivalent liquid water thickness in the ionomer is indicated by the vertical dashed line. Neutron images, binned water thickness and HFR distributions that represent data are also shown. Precondition: 35°C, 0.4 A cm^{-2}, 150 kPa abs. outlet pressure, 2/2 H_2/air stoichiometric ratios; Drying condition: 35°C, 0.1 A cm^{-2}, 101 kPa abs. outlet pressure, 2/16 H_2/air stoichiometric ratios [115].

In Figure 3.4, the sharp increase in HFR as water thickness approaches a value that is associated with liquid equilibrated ionomer water content (an estimated 13 μm equivalent water thickness for the 950 equivalent weight membrane at 20 moles water per acid site) is somewhat obvious given the strong

dependence of the ionomer "lambda" value (number of water molecules per sulfonate site) on the phase of water. Similar observations regarding HFR response to purge under saturated conditions were made by Cho and Mench [116] [117] [118]. However, what is unique about these data is that the HFR asymptote indicates only a small amount of liquid water in the GDL is required to maintain the ionomer lambda value at a liquid equilibrated state.

Finally, the integrated water measurement presented thus far is ignoring the anode vs. cathode distribution in these two experimental configurations. To elucidate this we applied high resolution neutron imaging methods to measure the through-plane water content by orienting the cell such that the neutron path was parallel to the active area plane (Figure 2.4b). This comparison is provided in Figure 3.5, where integrated liquid water thickness is scaled to GDL saturation. Here it is observed that the increased overall water content with the Toray material is a result of both a change in the anode distribution, where more water is stored toward the anode flow field and an increase in cathode GDL liquid water content with a similar distribution. This result indicates a shift in the overall water balance, which correlates to the slower HFR response to purging, as the additional anode water removal by the cathode gas stream is slowed by the membrane. Also, an increase in anode water further complicates the trade-offs mentioned previously, because draining water from the anode subsystem can impact system efficiency.

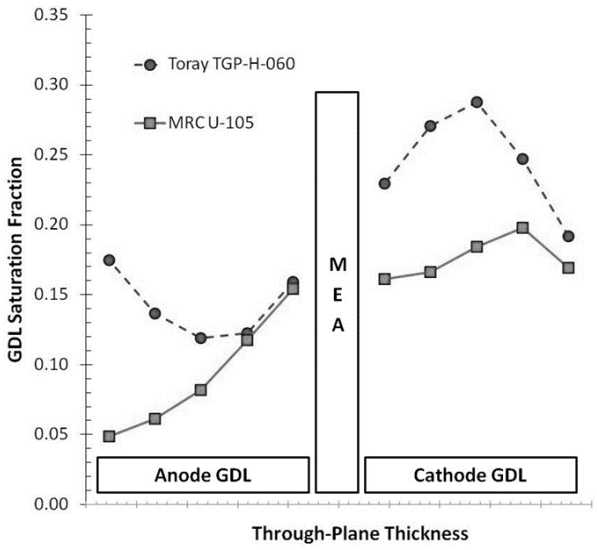

Figure 3.5: High resolution neutron imaging of through-plane water profiles for Toray (80°C, 0.6 A cm^{-2}, 4/4 H_2/air stoichiometry, 95% inlet RH, 150 kPa abs. outlet pressure, counter-flow) [115].

3.1.2 Accumulation and Removal of Liquid Water from the GDL

The work in Section 3.1.1 established that proton transport resistance is only minimized if liquid water is present in the GDL. This leads the research toward studying the consequence of liquid water accumulation. In this section, the removal mechanism is studied by purging the cathode with dry air. From this the relative role of convection and diffusion are considered ad an overall mass transfer coefficient is empirically derived. The first component of this portion of the study utilized GDL of a known saturation prior to each cell build. After the cell was assembled, a cathode purge was executed with simultaneous neutron imaging. The neutron radiographs were normalized by dry reference images according to the Lambert-Beer attenuation law, combined with the neutron cross-section for liquid water previously measured at the NIST experimental facility [119]. This analysis results in a spatially resolved water thickness that is multiplied by the physical area for presentation as volume. Each image has a liquid water volumetric uncertainty of about ± 0.01 mL.

The GDL was submersed in deionized water with the air pressure reduced to approximately 700 Pa. Before assembly of the saturated GDL into the 50 cm^2 fuel cell hardware, the volume of imbibed water was measured by weighing the GDL before and after saturation. The results shown in Table 8 indicate the 250 µm thick, 76% porous GDL substrate (as cited by manufacturer) was saturated to approximately 50% of open pore volume. As observed while weighing the saturated GDL, evaporation to the ambient was significant and this is thought to account for the loss later measured with neutron radiography.

Table 8: Initial ex-situ saturated water volume (pre-assembly) compared with neutron radiography measurement (post-assembly) (open volume prior to saturation = 0.95 mL).

	33°C Anode DM Saturated	33°C Cathode DM Saturated	76°C Anode DM Saturated	76°C Cathode DM Saturated
Initial water volume (scale)	0.537 mL	0.527 mL	0.531 mL	0.544 mL
Initial water volume (neutrons)	0.439 mL	0.433 mL	0.460 mL	0.466 mL

Once the assembled cell was at the appropriate temperature (33 or 76°C), the nitrogen gas purge with 1.0 slpm flow was engaged on the cathode side at ambient outlet pressure. Radiographs acquired during the purge were reduced to 10 second averages and water volumes for the entire active area were computed. These results for cathode purge configurations (as outlined in Table 2) are shown in

Figure 3.6, where the purge begins at 0 seconds and the removal rate is observed to be linear until nearly all water is removed. The nonlinear portion near the end of the purge is simply a result of the limited remaining water content, which yields under-saturated purge flow exiting the system. For the entire active area, water removal rates at 33°C are similar regardless of the location of liquid water (anode vs. cathode), whereas at 76°C the drying behavior is measurably different. A qualitative comparison of the 33°C cases indicates a similar drying profile for the anode saturated GDL with cathode purge and the cathode saturated GDL with cathode purge (Figure 3.7). One may observe that the only clear difference between these two configurations is the stream-wise length of the "drying zone", i.e., the region over which the GDL changes from being fully dry to its initial saturation state. At 33°C, the drying zone is shorter than the channel, but at 76°C it is longer, which results in a difference in bulk drying behavior. These factors are addressed in more detail later in the discussion of differential analysis.

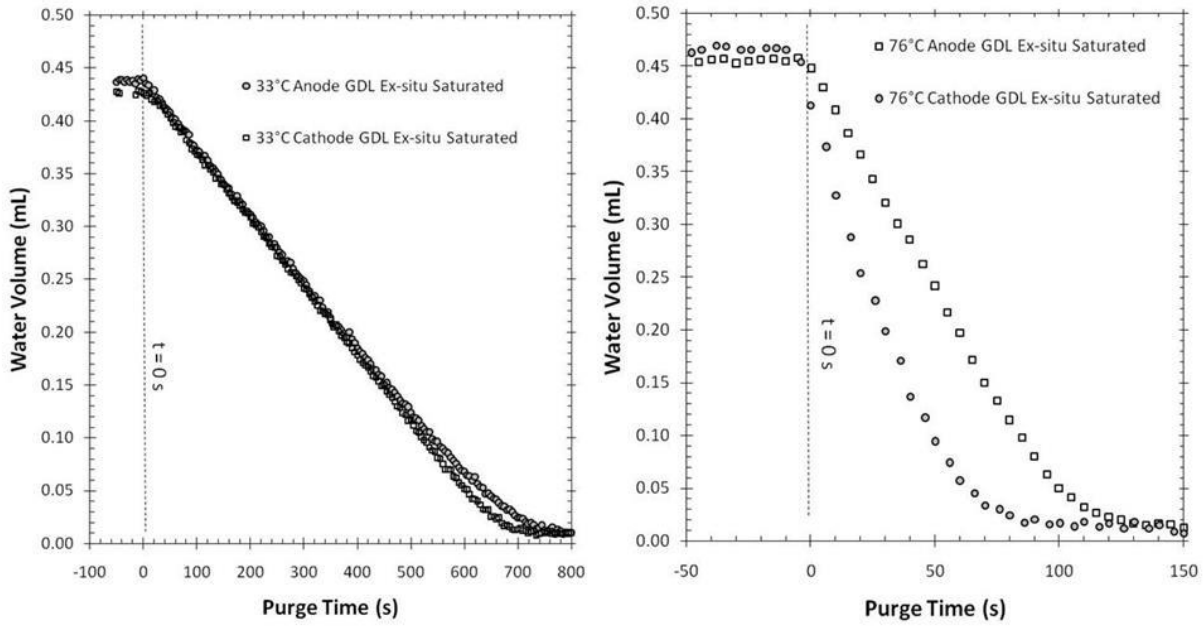

Figure 3.6: Ex-situ saturated GDL water removal during 1.0 slpm nitrogen purge at 101 kPa [120].

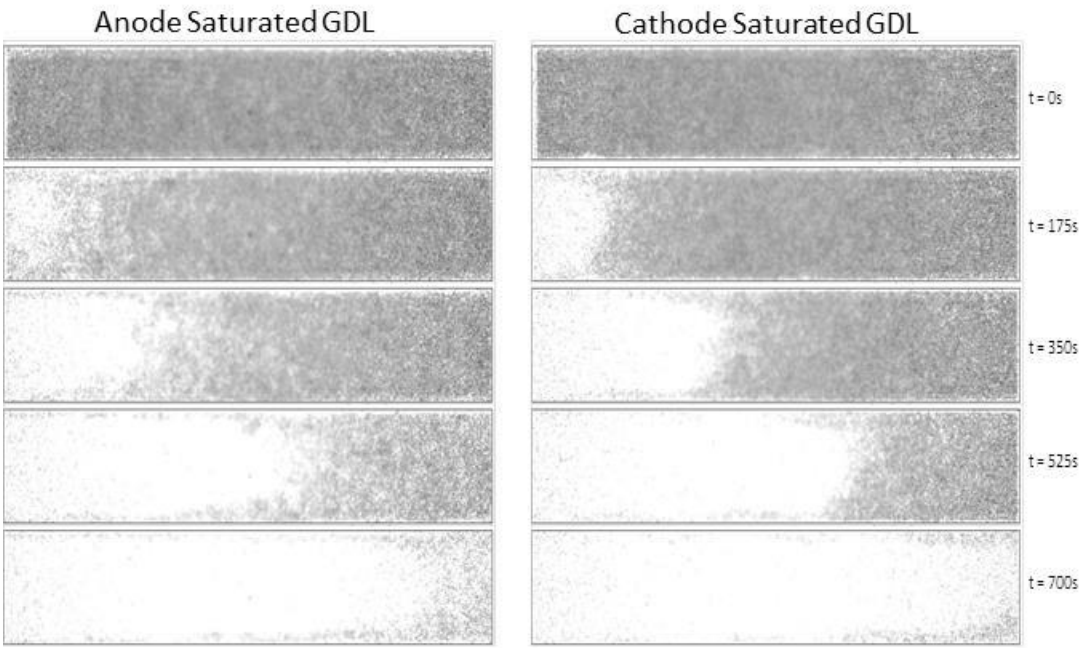

Figure 3.7: Radiographs of drying profile for anode (left) and cathode (right) saturated GDL with a cathode nitrogen purge at 1 slpm, 33°C and 101 kPa [120].

The linearity of water removal indicates a purely evaporative removal mechanism, as pressure driven flow in porous media is nonlinear for the given pore size range in the GDL substrate (10-50 μm). If a convective removal mechanism had a significant influence on liquid water removal, one would expect a sudden drop in water content at the onset of the purge when the large (i.e., lower pressure drop) pores were cleared of water. Furthermore, an evaporative mechanism can be evaluated by the vapor flux associated with the saturation fraction of the gas stream for cases where the drying zone is shorter than the active area. During the 33°C purge case, the gas stream can carry a maximum water volumetric flow of $6.7*10^{-4}$ mL/s, which correlates within 10% to the removal rate of $6.4*10^{-4}$ mL/s measured in both the anode and cathode saturated GDL experiments.

Ex-situ purge experiments demonstrate that diffusive transport resistance limits water removal from the GDL regardless of its location in either the anode or cathode GDL. To further investigate and confirm these initial measurements, purge experiments from an in-situ generated saturation state were executed. In these experiments, water accumulation was found to be a direct result of electrochemical water production and condensation as gas concentrations changed due to reactant consumption. Unlike the ex-situ experiments, liquid water in the flow field channels (primarily on the anode) was frequently observed. Liquid water slugs would complicate the water removal rate measurement as they

were observed to exist beyond the measurement area, thus enabling liquid water to flow back into the active area during purge. To mitigate these slugs, a brief anode and cathode channel purge was executed with a rapid release of test stand pressure from 150 kPa to ambient (estimated 5 slpm flow for < 1.0 second). This initial purge effectively removed all channel water prior to the controlled purge experiment, with minimal impact on GDL water content. An example of this procedure is shown in Figure 3.8 where the water slugs are immediately removed from the initial water state, resulting from steady-state precondition of 0.4 A/cm^2, 33°C, 150 kPa outlet pressures with bypassed humidifiers. Aside from simplifying the experimental procedure and data analysis, initial removal of channel water via pressure release has obvious practical benefits. Otherwise, anode channel water could only be removed via diffusive transport through the MEA to the cathode purge stream, thus significantly increasing purge time and energy.

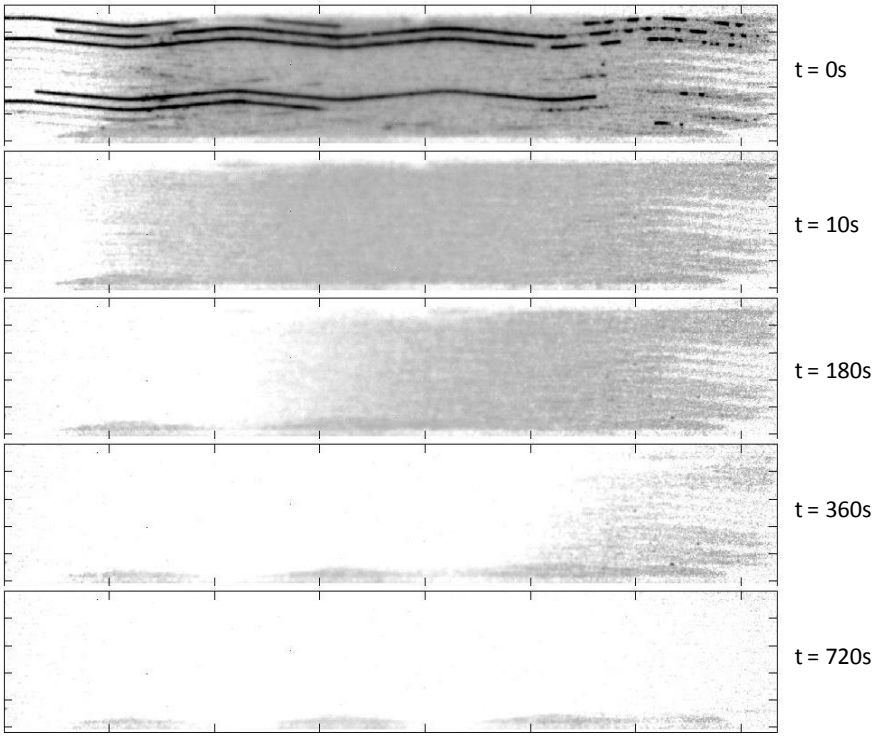

Figure 3.8: Purge of in-situ accumulated water with pressure release at 1s to remove channel liquid water slugs, followed by cathode nitrogen purge at 1 slpm, 33°C and 101 kPa. Shutdown conditions: 0.4 A cm^{-2}, 33°C, 150 kPa, 2/2 stoichiometric ratios, with no external humidification [120].

In Figure 3.9 the in-situ and ex-situ drying profiles resulting from purges at 33 and 76°C are compared. In-situ preconditions produced GDL saturation fractions that are lower than those from the ex-situ saturation procedure, as a result of steady-state GDL saturation fraction for the in-situ conditions at 0.4

A/cm^2 being less than the saturation achieved in vacuum for ex-situ experiments. Despite differences in how the GDL was saturated, the rate at which water is removed is comparable among all saturation methods at 33°C (6.0*10^{-4} mL/s both for in-situ saturated, 6.4*10^{-4} mL/s both for ex-situ saturated anode or cathode GDL). At 76°C the removal rate of 4.0*10^{-3} mL/s measured from the in-situ saturated condition closely compares with the rate measured ex-situ with anode GDL water and a cathode purge (4.1*10^{-3} mL/s). This result indicates that the location of saturation during the precondition at 76°C is primarily in the anode GDL, whereas if the majority of saturation were in the cathode GDL one would expect a faster removal rate as observed in the ex-situ configuration with a saturated cathode GDL (Figure 3.6).

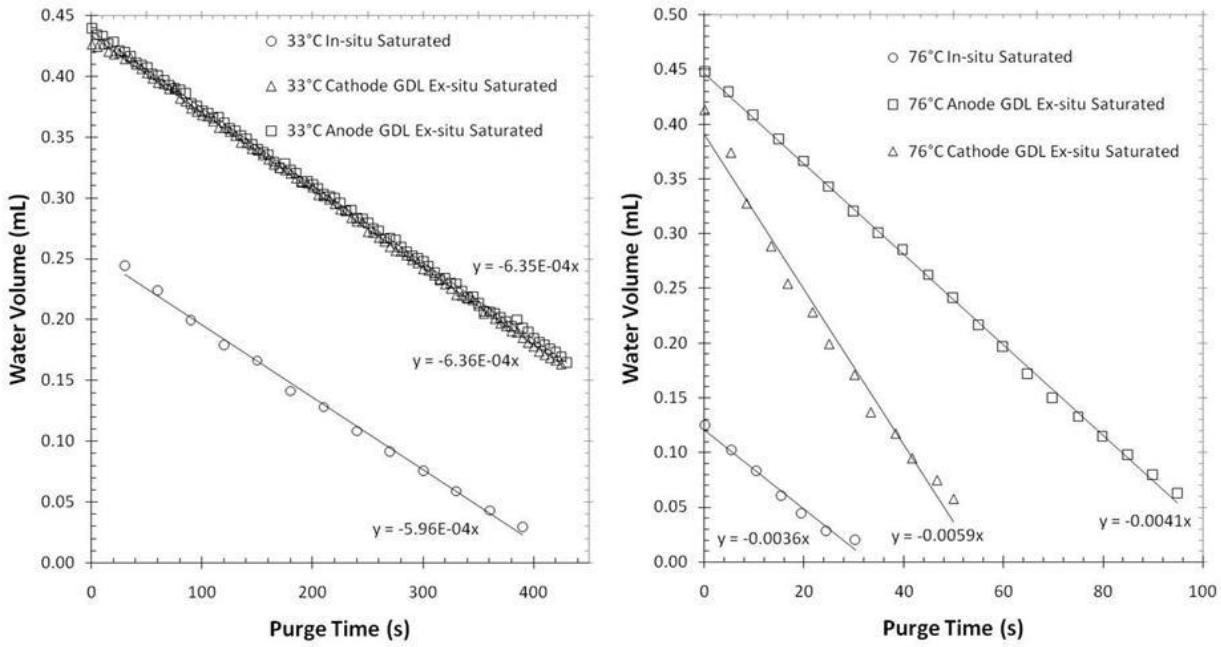

Figure 3.9: In-situ saturated cell compared with ex-situ saturated purge results, with cathode nitrogen purge of 1 splm at 101 kPa for all experiments [120].

Additional in-situ purge experiments were conducted at decreasing purge flow rates. These water removal rates are compared with the average ex-situ saturated anode GDL with cathode purge values in Figure 3.10. All data points are based on the average results from three experiments, with error bars representing measured maxima and minima. The precondition (0.4 A/cm^2, 150 kPa outlet pressures, 2/2 stoichiometric ratios, 50% inlet RH at 76°C, and bypassed humidifiers at 33°C) for in-situ saturated experiments is consistent for all purge data in Figure 3.10. These measurements also demonstrate the existence of an evaporative drying mechanism as water removal varies linearly with purge flow rate.

The theoretical water removal rate for a saturated exhaust is also shown in Figure 3.10 to illustrate the linear impact of mass transport resistance at the temperatures investigated. Although Figure 3.10 suggests that a purge is more efficient at lower temperatures, if one normalizes by the saturation pressure gradient of the purge relative to saturation of the liquid interface, the difference in efficiency is negligible.

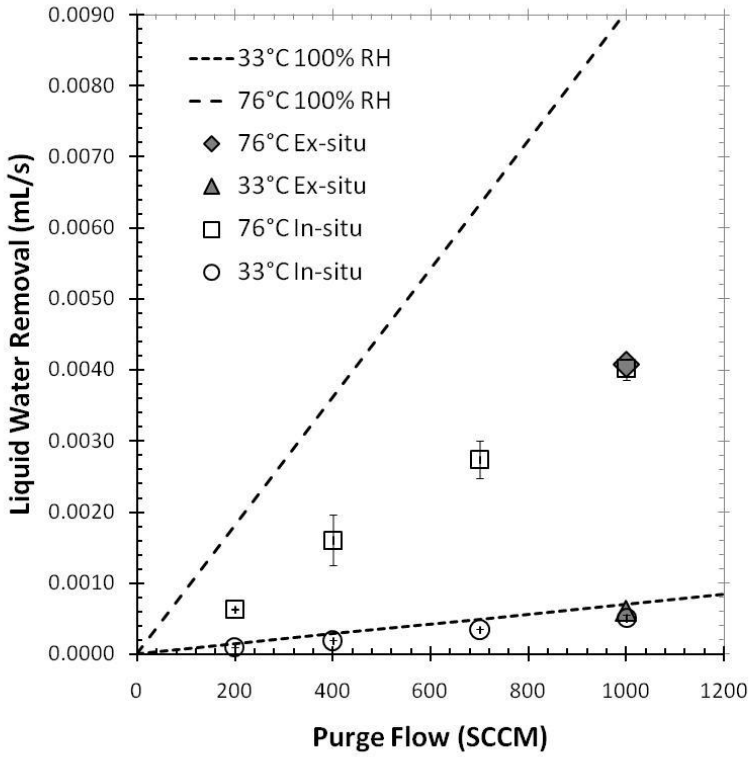

Figure 3.10: In-situ drying rates with dry nitrogen at decreasing cathode purge flows and comparison to ex-situ saturated anode GDL results at 1.0 slpm and 101 kPa [120].

Through bulk analysis it has been established that water removal during purge is limited by the saturation fraction of the purge gas stream at low temperatures, regardless of its location in either the anode or cathode GDL, because the purge flow exits the cell at 100% RH. At higher temperatures, transport resistance through the various layers has a significant impact on vapor uptake in the purge flow. The interaction among material layers and channel vapor transport resistance has strong temperature dependence due to the nonlinear increase in saturation vapor pressure with temperature. In the bulk analysis, this relationship is elucidated only once the channel exit relative humidity falls

below 100%, thus indicating that a differential RH analysis along the flow channel direction can be used to separate the membrane vapor transfer rate from the channel saturation effect.

Analyzing the neutron radiography data over a short flow length enables one to assume there is little change in channel RH in the stream-wise direction over the measurement area. Effectively differential test conditions were investigated by separating each matrix of water volume values (i.e., analyzed radiograph pixels) along the channel length, thus producing individual segment lengths of 1.25 mm. The water volume in each segment was summed vertically across all channels (Figure 2.5) and reported with a temporal resolution of 5 seconds. A representative plot from this analysis for the ex-situ saturated cathode GDL with cathode purge at 33°C is shown in Figure 3.11. Here the propagation of the saturation front is clearly observed as a function of purge length. Every segment except the first has an inflection point in the initial portion of the purge profile, due to the saturation of the gas flow upstream of the measurement point. However, the response of each segment eventually reaches a linear region that represents the maximum and constant drying rate for a given purge condition that occurs once all upstream water is removed. Data from the constant drying rate regions for various segments along the channel length are shown in Figure 3.11.

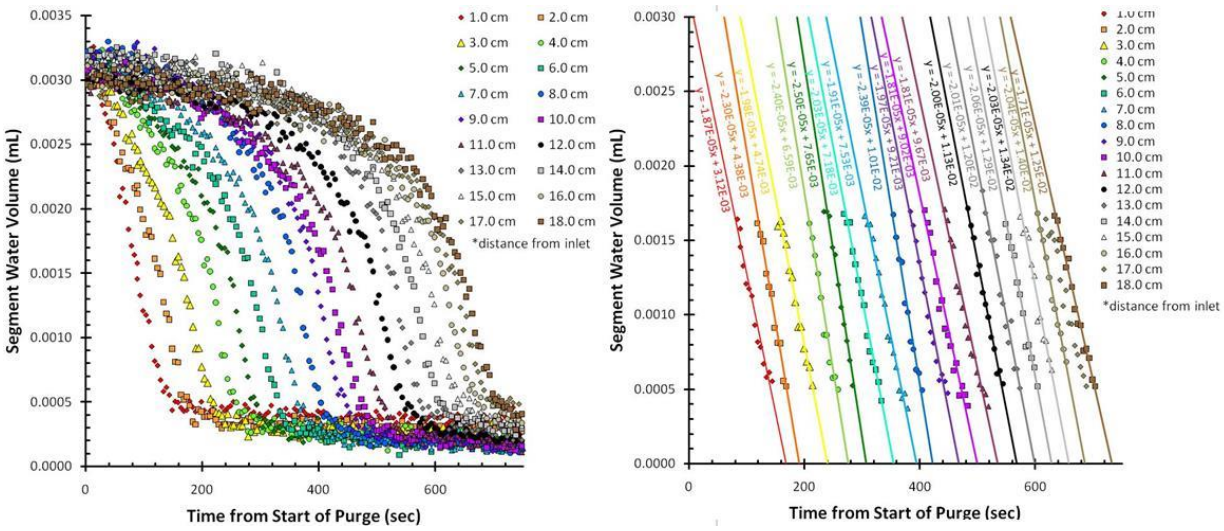

Figure 3.11: Segmented (1.25 mm wide at every 1.0 cm along channel length) analysis of water removal during purge from ex-situ saturated cathode GDL with a cathode nitrogen purge at 1 slpm, 33°C and 101 kPa. Constant drying rate portion is isolated in the right plot [120].

The same analysis was conducted for the remaining three ex-situ configurations (described in Table 2) and the average water removal rates from the 1.25 mm x 27.3 mm measurement segments are given in Table 9. This analysis also enables one to measure the stream-wise length of the drying front as it

moves from the cathode inlet to outlet during the purge. The 33°C anode saturated GDL case is compared to the cathode saturated case after 330 seconds of purge drying in Figure 3.12. Here the length of the drying front is measured as the distance between a nearly dry segment and one that has just begun drying (i.e., at its initial saturation state).

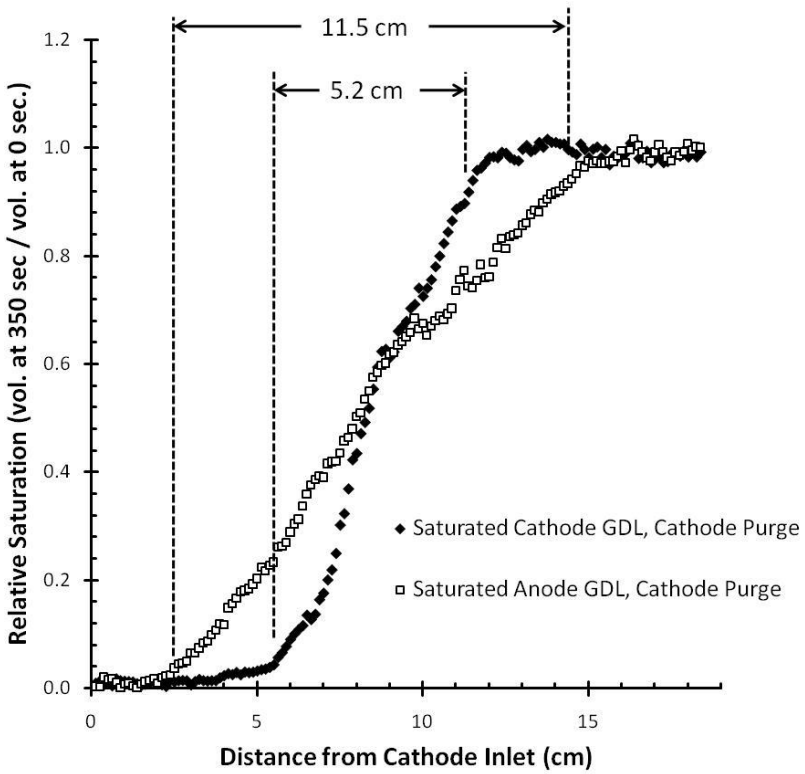

Figure 3.12: Measurement of drying front length after 330 seconds after start of cathode nitrogen purge at 1 slpm, 33°C and 101 kPa [120].

The data provided in Table 9 enable one to distinguish between anode and cathode GDL drying during in-situ saturated purge experiments. At 33 and 76°C with dry cathode purge flow, liquid water removal from the anode GDL through the membrane is measured to be 56% and 63% slower, respectively, than removing liquid water directly from the cathode GDL. Furthermore, the relative lengths of the drying fronts helps explain the similarity in bulk drying rates observed at 33°C and the variation at 76°C shown in Figure 3.6. With a saturated anode GDL at 76°C, the drying front length is longer than the stream-wise GDL length, resulting in an exit RH of less than 100% for the entire purge duration.

Table 9: Average differential water removal rates and standard deviations for ex-situ saturated GDL purge experiments, with segment area = 34.1 mm^2.

Temperature	Ex-situ Saturated GDL	Differential Removal Rate (μL/s)	Drying Front Length after 330 s purge (cm)
33°C	Cathode	0.0203 ± 0.0023	5.2 ± 0.3
33°C	Anode	0.0090 ± 0.0011	11.5 ± 0.3
76°C	Cathode	0.0758 ± 0.0076	15.7 ± 0.5
76°C	Anode	0.0283 ± 0.0017	>18.3

The preceding experimental work and analysis was developed as a diagnostic method to determine the location of water in the anode versus cathode GDL. These results were then compared to the differential removal rates during purges that follow in-situ preconditions. For consistency, in-situ and ex-situ comparisons were made at the same temperature, pressure, and purge flow (33/76°C, 101 kPa, and 1.0 slpm nitrogen, respectively). The differential removal rates and the drying zone length resulting from an in-situ precondition saturation state are shown in Table 10. These data correlate within 10% of those measured for an anode saturated GDL (Table 9), thus indicating the cathode GDL saturation content is low in comparison to the anode during fuel cell operation at these conditions.

Table 10: Average differential water removal rates for in-situ saturated cell (shutdown condition: 0.4 A/cm^2, 2/2 stoichiometric ratio, 150 kPa outlet pressure, inlet RH: dry at 33°C, 50% at 76°C, followed by a 1.0 slpm nitrogen purge at same temperatures).

Temperature	Differential Removal Rate (μL/s)	Drying Front Length (cm)
33°C	0.010 ± 0.0011	10.8 ± 0.4
76°C	0.0281 ± 0.0037	>18.3

As described earlier, the present work is based upon a test section design that simulates a full-scale automotive fuel cell. The majority of liquid water being in the anode GDL under representative PEFC operating conditions is a significant result that must be considered in ongoing GDL water management research. Moreover, the current work elucidates the water balance mechanism which enables this saturation state, as the measured water transfer rates indicate the membrane facilitates efficient water transfer if a concentration gradient is present. When the anode gas stream is introduced at a practical stoichiometric ratio in counter-flow, it equilibrates quickly with the cathode outlet RH condition. A similar water transfer across the MEA occurs at the cathode inlet, as indicated by the relatively low saturation level near the anode and cathode inlets shown in Figure 3.8 at t = 0 seconds. After the anode gas stream reaches 100% RH (if liquid water is present in the cell), condensation will occur as hydrogen

is consumed. For anode condensation to occur in counter-flow operation the cathode condition must enable the cathode water concentration to first exceed saturation and water in excess of the cathode saturation state must be of a quantity high enough to saturate the anode exhaust. A simple water balance (Equation 17) can be used to establish the anode outlet condition if one assumes water can move quickly from cathode to anode (as indicated by the current experiments)

$$\dot{m}_{w,An,out} = \dot{m}_{w,Prod} + \dot{m}_{w,Ca,in} + \dot{m}_{w,An,in} - \dot{m}_{w,Ca,sat} \quad , \qquad (17)$$

where $\dot{m}_{w,Prod}$ is the water mass production rate, $\dot{m}_{w,Ca,in}$ and $\dot{m}_{w,An,in}$ are the water mass flows entering with the cathode and anode streams, respectively, and $\dot{m}_{w,Ca,sat}$ is the outlet water flow in the cathode, assuming full saturation. After this water balance is satisfied, if $\dot{m}_{w,An,out}$ exceeds saturation, the rate of condensation in the anode is proportional to the change in volumetric flow from inlet to outlet (hydrogen stoichiometric ratio).

Applying this one-dimensional water balance based on channel conditions indicates that condensation in the anode will occur at a rate of 0.25 μL/s at 76°C and 0.06 μL/s at 33°C. These rates are conservative as they are an approximations based on outlet conditions; in reality the through-plane temperature gradient between the MEA and flow distributor would elevate this rate due to the higher saturation pressure adjacent to the ionomer. However, for the proceeding analysis of drying mechanisms it is sufficient to establish the mechanism by which the anode GDL accumulates liquid water during steady state operation.

A major element of this water balance that is not addressed here is liquid water in the cathode volume where the anode gas is saturated and no back diffusion driving force exists. Water removal from the cathode GDL is thought to be assisted by additional convective mechanisms, resulting from the relatively high outlet flow, pressure induced over-land flow and capillary pressure associated with water generation. These elements are crucial for a comprehensive two-phase model; however, they are beyond the scope of the current work, which focuses on the anode side accumulation mechanism that has been observed to be the primary zone of water accumulation in the GDL.

Anode condensation will occur frequently at start-up and during normal operation where optimal performance is typically achieved with the cathode exhaust relative humidity equal to or greater than 100% as proton transfer resistance in the ionomer is minimized. Conversely, excess liquid water will cause flow maldistributions and flooding of the porous layers, especially if in the form of ice at startup.

To enable a frozen start, liquid water blocking the channels must be removed at shutdown to mitigate local reactant starvation, and the MEA water content must be reduced, so that the water capacity in the ionomer and electrode is sufficient to prevent ice formation from blocking gas diffusion during operation at sub-frozen temperatures (start-up) [121]. However, before the ionomer and electrode water content can be reduced, the adjacent GDL must be substantially dry.

Thus far it has been established that liquid water can be convectively removed from the channels, but water removal from the GDL and MEA is purely evaporative during a purge with practical air flow. Additionally we have identified the effect of anode GDL saturation due to condensation and how this phenomenon limits the rate of water removal during cathode purge due to MEA transport resistance. This knowledge can be combined to characterize water removal during purge. For the simplest case where the purge gas exits fully saturated, the time of purge (t_p) can be estimated based on a step change in the exiting RH from 100%:

$$t_p = \frac{m_w}{\dot{m}_{p,sat}} \quad , \tag{18}$$

where m_w is total accumulated water mass, and $\dot{m}_{p,sat}$ is mass flow rate of water removed by the cathode purge stream exiting at full saturation. The step change in RH is an approximation because the water removal rate will decrease near the end of the purge process where the saturation length becomes shorter than the length of the drying zone; this is evidenced by the non-linearity near full dry-out in Figure 3.6 and Figure 3.11.

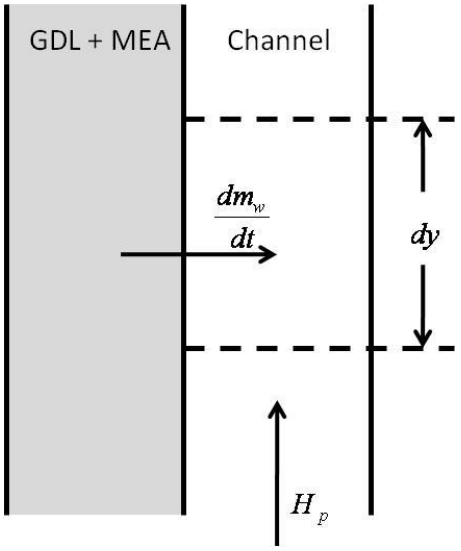

Figure 3.13: Schematic of water mass balance for liquid water removal from GDL and MEA during purge [120].

At normal operating temperatures and high purge flow rates, the drying zone will exceed the channel length for all or most of the purge duration and the previous approximation thus is not valid. For a more general solution, a material balance for the transfer of water from the porous layers and ionomer into the purge gas (Figure 3.13) is applied for a constant drying rate [122]

$$\frac{dm_w}{dt} = -KV_{GDL}\left(H_{GDL} - H_p\right) = -\frac{\dot{m}_p V_{GDL}}{A_{chan}}\frac{dH_P}{dy} \qquad (19)$$

where $\frac{dm_w}{dt}$ is the mass rate of water removal, K is the overall mass transfer coefficient, $V_{GDL}$is the open volume of the GDL, H_{GDL} is the specific humidity at the surface of the GDL, H_p is the specific humidity of the purge stream, and A_{chan} is the total channel flow area. From the right hand terms of Equation 19, the humidity variation along the channel (y) may be written as

$$\frac{dH_P}{dy} = \frac{KA_{chan}}{\dot{m}_p}(H_c - H_P) \quad , \qquad (20)$$

in which H_c is constant saturated specific humidity at the GDL surface for constant rate drying. The solution of Equation 20 is

$$H_p = H_c + (H_{in} - H_c)e^{-\frac{KA}{\dot{m}_p}y} \quad , \qquad (21)$$

where H_{in} is the specific humidity of the inlet purge gas. Combining the left hand terms of Equation 19 with Equation 21 leads to the partial differential equation:

$$\left(\frac{\partial m_w}{\partial t}\right)_y = -KV_{GDL}(H_c - H_{in})e^{-\frac{KA}{\dot{m}_p}y} \quad . \qquad (22)$$

The solution to Equation 22 is

$$m_w(y,t) = m_{w,o}(y,0) - KV_{GDL}(H_c - H_{in})te^{-\frac{KA}{\dot{m}_p}y} \quad , \qquad (23)$$

with initial conditions $m_w = m_{w,o}$ at $t = 0$ for all values of y. Next, the mass transfer coefficient can be determined using Equation 22 from the experimental data given in Figure 3.10 for a given drying zone. A least squares fit to these data results in a mass transfer coefficient of K = $7.5*10^{-3}$ g s^{-1} cm^{-3}, which predicts all purge data at both 33°C and 76°C within a 20% variation, as shown in Figure 3.14. This simple correlation demonstrates that a constant rate drying approximation can be used to predict bulk water removal in PEMFCs from a wide variety of shutdown and purge conditions. The observed data scatter is thought to be caused mainly by the presence of a temperature gradient along the channels, which results in a y-dimension variation in the saturated specific humidity.

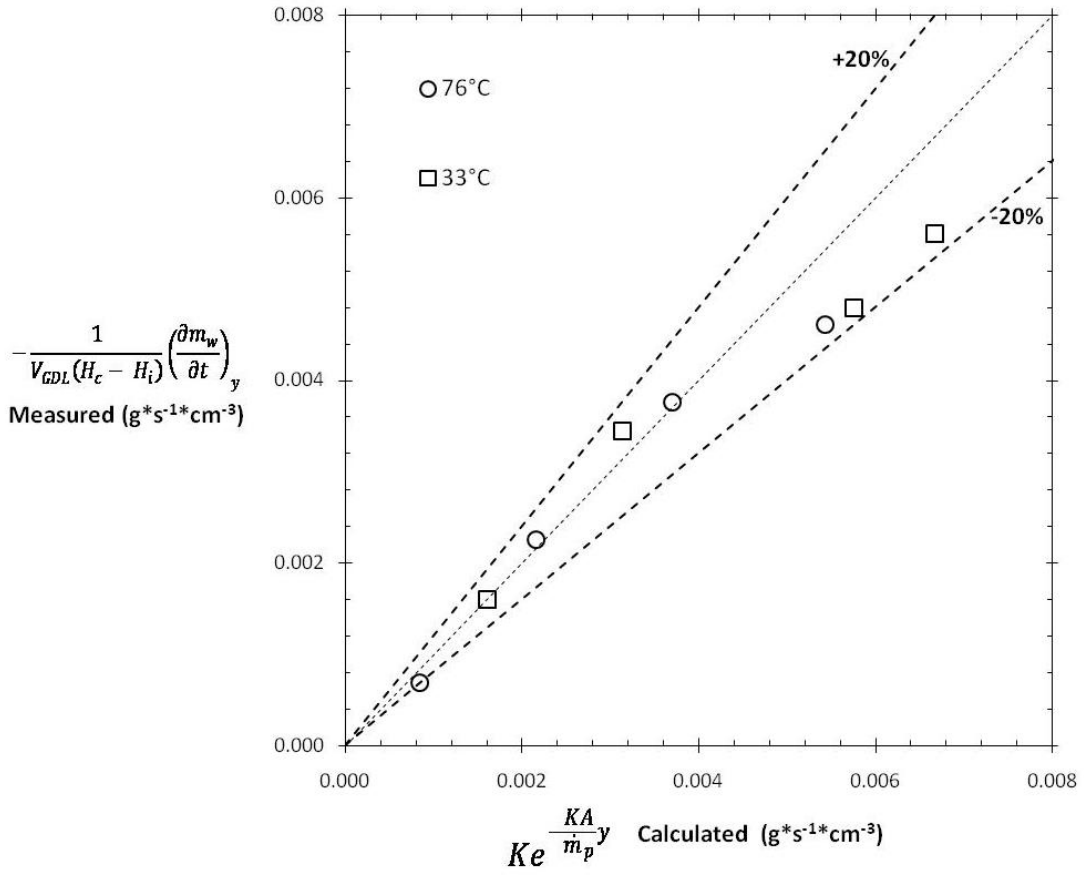

Figure 3.14: Purge data at 33 and 76°C (from Figure 3.10) fit to Equation 22 with K = 7.5*10-3 g s^{-1} cm^{-3} [120].

3.2 Novel Materials Approach to Water Management

The results obtained in Section 3.1.2 highlight the benefit of reduced water accumulation in the anode GDL for shutdown preparation of PEFCs. Since condensation in the anode volume is a result of water vapor diffusion from the anode, a logical mitigation strategy would be to run the cathode drier to shift the water balance. However, as shown in Section 3.1.1, some liquid water content is necessary to minimize proton transport resistance through the membrane. These two results combined lead to the passive material solution outlined in Section 2.4.1.

3.2.1 High Tortuosity GDL Performance

To demonstrate this material and the theory involved with development, a series of performance experiments that compared a symmetric to an asymmetric configuration (where the high diffusion resistance paper was used only on the anode side) were executed. Dry and wet results from this study are show in Figure 3.15. These results clearly indicate that the high diffusion resistance GDL cannot be applied to the cathode without a significant performance trade-off. However, the results in Figure 3.15 demonstrate this material can be used on the anode side if a standard GDL (MRC-105) is used on the cathode. In fact, under dry conditions the performance increased due to improved membrane hydration.

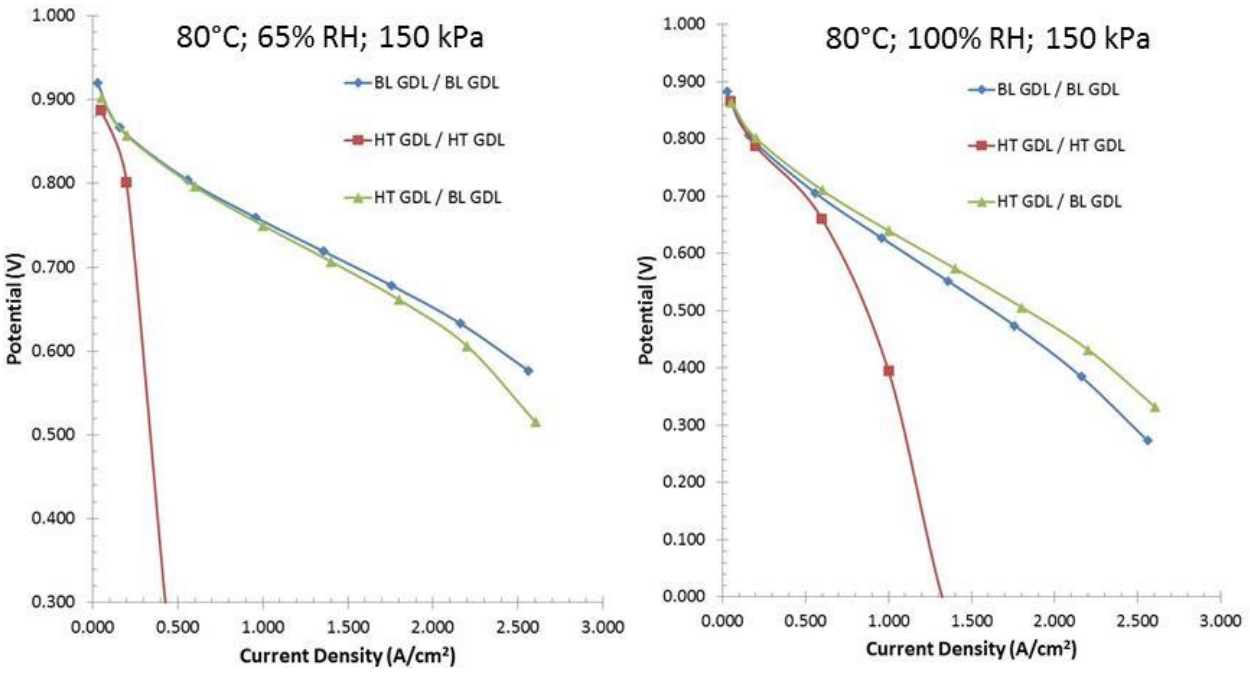

Figure 3.15: Dry (left) and wet (right) performance of high diffusion resistance anode GDL concept configurations compared with the baseline GDL. HT- High Tortuosity, BL – Baseline (MRC-105) [123].

The sensitivity between wet and dry performance was further investigated by varying the inlet relative humidity at high current density. As shown in Figure 3.16, the high diffusion resistance anode GDL configuration also demonstrates improved robustness to variations in operating conditions. Improved performance during transients between dry and wet conditions is of particular interest for PEFC systems as high load demands are often initiated by a dry transition as humidification tends to lag flow increases.

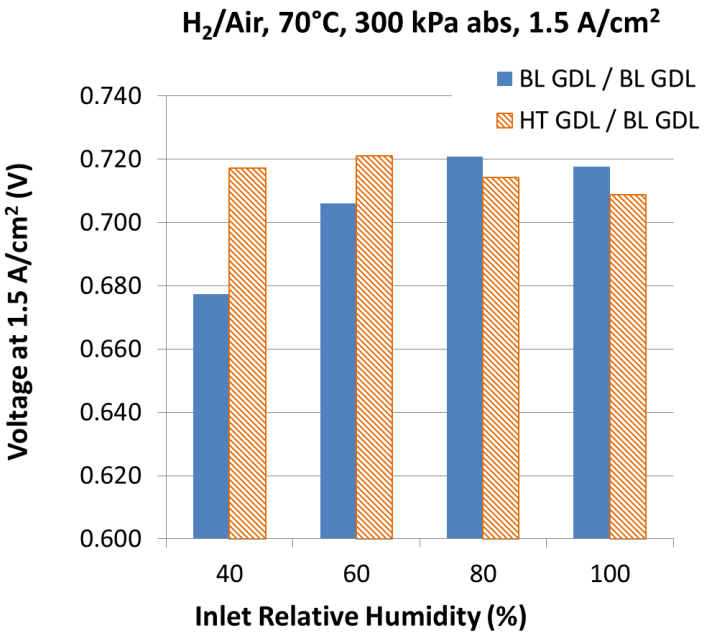

Figure 3.16: Relative humidity sweep at 1.5 A/cm^2 for baseline and asymmetric configurations. HT- High Tortuosity, BL – Baseline (MRC-105) [123].

3.2.2 Passive Anode Water Management with High Tortuosity GDL

The overall water balance between the anode and cathode exits were also compared. Liquid water in the anode and cathode exhaust was condensed at 10°C and collected such that the mass could be recorded. With the water production flux known from the overall current density, the mass balance is reported as the fraction of reaction water that leaves through the cathode exit. The high tortuosity GDL on the anode side configuration in comparison with a baseline MRC-105 symmetric configuration yielded a significant shift in water balance. Several additional test conditions were designed to compare the water balance by varying the anode vs. cathode RH. Shown in Figure 3.17, the high tortuosity material shifts the water balance greater than 30% toward the cathode under most conditions tested. This is a result of the significant increase in diffusion resistance limiting back diffusion toward the anode channel. Under most conditions no reaction water is moving toward the anode and the cathode steam is removing anode water. Although performance varies slightly thereby changing the heat load, the magnitude of the observed water balance shift is much higher than uncertainty associated with these effects.

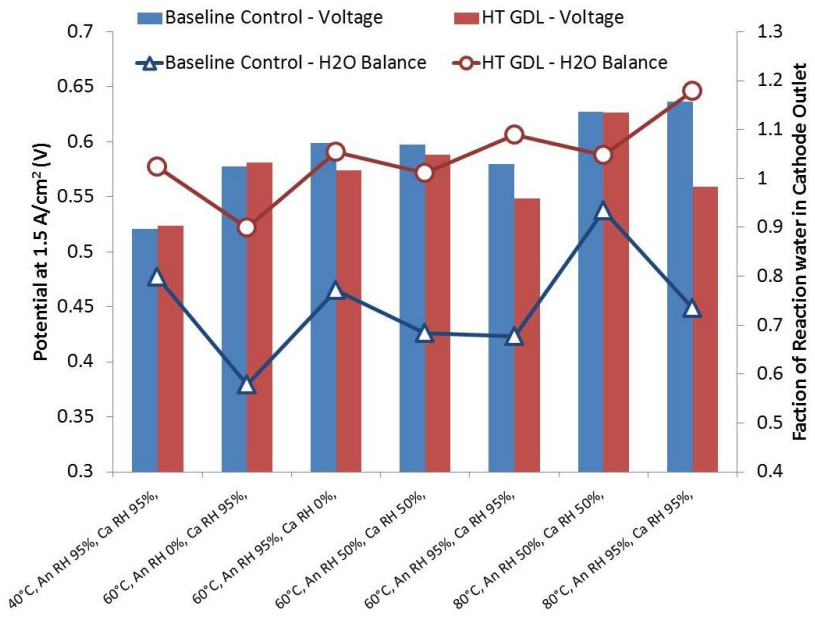

Figure 3.17: Water balance study of high diffusion resistance anode GDL (labeled HT in plot), water balance error is less than ± 3% based on reaction water mass balance and performance variation [123].

The data reported thus far have been generated with pure hydrogen. However, partial PEFC systems typically recirculate the anode fuel and nitrogen cross-over through the membrane will result in a diluted anode feed stream. Shown in Figure 3.18 are wet and dry polarization curves with and without nitrogen dilution of 15% as a function of time to demonstrate the stability during each test point. Although there is a slight performance loss observed (20 mV), these initial results indicate a higher diffusion resistance anode GDL is viable a concept for PEFC systems. Equation 4 predicts 10 mV of this loss is simply due to the change in equilibrium potential with lower hydrogen partial pressure at the anode catalyst. In the context of efficiency however, it must also be considered that this material configuration will reduce nitrogen cross-over, perhaps countering the impact of a voltage loss.

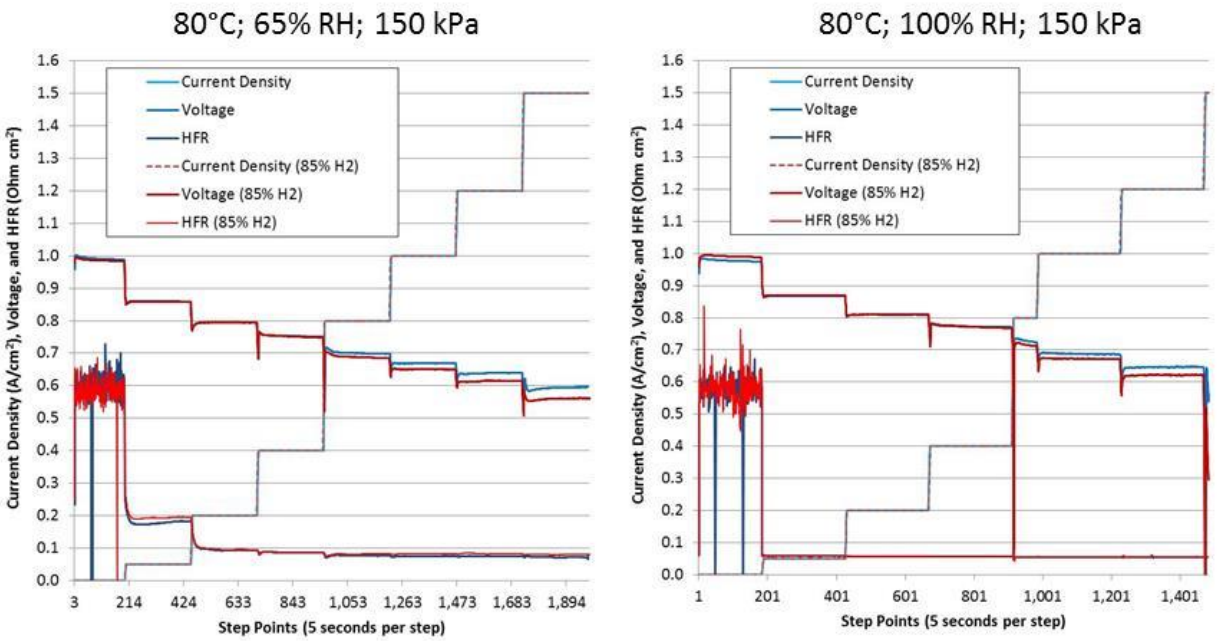

Figure 3.18: Asymmetric high diffusion resistance anode GDL wet performance comparison with and without nitrogen dilution on the anode [123].

3.3 Effective Diffusion Measurements

The experimental results presented thus far have focused on transport in the GDL and liquid water accumulation. To link these data and predict transport for a wide variety of operating conditions a correlation for the effective diffusion coefficient as a function of saturation is required. In this section, the results of the combine experimental methods of limiting current and neutron imaging are used to validate effective medium theory based on the change in porosity hat liquid water imposed.

3.3.1 Oxygen Transport Resistance and Liquid Water

The resistance to oxygen mass transfer in the cathode GDL as a function of the limiting current for each experimental condition is given in Figure 3.19. Both GDL materials show the dry and wet plateaus at similar values as reported by Caulk et al. [29]. Since the Toray material has approximately one-third the thermal resistance of the MRC GDL, the earlier transition in transport resistance is a result of the lower average saturation pressure in the Toray GDL causing more condensation at a given water flux. This is

confirmed in Figure 3.20 by the average liquid water saturation for the two GDLs within the field of view (1.5 cm or 15 channels) where more accumulation occurs at a lower limiting current in the Toray GDL.

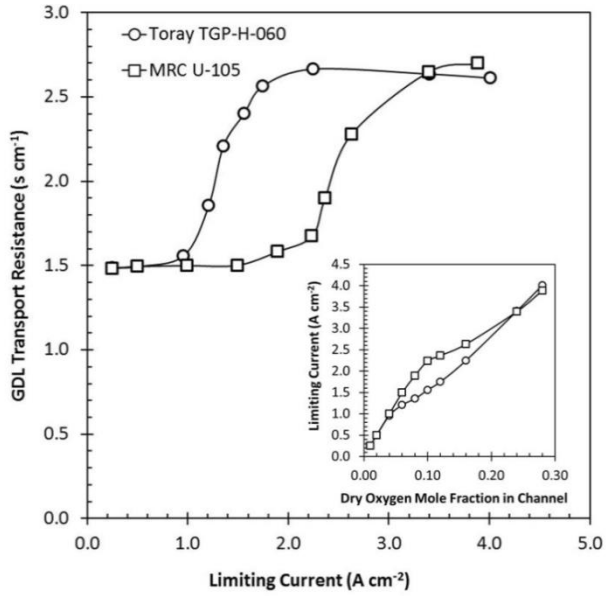

Figure 3.19: Measured GDL oxygen transport resistance for Toray TGP-H-060 and MRC U-105, calculated from limiting current at varied dry oxygen mole fractions (subplot) [124].

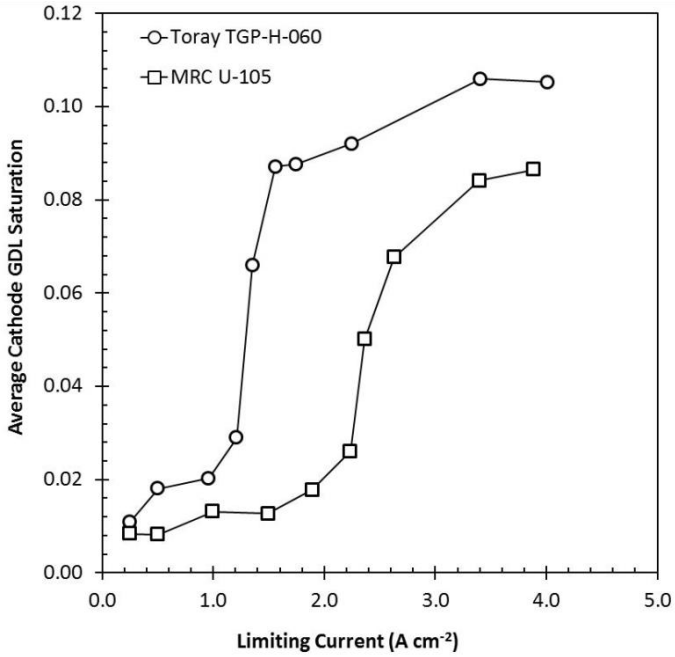

Figure 3.20: Average liquid water saturation in the 1.5 cm viewing area of cathode GDL for each limiting current condition investigated [124].

3.3.2 Determination of Effective Diffusion Relationship with Saturation

A strong correlation between liquid water content and GDL transport resistance is confirmed in Figure 3.19 and Figure 3.20. However, developing an effective oxygen diffusion coefficient relationship based on the average saturation was observed to be insufficient based on the asymmetric nature of water accumulation over the land vs. channel. A typical radiograph given in Figure 3.21 represents a consistent trend observed at all limiting current conditions, as nearly all liquid water accumulation occurs adjacent to the land. This is of course expected, due to the different heat transfer boundary conditions adjacent to the GDL [125]. One other possible contributor to this saturation distribution relevant to the current work is convection through the GDL caused by the high gas flow rates used to achieve differential conditions. This was investigated by reducing the flow rate by a factor of 5; however the resulting distribution and quantity of water was relatively unchanged. This result is also theoretically established based on the measured in-plane pressure differential though these porous substrates being significantly higher than the channel [126]. Therefore, a two dimensional analysis focusing only on diffusion is reasonable, and was adopted to determine the ratio of the bulk to effective diffusion coefficients for oxygen in the cathode GDLs (D/D_{eff}).

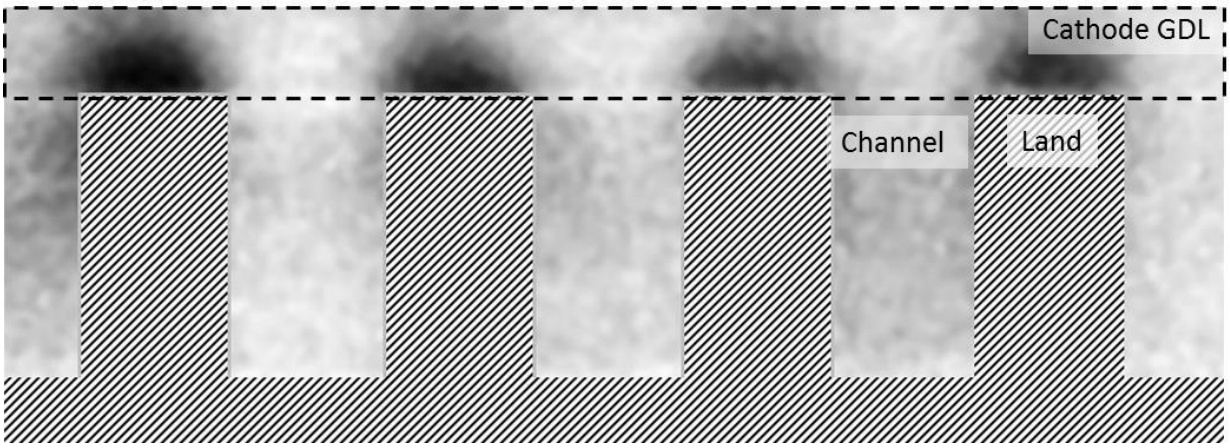

Figure 3.21: Neutron radiograph of MRC U-105 at limiting current with land/channel geometry superimposed, where dark areas represent liquid water (operating condition: 70C, 20% oxygen in nitrogen, 77% RH, 300 kPag, 0.1 V) [124].

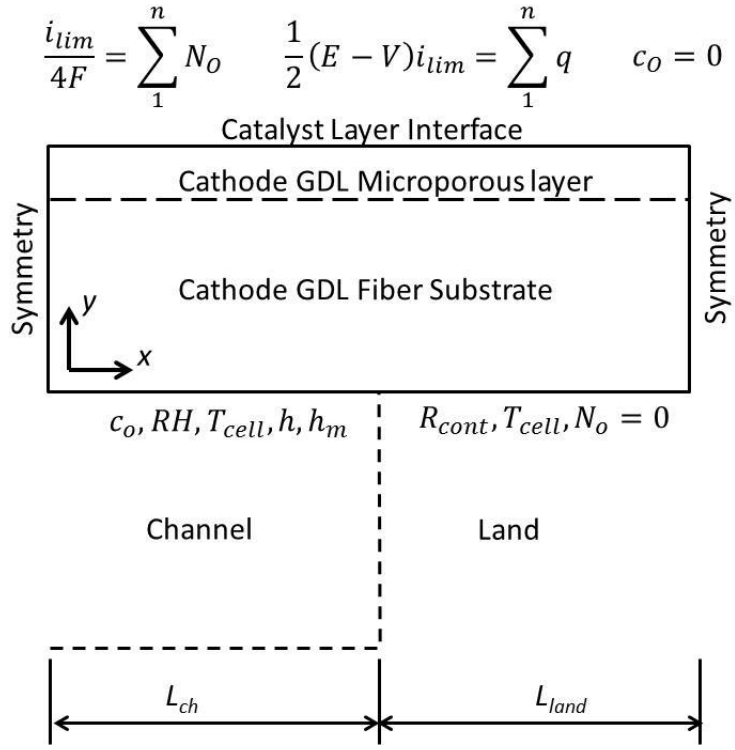

Figure 3.22: Cathode GDL model domain and associated boundaries used in conjunction with measured saturation distribution used to solve for the effective oxygen diffusion coefficient [124].

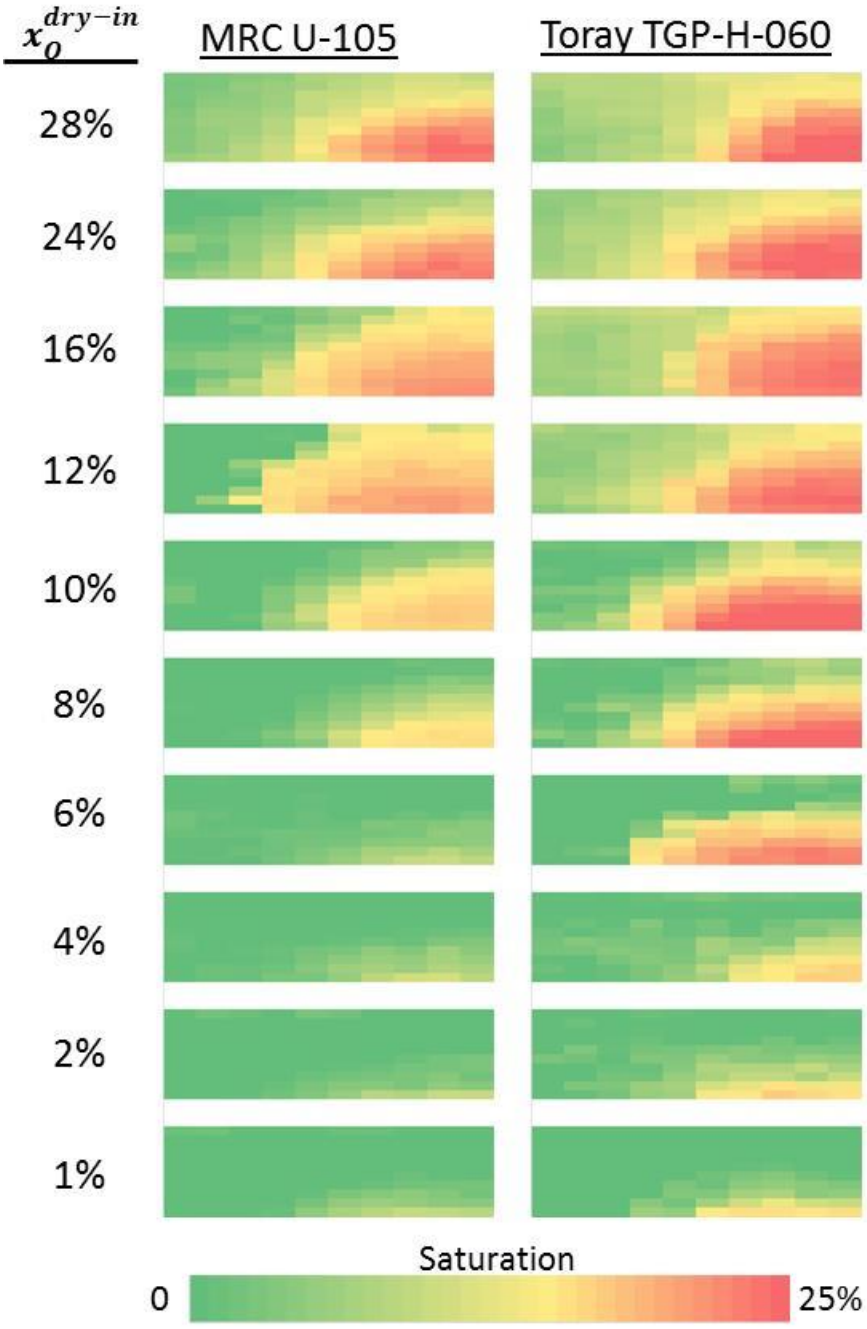

Figure 3.23: Average measured saturation at limiting current for MRC U-105 and Toray TGP-H-060 within the domain described in Figure 3.22 [124].

The two dimensional analysis was developed through the GDL in a half-land and half-channel domain with boundary conditions, as shown in Figure 3.22. The measured saturation used in this analysis is given in Figure 3.23. These saturation maps for each limiting current condition were generated by averaging the local saturation (at each pixel) within the domain (Figure 3.22) across the entire

measurement window of 15 lands and channels. Analysis of species within the GDL was simplified by varying RH linearly from 100% at the saturation interface (based on saturation maps in Figure 3.23) and at the catalyst layer to the channel RH while oxygen and nitrogen were conserved with no consideration for membrane crossover. The heat conduction and mass balance of oxygen at steady state

$$\frac{\partial}{\partial x}\left(k_x \frac{\partial T}{\partial x}\right) + \frac{\partial}{\partial y}\left(k_y \frac{\partial T}{\partial y}\right) = 0 \quad (24)$$

$$\frac{\partial}{\partial x}\left(D_{eff,x} \frac{\partial c_o}{\partial x}\right) + \frac{\partial}{\partial y}\left(D_{eff,y} \frac{\partial c_o}{\partial y}\right) = 0 \quad (25)$$

were solved using finite difference method where the anisotropic thermal conductivity, *k,* and effective diffusivity, $D_{eff,}$ in the through-plane and in-plane dimensions was accounted for [127] [128] [129] [130]. The total heat flux, *q,* at the catalyst layer interface, through the cathode GDL, was assumed to be half of the waste heat as symmetric anode and cathode GDL and flow channel geometries were used and the thin membrane poses only a small thermal resistance

$$q = \frac{1}{2}(E - V)i_{lim} \quad (26)$$

where *E* =1.25 V is the equilibrium potential of the cathode reaction and *V* is the measured cell potential. The total oxygen flux, N_O, at the catalyst layer interface is known from the limiting current per Equation 27.

$$N_O = \frac{i_{lim}}{4F} \quad (27)$$

The dry thermal conductivity of the GDL will represent a maximum temperature differential through the layer, as the addition of saturation will increase the effective thermal conductivity, k_{eff}. Recent experimental work by Xu et al. [18] shows these relationships and is approximated here using the measured saturation map

$$k_{eff} = s\varepsilon k_w + k_{GDL}^{dry} \quad (28)$$

where s is the measured local saturation, ε is the porosity, and k_{GDL}^{dry} is the measured thermal conductivity of the dry GDL. Compressive strain differences between the land and channel were accounted for based on channel intrusion of 20 µm [131].

A unique solution for *n* in the modified Bruggman relationship based on effective medium theory,

$$D_{eff} = D[\varepsilon(1 - s)]^n \quad (29)$$

was found numerically through the solution of Equations 24 and 25 with local current density over the land and channel varying such that the oxygen concentration at the catalyst layer interface was equal to zero while constrained by the overall limiting current density. The specific GDL properties, anisotropic relationships, and associated parameters used in this analysis are given in Table 3 and Table 4.

Table 11: Parameters used in the two-dimensional finite difference model.

Parameter	Value	unit
Cell Temperature, T_{cell}	70	°C
Total Pressure, P	300	kPag
Half Channel Width, L_{ch}	0.250	mm
Half Land Width, L_{land}	0.250	mm
Mass Transfer Coefficient in Channel, h_m Baker et al. [19]	0.056	m s^{-1}
Heat Transfer Coefficient in Channel, h	12	W m^{-2} K^{-1}
In-Plane/Through-Plane GDL Carbon Fiber Diffusivity, D_x/D_y [29]	1.18	-
In-Plane/Through-Plane GDL MPL Diffusivity, D_x/D_y [29]	1.7	-
Thermal Conductivity of Water, k_w	0.665	W m^{-1} K^{-1}
MPL Porosity, ε [132]	50%	-
In-Plane / Through-Plane MPL Thermal Conductivity, k_x/k_y	1.0	-
Gas Pair Diffusivity for Oxygen in Nitrogen, $D_{O\text{-}N}$ [133]	$D_{O-N} = \frac{0.273}{P}\left(\frac{T}{T_{ref}}\right)^{1.823}$	cm^2 s^{-1}
Gas Pair Diffusivity for Oxygen in Water Vapor, $D_{O\text{-}W}$ [133]	$D_{O-W} = \frac{0.3}{P}\left(\frac{T}{T_{ref}}\right)^{1.8}$	cm^2 s^{-1}

Significant temperature and current density variations resulted from the numerical solution at the high limiting currents and low cell potential associated with these experiments. An example of these gradients at the catalyst layer interface is given in Figure 3.24 for 20% oxygen case at limiting current, where the variation observed correlates well with similar studies [134]. This distribution plays a significant role throughout the solution and this is not captured with a more simplified one-dimensional approach. The solution for each limiting current based on its corresponding saturation distribution (Figure 3.23) resulted in relatively consistent values for the exponent n in Equation 29 of 3.6 ± 0.1 for Toray and 4.0 ± 0.1 for MRC. For Toray TGP-H-060, these values are in line with similar studies that reported 3.8 [22] and 3.5 [23]for the through-plane direction. The error reported for the exponent *n* is the range found from the solutions of the 10 operating conditions studied for each material. The

different magnitude of *n* is likely related to variations of water morphology inside pore geometries of the two substrates examined, thus impacting the tortuosity in Equation 11.

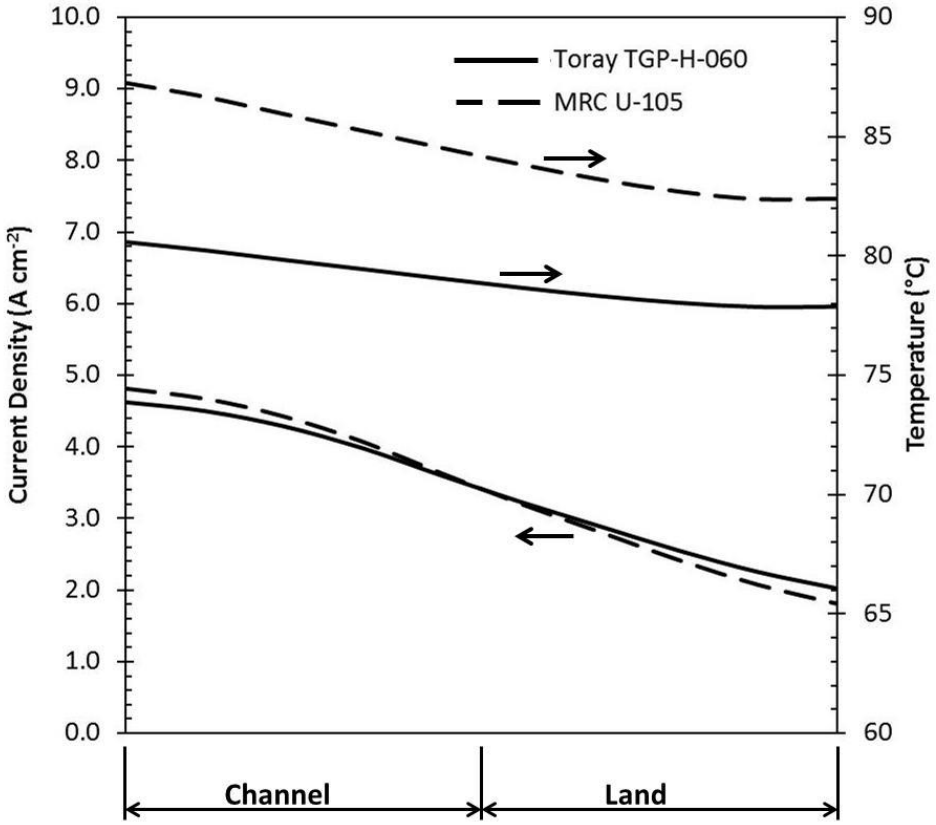

Figure 3.24: Simulation results of current density and temperature at the catalyst layer interface for 20% oxygen limiting current condition [124].

The effective diffusion correlation developed based on local saturation and corresponding boundary conditions (modified Bruggeman, Equation 29) is of particular interest because although the limiting current analysis of diffusion resistance is qualitatively accurate, it can't be applied to a fuel cell model without linkage to saturation. Thus far, this functionality has been established based on the two-dimensional solution presented. However, its applicability for a one-dimensional model where average saturation between the land and channel is used should be considered as this is thought to be a critical issue for adding two-phase capability to the well-established one-dimensional dry model. Figure 8 shows this comparison of the measured diffusion resistance at limiting current (Equations 12-15) to that calculated with Equation 29 using average saturation from the data in Figure 3.23. When the GDL is nearly dry the modified Bruggeman relationship is accurate. However, Figure 3.25 also demonstrates that using average saturation will underpredict the diffusion resistance when significant liquid water is

non-uniformly distributed across the in-plane dimension of the GDL. This is caused by the nonlinear impact of saturation on the effective diffusion coefficient.

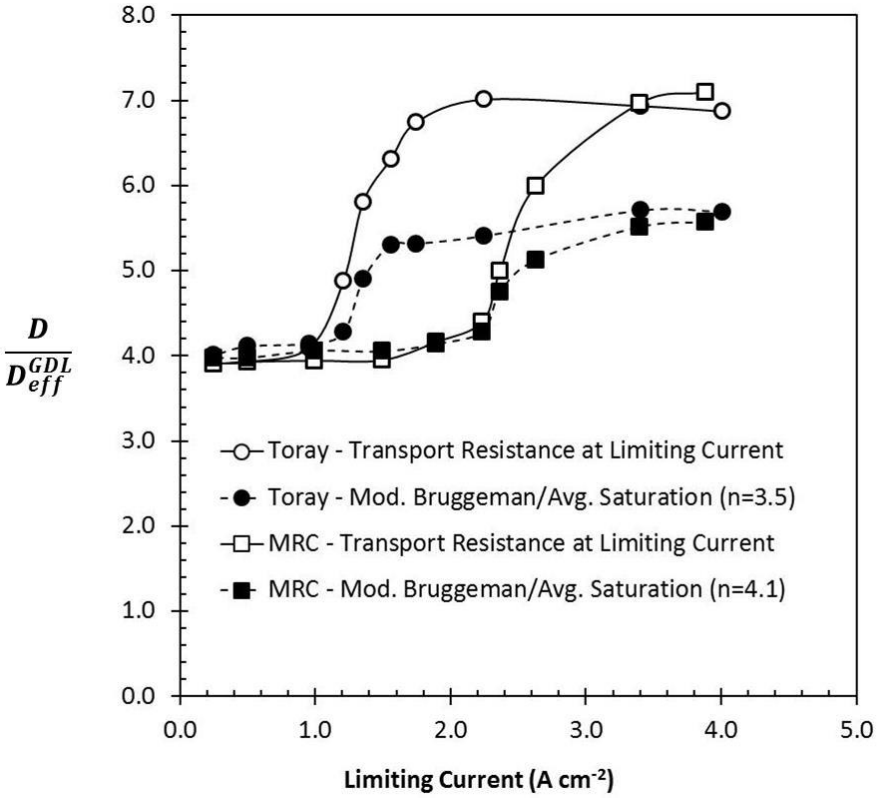

Figure 3.25: Effective diffusion coefficients through the GDL calculated based on limiting current (Equation 14) and the modified Bruggeman relationship (Equation 28) based on average GDL saturation [124].

The use of the Bruggeman relationship with saturation will always under predict the diffusion resistance, as it implicitly assumes a connected pathway for gas transport exists until the medium is fully saturated, while the true situation can include blockage of a pore pathway via a much lower saturation [6]. Thus, the Bruggeman relationship should be viewed as a limiting case in the context of effective diffusion resistance with saturation. As a result of the dramatic channel/land variation in thermal and mass transport boundary conditions, a simplified 1-D fuel cell model must consider the land vs. channel liquid water distribution in the GDL. Such a correction could be derived empirically from the data herein, but its usefulness would be limited as these limiting current conditions represent a most extreme case where temperature gradients will be highest, thus causing the most pronounced maldistribution of liquid water over the land vs. channel.

4. Chapter 4 – Oxygen Transport Near the Pt Surface

This research was focused on transport resistance through the thin ionomer at the Pt catalyst interface (Goal 3 in Section 1.4). Two experimental tracks were pursued, one comparing ionomer surface area to Pt (Section 2.1.3), and the second where the impact of ionomer thickness (Section 2.1.4) was evaluated. Novel experimental designs have been developed to isolate and study these parameters. Custom catalyst layer formulations and fabrication methods were used to make well controlled samples and limiting current experiments provide a direct measurement of the pressure independent component of transport resistance. Results were used to model transport through the ionomer at a single Pt nano-particle with the ultimate goal of characterizing the contribution of bulk vs. interfacial transport resistance in the layer.

4.1 Platinum Loading and Catalyst Layer Structure

The experiments described in this section targeted consideration of the relative influences of parameters related to local transport at the Pt nano particle, where samples were designed such that mesoscale and agglomeration effects were consistent across all configurations. To interpret the experimental results, limiting current at an individual Pt particle based on oxygen transport through the ionomer was modeled to consider the role of interfacial resistances.

4.1.1 Electrochemical Characterization of Samples

The key electrochemical characterization results for all dispersion samples (described in Section 2.4.2) are provided in Figure 4.1. Ideally, the measurements in Figure 4.1a-e would be constant as this would avoid convolving the focus of this study, transport loss near the Pt surface. Of these measurements, the variation in Pt area measured from HAD cyclic voltammetry is most significant. This variation of nearly 30% results from differences in the mean Pt particle size which was measured with x-ray diffraction (XRD) for the catalysts used in this study. HAD areas calculated based on the mean Pt diameter from XRD (4.9 nm) verify the measurement within 5%, and the trend in Pt area was independently verified in Figure 4.1b where the mass activity follows a similar but less pronounced trend. In addition to characterization of the platinized carbon aggregate distribution in the cross-section of diluted electrodes with SEM, the Pt particle size distributions for each catalyst type were also characterized with

transmission electron microscopy (TEM). TEM results indicate that lower HAD areas are influenced by infrequent localized large Pt aggregates that have a significant impact on the mean. At 2.0 A cm^{-2}, using a Tafel slope of 140 mV $decade^{-1}$ [86], this variation in Pt area/activity would account for less than ± 10 mV performance difference between all samples at a given loading, assuming no local resistance.

For the MEAs used in this work, high frequency resistance (HFR) was obtained at 8 kHz, and cathode catalyst layer (11 ± 1.5 μm thick cathode regardless of Pt loading and/or dilution, see Table 6) proton transfer resistances were relatively constant at 0.048 ± 0.003 and 0.014 ± 0.004 ohm cm^2, respectively, at the conditions used for fully humidified polarization measurements at 80°C. At these conditions, the losses from electrode proton transfer are less than 14 ± 4 mV [13] at the highest current densities (2.0 A cm^{-2}); thus non-polarizing membrane and contact resistances (HFR) dominate the ohmic corrections applied to the cell potential. Since electrode proton resistance is relatively consistent between samples at 122% RH (Figure 4.1d), a drier condition at 50% RH is given in Figure 4.1c to highlight the relative differences between samples and estimate the performance impact (± 10 mV) at the dry operating condition discussed later in this document.

The oxygen diffusion resistance in the bulk of the porous diffusion media is represented by the ratio of oxygen diffusion coefficients without and with porosity and tortuosity effects (D/D_{eff}) in Figure 4.1e, which was calculated from limiting current at different total pressures [19]. Since the same GDL and macroporous catalyst layer structure was used in all experiments, this parameter should not vary significantly between configurations. This is the case in Figure 4.1e as all data lie within uncertainty, thus verifying that bulk diffusion is relatively constant. When corrected for, this variation in diffusion resistance has a maximum voltage correction variance of ± 5 mV [7]. Summing these variations for bulk diffusion, electrode proton resistance, and Pt surface area results in an error of ± 20 mV at 2.0 A cm^{-2} at fully humidified conditions and up to ± 27 mV at 50% RH. This maximum error between samples is considered when comparing uncorrected performance data.

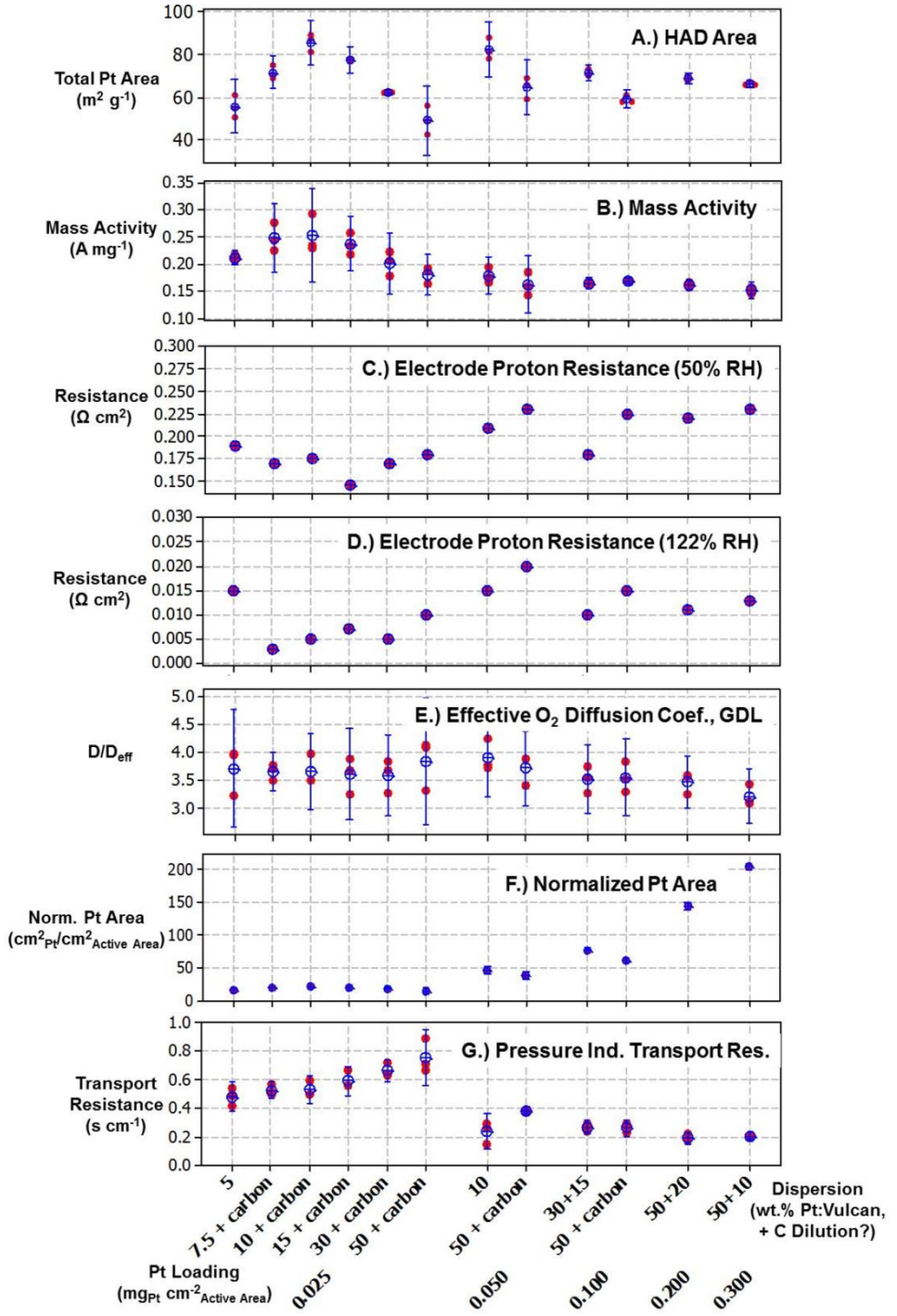

Figure 4.1: Summary of key measurements characterizing all electrode types a.) Pt surface area measured with hydrogen/liquid water cyclic voltammetry [104], b.) Pt mass activity measured at 0.9V in pure oxygen at 80°C and 100% RH [105], c.) electrode proton resistance measured with impedance (50% RH condition shown) [106], d.) electrode proton resistance measured with impedance (122% RH condition shown) [106], e.) effective oxygen diffusion coefficient measured based on pressure dependence of limiting current at <100% RH conditions [19], f.) Pt area normalized to the geometric active area (loading * HAD area), g.) pressure independent transport resistance from limiting current at <100% RH conditions. Error bar represent 95% confidence intervals for the mean [135].

The functionality of pressure independent transport resistance given in Figure 4.1g with the normalized Pt area (*loading × HAD area* = $A_{Pt,\,surf}/A_{active\ area}$) given in Figure 4.1f is the focus of the current study. Based on the limiting current analysis, the pressure independent oxygen transport resistance ($R_{O_2}^{P,ind.}$) is assumed to consist of Knudsen ($R_{O_2}^{Knudsen}$) and interfacial effects. Since an interfacial resistance would occur at or near the Pt surface, this component of resistance ($R_{O_2}^{Pt/i}$) is assumed to scale inversely with the normalized Pt area per Equation 16. This assumption is good when the local resistance is high enough to result in relatively uniform reaction current distribution [33]. Based on Equation 16, $R_{O_2}^{Knudsen}$ is determined from the intercept of the $R_{O_2}^{P,ind.}$ vs. $A_{active\ area}/A_{Pt,\,surf}$ relationship that is generated experimentally by varying Pt loading. The total transport resistance ($R_{O_2}^{total}$) also includes the pressure dependent bulk diffusion resistance (characterized in Figure 4.1e) that is given in Equation 13.

4.1.2 Performance and Limiting Current Results

The total transport resistance at limiting current (i_{lim}) is given by Equation 12 when the oxygen concentration at the Pt surface is near zero. To gather multiple data points at low limiting current, oxygen concentrations of 0.01, 0.02, and 0.04 are considered at total pressures of 110, 150, 200, and 300 kPa (to evaluate the pressure dependent terms). Liquid water effects were minimized with differential flow controlled at 65% relative humidity.

Before further considering these limiting current results, Pt surface area was examined with polarization performance of the non-diluted electrode formulations (i.e. no additional bare carbon support). The pure uncorrected oxygen performance in Figure 4.2a was corrected for HFR, electrode protonic resistance, and hydrogen crossover current in Figure 4.2b. Normalizing current density by Pt area on a logarithmic scale shows a relatively linear behavior, thus indicating most of the performance loss associated with reduced loading in Figure 4.2a is kinetic. However, for the same operating condition with air instead of oxygen (the analysis now including bulk transport corrections as oxygen concentration can vary significantly in air), performance shown in Figure 4.3 indicates an increasing transport loss as loading is decreased. In Figure 4.3b, the only transport loss not accounted for is the pressure independent term given in Figure 4.1f, which clearly varies as loading decreases. With this local transport loss now shown to increase with decreased Pt loading, a simple geometric correction is sought as a first approximation.

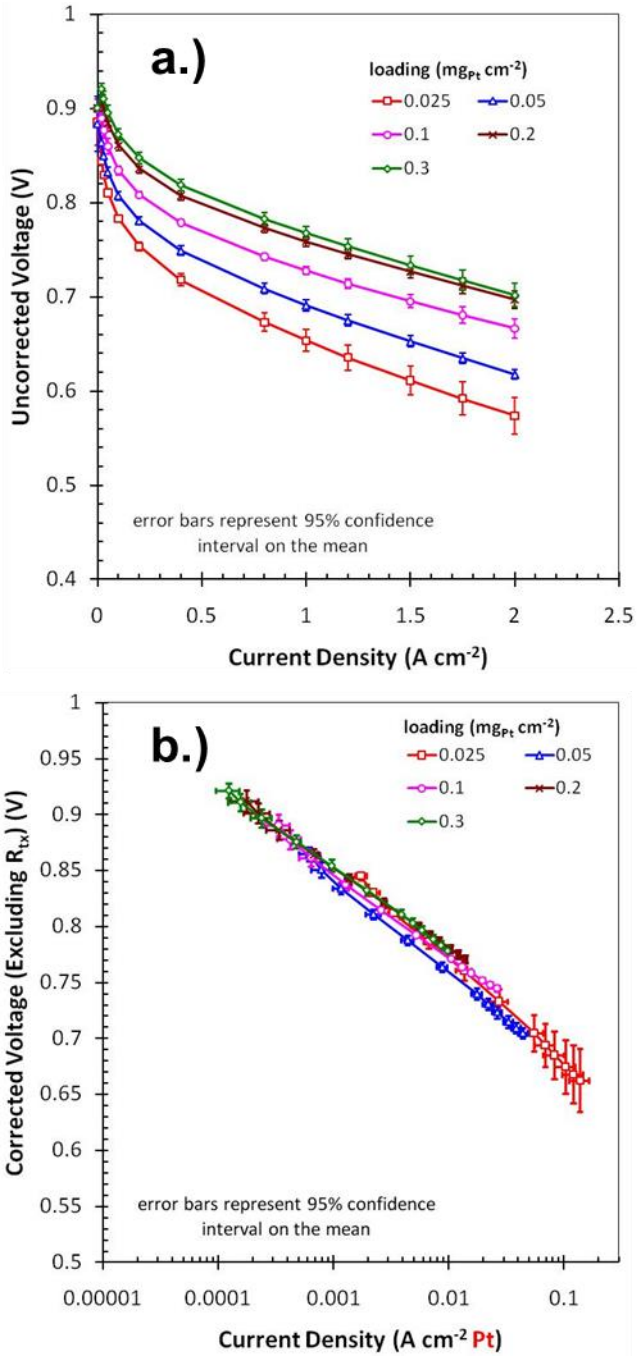

Figure 4.2: Non-diluted electrode performance with 100% H2/O2, 100% RH, 80C, 150 kPa operating conditions. a.) uncorrected performance; b.) corrected potential with current density scaled to Pt area [135].

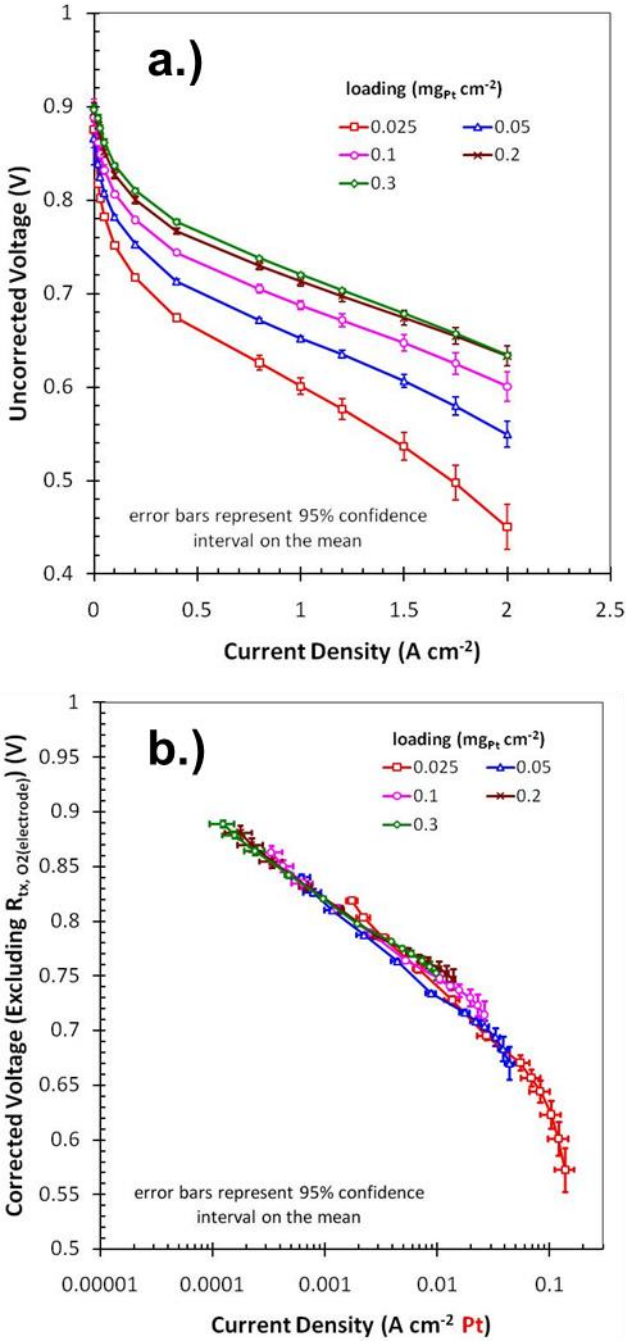

Figure 4.3: Non-diluted electrode performance with H2/air, 100% RH, 80°C, 150 kPa operating conditions. a.) uncorrected performance; b.) corrected potential with current density scaled to Pt area [135].

As assumed in Equation 16, a logical starting point is to scale based on the inverse of normalized Pt area. Since all bulk transport resistance has been shown to be relatively constant, the total transport resistance calculated from Equation 12 for each oxygen concentration at a given total pressure is considered as a function of loading according to Equations 13 and 16 in Figure 4.4. In Figure 4.4, the

slope for a given total pressure represents the transport resistance near the Pt surface. This linear approximation fits the data fairly well, resulting in an average resistance of 4.8 s cm^{-1} at the Pt surface.

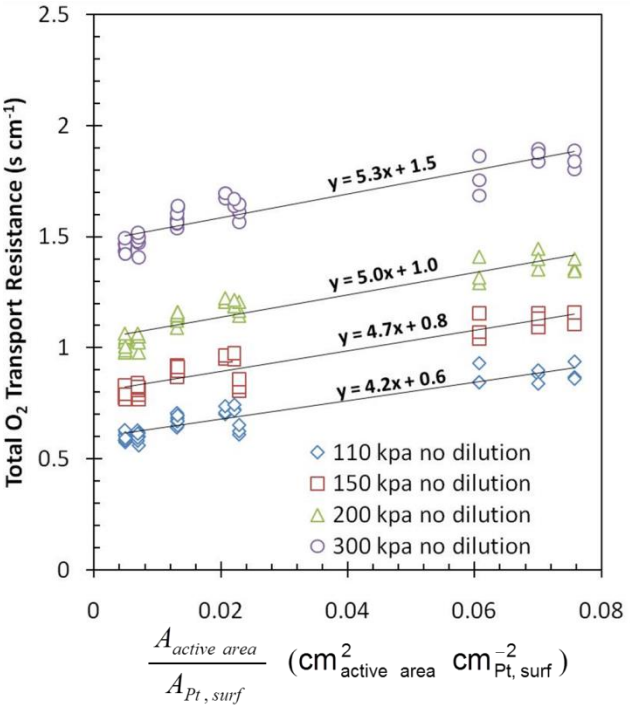

Figure 4.4: Total transport resistance calculated from Equation 12 for each oxygen concentration at a given total pressure as a function of Pt area for non-diluted catalyst layers [135].

Next, to further consider if this resistance scales exclusively with Pt area, the performance of the carbon diluted electrodes is compared to the non-diluted samples. In oxygen, this comparison shown in Figure 4.5a indicates nearly identical performance, with kinetic loss dominating. However, in air, for a given loading, a significant deviation between diluted and non-diluted samples is observed in Figure 4.5b-c. Figure 4.5b provides a direct comparison to Figure 4.3, where all diluted electrodes at a given Pt loading show increased mass transport loss. A drier operating condition at 65% RH is given in Figure 4.5c, and the deviation between high and low wt.% of Pt/C catalyst layers is observed to increase at these drier test points. This trend indicates that liquid water does not have a significant role in the observed performance loss between catalyst types at a given loading. Increased deviation at dry conditions was also confirmed with the 93.5°C polarization curve (not shown) described in Table 1.

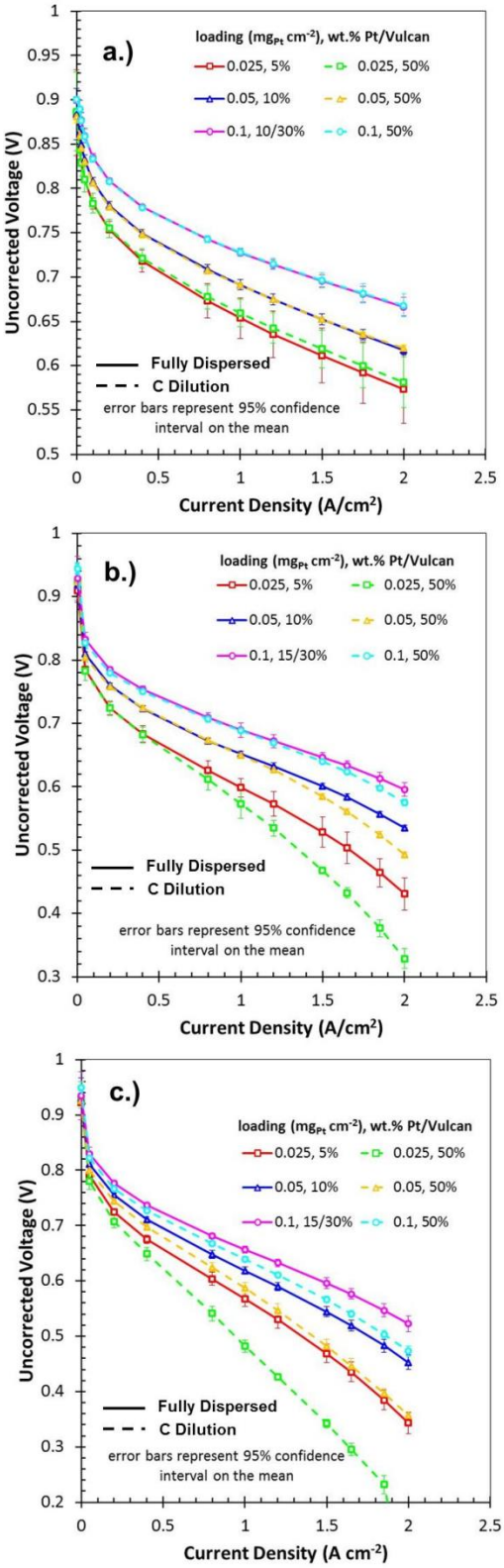

Figure 4.5: Diluted compared with non-diluted performance; a.) H2/O2, 100% RH, 80°C, 150 kPa operating conditions b.) H2/air, 100% RH, 80°C, 150 kPa operating conditions (non-diliuted data from Figure 5), c.) H2/air, 65% RH, 80°C, 150 kPa operating conditions [135].

Additional characterization of the deviation between different catalyst dispersions in Figure 4.5 was executed at the lowest loading studied, where the performance deviation between catalyst types is most pronounced. The Pt dispersions at 0.025 mgPt cm^{-2} were further varied with different wt.% Pt/Vulcan and bare Vulcan content as described in Table 6 (samples 7-12). These formulations expand on the 0.025 mgPt cm^{-2} performance given in Figure 4.5b by further demonstrating a direct correlation between performance loss and Pt dispersion with multiple data sets as shown in Figure 4.6 for the same operating condition. Here, performance loss seems to scale proportionally with increasing wt.% Pt/Vulcan catalyst when current is normalized by geometric area in Figure 4.6a. In Figure 4.6b, current density is corrected for the measured gas crossover and scaled to Pt area with potential corrected for coverage dependent kinetics [87], ohmic resistance, and changes in oxygen partial pressure in the electrode due to bulk and Knudsen transport resistances. Although the high wt.% dispersions seem to scale with Pt area in Figure 4.6b, the more dispersed 5 and 7.5 wt.% Pt/C samples clearly do not. This indicates that scaling directly to Pt surface area is not sufficient for all dispersed catalyst structures tested. Rather, at low loading, the dispersion (or equivalently the distance between Pt particles) should be considered.

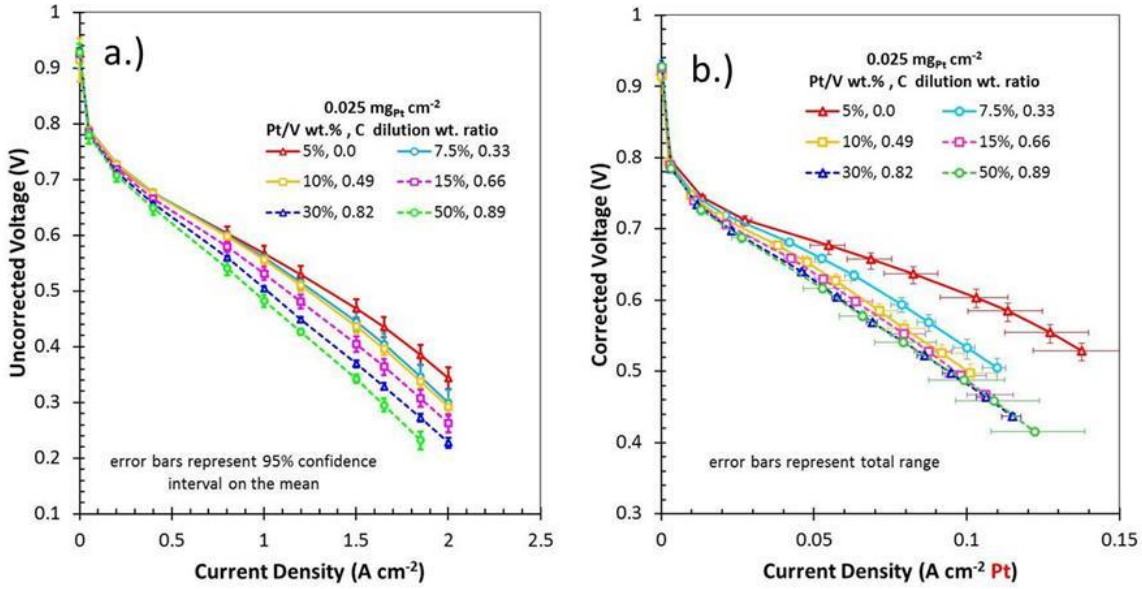

Figure 4.6: Loadings of 0.025 mgPt cm^{-2} with varied bare carbon dilution (samples 7-12 in Table 6) at H_2/air, 65% RH, 80°C, 150 kPa operating conditions, a.) uncorrected performance, b.) current density corrected for measured gas crossover and scaled to Pt area with potential corrected for coverage dependent kinetics, ohmic resistance, and changes in oxygen partial pressure in the electrode due to bulk and Knudsen transport resistance [135].

4.1.3 Limiting Current at a Single Pt Particle Model

To investigate the influence of dispersion, one can solve the oxygen diffusion equation for total oxygen transport resistance from the gas phase to the Pt surface, considering interfacial resistance at Pt/ionomer ($R_{Pt/i}$) and gas/ionomer interfaces ($R_{g/i}$), respectively, in addition to the bulk resistance of the ionomer film (R_f). In the platinized aggregates shown in Figure 2.2, multiple platinum nano-particles sit on a carbon support particle coated with electrolyte. For oxygen transport through the thin ionomer film to the Pt surface where it is electrochemically reduced to water, we assume that the Pt particles are uniformly distributed on the surface of a carbon particle and thus only consider the case that a single Pt particle rests on a discrete carbon surface whereas the thin ionomer film of uniform thickness covers both Pt and carbon surfaces. Approximately, it can be represented in the cylindrical coordinates as displayed in Figure 4.7.

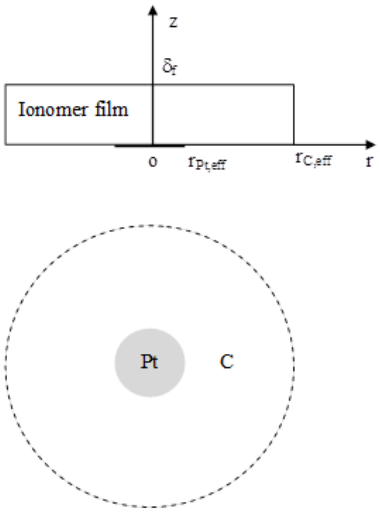

Figure 4.7: Schematic of the model representation of a single Pt particle on carbon support surface covered by a thin ionomer film [135].

Given the weight percentage of Pt, Pt particle size, and carbon support particle size, one can calculate the number of Pt particles on the surface of the carbon particle,

$$N_{Pt} = \frac{\rho_C}{\rho_{Pt}} \cdot \left(\frac{r_C}{r_{Pt}} \right)^3 \cdot \left(\frac{wt\%Pt}{100 - wt\%Pt} \right) \quad , \qquad (30)$$

where ρ is the density, r the radius, with subscripts C and Pt denote carbon and Pt particles, respectively. The effective radii shown in Figure 4.7 results from the surface area of the Pt particle,

$$r_{Pt,eff} = 2r_{Pt} \quad . \tag{31}$$

And from the surface area of the carbon particle and the number of Pt particles,

$$r_{C,eff} = \frac{2r_C}{\sqrt{N_{Pt}}} \quad . \tag{32}$$

The Pt particle size can be estimated based on the measured HAD area. Assuming spherical particle,

$$r_{Pt} = \frac{3}{\rho_{Pt} \cdot HAD} \quad . \tag{33}$$

Conservation of oxygen in the ionomer film gives

$$\frac{1}{r}\frac{\partial}{\partial r}\left(K_{O2} r \frac{\partial p_{O2}}{\partial r}\right) + \frac{\partial}{\partial z}\left(K_{O2}\frac{\partial p_{O2}}{\partial z}\right) = 0 \quad , \tag{34}$$

where K_{O2} is the oxygen permeability in the ionomer film. Equation 34 can be reduced to 1-D by integrating it over ionomer film thickness δ_f,

$$\frac{\partial}{\partial r}\left(K_{O2} r \frac{\partial p_{O2}}{\partial r}\right) + \left[\left(K_{O2}\frac{\partial p_{O2}}{\partial z}\right)_{z=\delta_f} - \left(K_{O2}\frac{\partial p_{O2}}{\partial z}\right)_{z=0}\right]\frac{r}{\delta_f} = 0 \quad . \tag{35}$$

When measuring limiting current, oxygen partial pressure at the Pt surface approaches zero. Thus, one has

$$\left(K_{O2}\frac{\partial p_{O2}}{\partial z}\right)_{z=\delta_f} = \frac{p_{O2}^g - p_{O2}}{R_{g/i} + \frac{\delta_f}{2K_{O2}}} \quad , \tag{36}$$

and

$$\left(K_{O2}\frac{\partial p_{O2}}{\partial z}\right)_{z=0} = \begin{cases} 0, & \text{if } r > r_{Pt,eff} \\ \dfrac{p_{O2}}{R_{Pt/i} + \dfrac{\delta_f}{2K_{O2}}} & \text{if } r \le r_{Pt,eff} \end{cases} \quad . \tag{37}$$

Notice that in equations 36 and 37, interfacial resistance at both gas/ionomer and Pt/ionomer interfaces are considered. Utilizing equations 36 and 37 as well as the symmetric boundary condition at r = 0 and

$r = r_{Pt,eff}$, Eq. 35 can be integtated over a control volume of Δr and then solved numerically to obtain oxygen pressure within each control volume of the ionomer film

$$p_{O2,i} = \frac{\frac{2r_{i-1}}{\Delta r_i + \Delta r_{i-1}} p_{O2,i-1} + \frac{2r_i}{\Delta r_i + \Delta r_{i+1}} p_{O2,i+1} + \frac{p_{O2}^g}{(2\beta_g + 1)} \cdot \frac{r_i^2 - r_{i-1}^2}{\delta_f^2}}{\frac{2r_{i-1}}{\Delta r_i + \Delta r_{i-1}} + \frac{2r_i}{\Delta r_i + \Delta r_{i+1}} + \left(\frac{1}{2\beta_g + 1} + \frac{\alpha}{2\beta_{Pt} + 1} \right) \frac{r_i^2 - r_{i-1}^2}{\delta_f^2}} \quad . \qquad (38)$$

For internal control volumes, and

$$p_{O2,i} = \frac{\frac{2r_i}{\Delta r_i + \Delta r_{i+1}} p_{O2,i+1} + \frac{p_{O2}^g}{(2\beta_g + 1)} \cdot \frac{r_i^2}{\delta_f^2}}{\frac{2r_i}{\Delta r_i + \Delta r_{i+1}} + \left(\frac{1}{2\beta_g + 1} + \frac{1}{2\beta_{Pt} + 1} \right) \frac{r_i^2 - r_{i-1}^2}{\delta_f^2}} \quad , \qquad (39)$$

for left-bound control volume (adjacent to r=0), and

$$p_{O2,i} = \frac{\frac{2r_{i-1}}{\Delta r_i + \Delta r_{i-1}} p_{O2,i-1} + \frac{p_{O2}^g}{(2\beta_g + 1)} \cdot \frac{r_i^2 - r_{i-1}^2}{\delta_f^2}}{\frac{2r_{i-1}}{\Delta r_i + \Delta r_{i-1}} + \left(\frac{1}{2\beta_g + 1} \right) \frac{r_i^2 - r_{i-1}^2}{\delta_f^2}} \quad , \qquad (40)$$

for the right-bound control volume (adjacent to $r = r_{C,eff}$). In Eq. 38, α takes 1 for the control volumes above Pt surface and 0 for that touching carbon surface. In Eq. 38 through 40, β is the ratio of interfacial resistance over the bulk resistance of the ionomer film, which is

$$\beta_k = \frac{R_{k/i}}{\left(\frac{\delta_f}{K_{O2}} \right)} \qquad \mathrm{k = g,\ Pt} \quad . \qquad (41)$$

Eq. 38 through 38 were iteratively solved for oxygen pressure distribution in the thin ionomer film. Then the limiting current density in the unit of A cm^{-2}_{Pt} can be calculated by the total oxygen flux to the Pt surface

$$i_{\lim} = \frac{4F}{r_{Pt,eff}^2} \sum \frac{p_{O2,i}(r_i^2 - r_{i-1}^2)}{\left(R_{Pt/i} + \frac{\delta_f}{2K_{O2}} \right)} \quad . \tag{42}$$

And the local oxygen transport resistance in the unit of s cm^{-1} can be evaluated by

$$R_{O2}^{local} = \frac{4Fp_{O2}^{g}}{i_{\lim}(RT \cdot 10^3)} \quad . \tag{43}$$

In the case that only one control volume is considered over the Pt surface, the local resistance becomes

$$R_{O2}^{local} = \left[\left(\beta_{Pt} + \frac{1}{2} \right) + \left(\beta_g + \frac{1}{2} \right) \left(\frac{r_{Pt,eff}}{r_{C,eff}} \right)^2 \right] \frac{\delta_f}{K_{O2}(RT \cdot 10^3)} \quad , \tag{44}$$

which shows that the local resistance increases with the relative Pt surface area over carbon surface area. As a result, an electrode made of higher weight percentage of Pt/C would yield higher local transport resistance, as its relative Pt surface area is larger. The relative importance of an interfacial resistance can be extracted from the measured electrode resistance by the limiting current method.

4.1.4 Interfacial Transport Resistance in the Ionomer Layer

Using this single particle analysis based on an assumed constant particle size for all catalysts used in the current study, Figure 4.8 displays a parametrical study for various scenarios of bulk and interfacial resistances in the ionomer film. For comparison, the bulk and interfacial resistances were varied to match the measured local resistance value for the 5 wt.% Pt/Vulcan (most dispersed) electrode first to compare the relative trends, and then the functionality of four film resistance scenarios was evaluated as the ratio of ionomer to Pt area approaches unity. It is shown that a resistance scenario focused on only one of the two interfaces will not agree with the measured local resistance that increases with the Pt particle density. If the interfacial resistances are ignored entirely, the film resistance must be an order of magnitude larger than bulk ionomer. Although the functionality of an increased bulk resistance scenario follows the trend observed experimentally in Figure 4.1g, the magnitude of increase from high to low dispersions of Pt will be under predicted. A final scenario that includes both interfacial resistances at a factor of 4 relative to bulk ionomer resistance (ca. 1 s cm^{-1}) and a film resistance equal to bulk ionomer shows a trend that most closely matches the data. This final scenario also makes the most sense physically, as it has been established that the resistance scales relatively well with Pt surface area

(Figure 4.4) for higher dispersions at a given loading and it should be expected that a transport model would include a Pt interfacial resistance. Furthermore, the oxygen permeability through the bulk of the film remains at a realistic value with this scenario that includes two interfacial resistances.

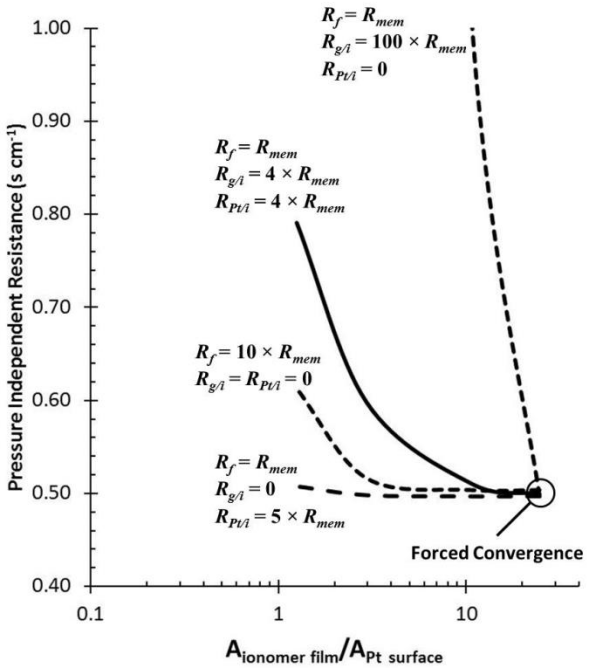

Figure 4.8: Model predictions showing the significance of interfacial resistances at both gas/ionomer and platinum/ionomer interfaces. The model assumes 40 nm (in diameter) carbon particle, 60 m^2/g_{Pt} HAD area, and 4 nm thick ionomer film [135].

A direct comparison of this model to the experimental results requires an average Pt particle size for each catalyst type. This is calculated from the measured electrochemical surface area given in Figure 4.1a and verified with XRD. In Figure 4.9a, the measured pressure independent transport resistance is compared to the model at different loadings with samples that have the highest dispersions of Pt (no bare carbon dilution). In the two model predictions shown, the Pt interfacial resistance is constant at 4 multiples of bulk and the gas side interfacial resistance is varied between 0 and 4 multiples of bulk. This comparison demonstrates that the model accurately captures the trend in the data as Pt loading is decreased without an interfacial resistance at the gas interface. This is due to the high area ratio of ionomer to Pt in these non-diluted samples at lower loadings. At high loading the Pt surface area is large enough to make the local transport effect negligible because of lower current per Pt area. The importance of the gas side interfacial resistance is only realized as the Pt particles get closer together and the oxygen flux through the ionomer/gas surface is near that at the Pt. This relationship is shown in

Figure 4.9b at 0.025 mg_{Pt} cm^{-2} where both resistances are required to predict the increase in transport resistance as the Pt becomes more concentrated.

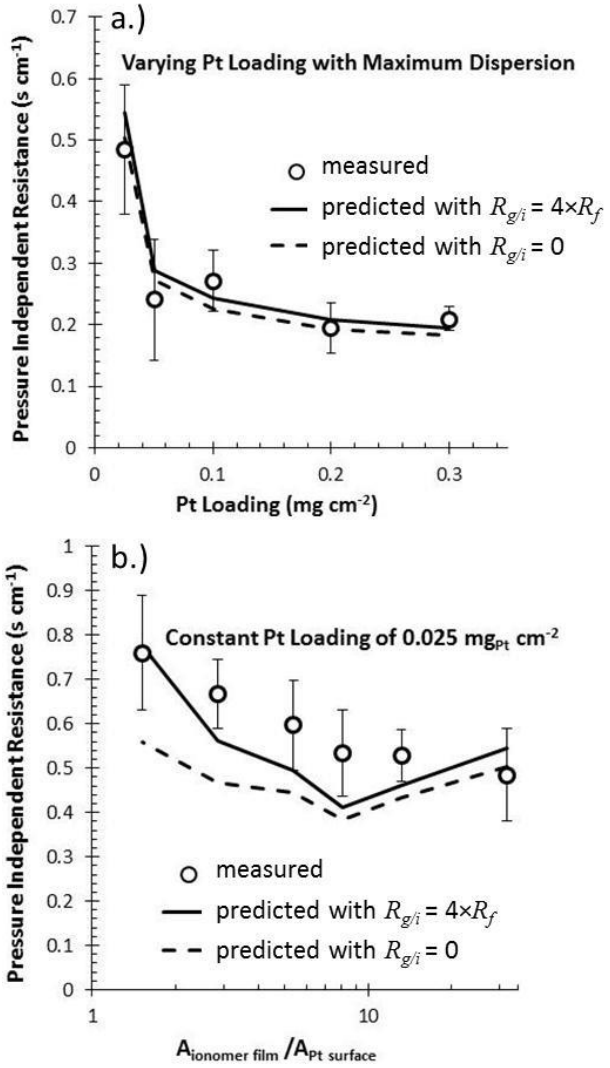

Figure 4.9: Pressure independent oxygen transport resistance from single particle model and experiments, a.) varying Pt loading with most dispersed samples (no bare carbon dilution), b.) constant Pt loading of 0.025 mg_{Pt} cm^{-2} with varying Pt dispersions [135].

This analysis shows that interfacial resistances might dominate the oxygen transport through a thin ionomer film (e.g. 4 nm) to the Pt surface. It is therefore desirable in the current state-of-the-art to reduce oxygen flux per unit area of ionomer coverage. Beyond the simplified analysis presented here, the observed differences in oxygen transport could also be accounted for with a more complex analysis of the mesoscale structure inside agglomerated platinized aggregates where the average transport length to the Pt surface varies. However, given the microscopy characterization results from this work

and key parameters that were kept constant between samples, an agglomerate approach is difficult to justify. Regardless of the complexity of the geometry assumed, these applied experiments along with an oxygen limiting current analysis demonstrate that local oxygen transport loss can be partially mitigated with electrode design, where oxygen flux through the gas/ionomer interface to the Pt surface is minimized for a given electrode structure and catalyst type.

4.2 Ionomer Layer Thickness

As discussed in Section 4.1, with all voltage loss accounted for, the performance of low loaded electrodes is hindered by an additional transport loss at or near the Pt surface. This study was continued using one catalyst type in low-loaded and nominal loaded cathode electrodes, where performance as a function of ionomer film thickness was considered by varying the ionomer-to-carbon weight ratio (I/C) in the composite electrode. This ratio, historically studied in order to optimize performance at various operating conditions, especially low relative humidity, has not been thoroughly investigated as a possible contributor to gas transport resistance. A novel fabrication method was utilized in order to ensure uniformity at low coverage levels, and various diagnostic methods were employed in order to resolve the contribution of the above mentioned voltage loss terms.

4.2.1 Electrochemical Characterization of Electrodes with Varying Ionomer Thickness

Calculated Pt area values, specific activities (O_2 pol curve, current at 0.9 V), and calculated ionomer film thicknesses for each electrode type are reported in Figure 4.10. Ionomer thicknesses were calculated based on catalyst dispersion weight ratios, measured platinum area, a carbon surface area of 230 $m^2 g^{-1}$, and material densities. Based on the assumption of uniform ionomer distribution over the carbon and platinum, for I/C electrodes below 0.6, a subnanometer coverage is calculated. This type of coverage further probes the nature of transport resistance through the ionomer. It is also observed that for all loadings, below nanometer coverage results in increased mass and specific activities.

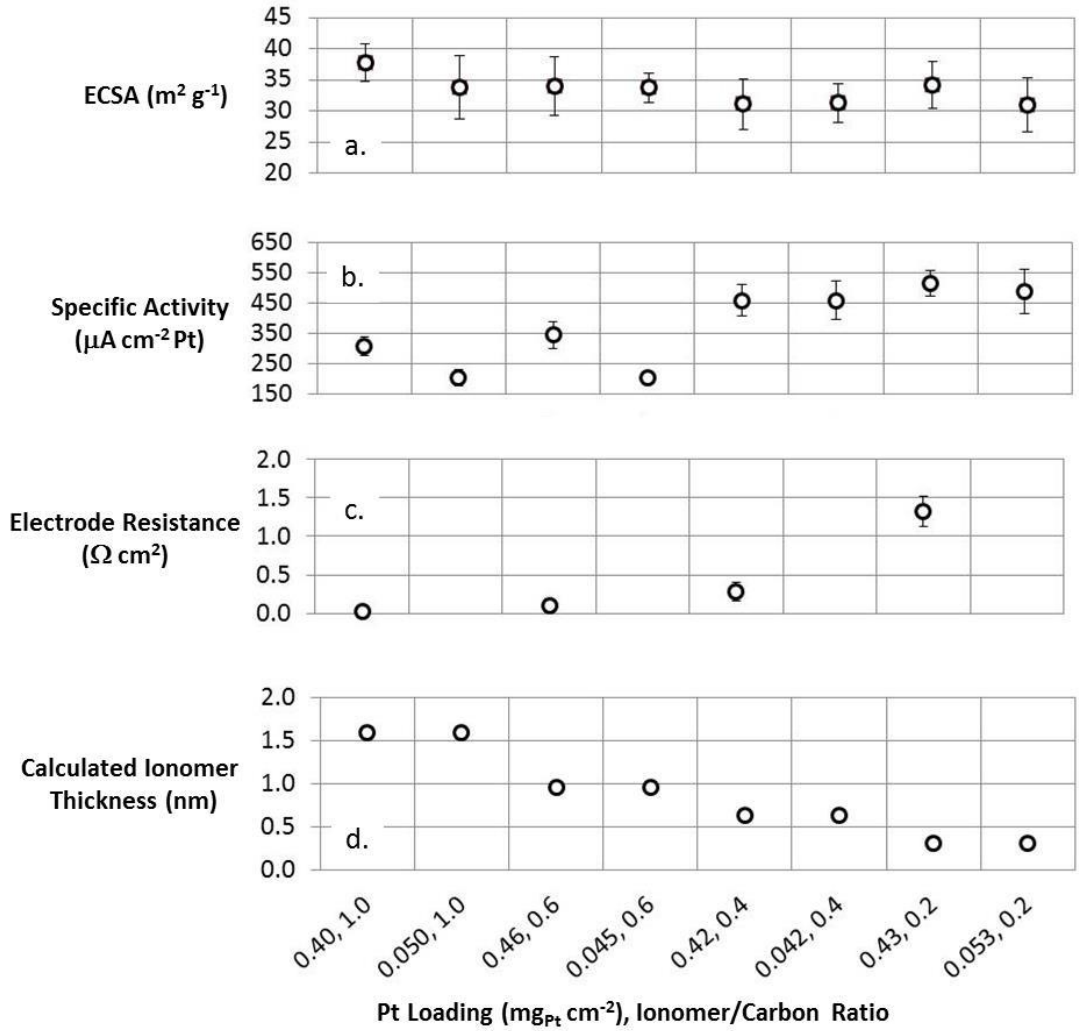

Figure 4.10: Characterization of ionomer thickness samples: a.) electrochemical surface area, b.) specific activity, c.) electrode proton resistance at 75% RH, d.) calculated ionomer thickness. Error bars represent 95% confidence for the mean.

The electrode proton transfer resistances were measured as described by Liu et al. [10] with impedance and a transmission line model. The thickness of the low Pt loaded parts prohibited collection of meaningful impedance data in the frequencies scanned; estimations made by using the sheet resistivity and capacitance of the thicker part predicts a scanning frequency of 40 kHz would be needed to collect data at fully humidified conditions for these thin films. Therefore, for the MEAs used in this work, the sheet resistivity values are only reported for the 0.4 $mg_{Pt}\ cm^{-2}$. Data was also collected at 75%, 50%, and 22% RH to determine viability of the electrode design for varying operating conditions. The electrode resistance was consistent across all I/C ratios at 122% RH ranging from 0.014 to 0.024 ohm cm^2. The variation at 75% RH is shown in Figure 4.10c, where this small decease in water activity causes an

exponential increase in electrode proton resistance as ionomer loading is decreased. These data highlight the practical issues associated with low ionomer content in a typical fuel cell system; however, in this study experiments were executed at high RH to investigate bulk transport through the ionomer. The real component of resistance was measured at 8000 Hz during polarization measurements.

4.2.2 Performance of Varied Ionomer Thickness Samples

Polarization curves for all cathode electrode types with oxygen and air at 95 °C are shown in Figure 4.11. All test conditions outlined in Table 1 were executed for these samples and similar trends to those in Figure 4.11 were observed; however, liquid water in the electrode is mitigated at 95 °C. The oxygen data in Figure 4.11a represents the combined impact of variation in catalyst activity (Figure 4.10b) and protonic resistance in the electrode (Figure 4.11d), as all other parameters are constant (for a given Pt loading). Additional transport loss is considered with air cathode polarization in Figure 4.11b, where a clear improvement in the performance of the low loaded parts occurs with decreasing I/C ratio.

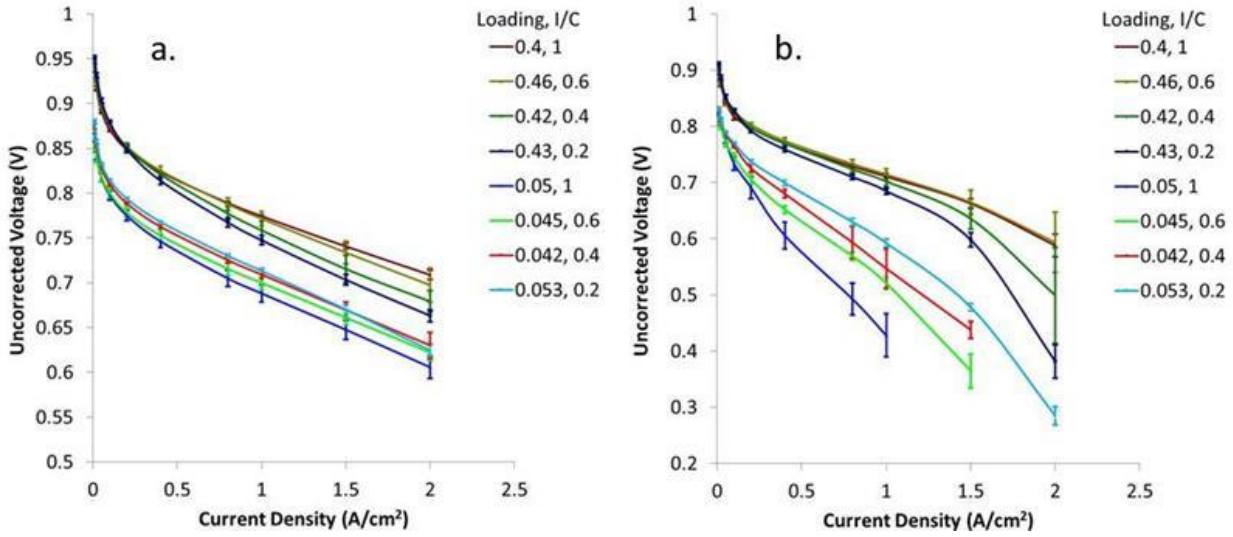

Figure 4.11: Polarization performance of ionomer thickness study samples at 95 °C, 100% RH, a.) pure oxygen cathode feed, b.) air cathode feed. Error bars represent 95% confidence for the mean of 8 experiments.

Next, the data in Figure 4.11 were corrected for ohmic and electrode resistance, and current related to gas cross-over. The remaining kinetic and local transport contribution can be evaluated by normalizing the current density with measured Pt surface area (given in Figure 4.10a) and scaling current logarithmically (Equation 6). In oxygen this analysis, shown in Figure 4.12a, indicates all samples follow

a similar kinetic relationship above 0.7 V. The performance difference between the 0.05 mg_{Pt} cm^{-2} electrodes correlates to the difference in specific activity reported in Figure 4.10b; however, error in the measurements used for voltage corrections will also have a role in deviation from linearity. For oxygen data presented this way, all data should fit a linear model if catalyst activity is constant. The same is true in air if all transport losses are accounted for and if oxide coverage at low potentials does not impact catalyst activity. The data in Figure 4.12b indicate this is not the case for the low Pt electrodes as a significant loss is observed at potentials below 0.7 V. A portion of this loss can be accounted for with reported values for potential dependent kinetics [87], but even with a Tafel slope of 140 mV $decade^{-1}$ there is additional unaccounted loss. Following the analysis in Section 4.1, this loss can be isolated by considering the variation in total transport resistance evaluated with limiting current (Equation 12) as a function of normalized Pt and ionomer area.

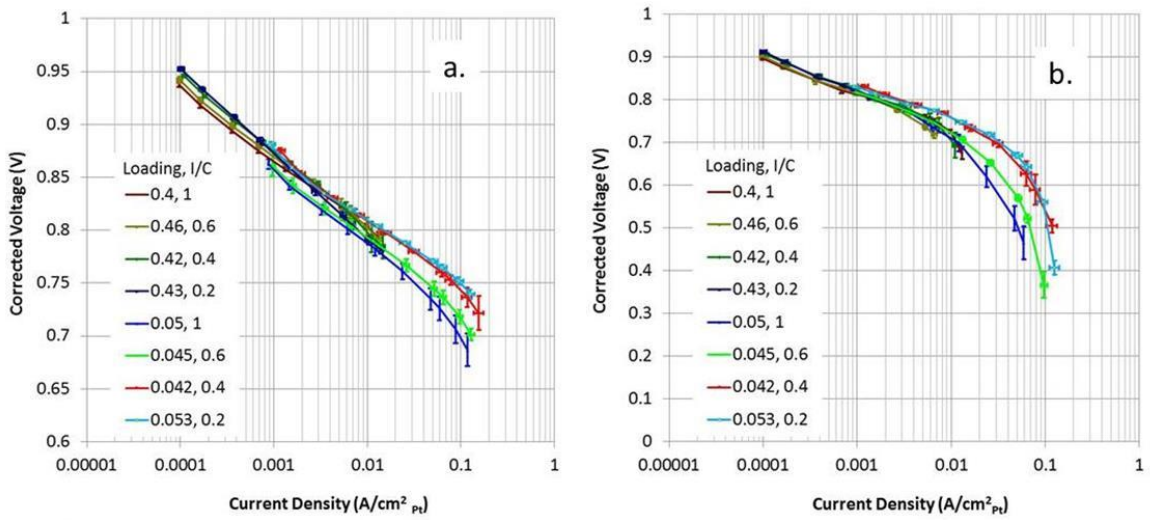

Figure 4.12: Corrected polarization performance of ionomer thickness study samples at 95 °C, 100% RH with current density normalized to measured Pt surface area, a.) pure oxygen cathode feed, b.) air cathode feed. Error bars represent 95% confidence for the mean of 8 experiments.

4.2.3 Transport Resistance Through Ionomer

In Figure 4.13 total oxygen transport resistance is considered as a function of Pt and ionomer surface area to elucidate the local component of transport resistance near the Pt surface per Equations 13 and 45 (Section 4.1.4).

$$R_{O_2}^{P,ind} = R_{O_2}^{Knudsen} + \frac{A_{electrode}}{A_{Pt,surface}} R_{O_2}^{Pt/i} + \frac{A_{electrode}}{A_{Ionomerfilm}} R_{O_2}^{g/i} \approx R_{O_2}^{Knudsen} + \left(\frac{A_{electrode}}{A_{Pt,surface}} + \frac{A_{electrode}}{A_{Ionomerfilm}} \right) R_{O_2}^{local} \quad (45)$$

The local transport resistance is estimated from the variation of total transport resistance between the two loading studied in Figure 4.13. At 0.2 I/C ratio in Figure 4.13a, the variation between loadings is small and the local component to transport resistance is low (1.1 s cm^{-1}) relative to the 1.0 I/C case where the local resistance is 11.0 s cm^{-1}.

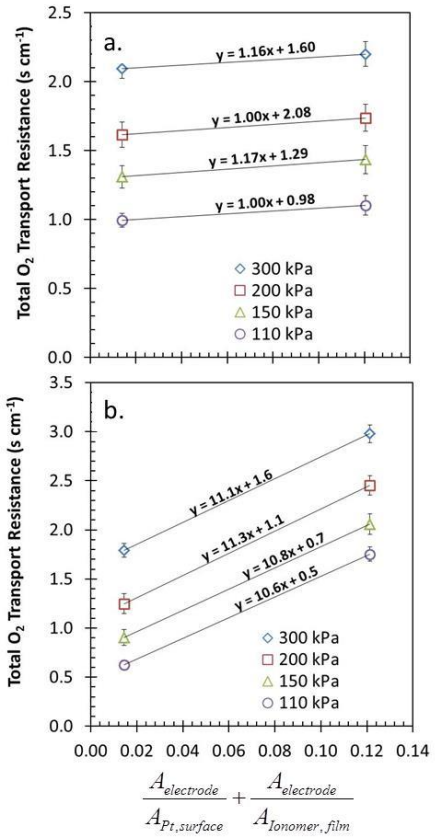

Figure 4.13: Total oxygen transport resistance vs. normalized Pt and ionomer surface area with 0.4 and 0.05 mg_{Pt} cm^{-2} loading, a.) 0.2 I/C ratio, b.) 1.0 I/C ratio. Error bars represent 95% confidence for the mean of 3 experiments.

The oxygen transport resistance through the ionomer film must now be considered with the simplified model developed in Section 4.1. With this model, interfacial transport resistance at the ionomer and Pt interface was shown to account for local transport near the Pt surface in various electrode dispersions. The relationship in Figure 4.9b is reexamined with these data resulting from an ionomer thickness study with dispersion held constant in Figure 4.14. The data at 1.0 and 0.6 I/C correlate well with the interfacial resistance model. However, at 0.2 and 0.4 I/C this model overpredicts the measured data. If uniform coverage of ionomer is assumed, this deviation is likely related to a structural change in the polymer as the thickness is decreased. Although researchers have shown the chemical environment in these films is consistent with decreasing thickness [136] [137], to date there are no data available for catalyst inks with less than 1.0 I/C content. At this length scale, these films will likely consist of a single monolayer in which the polymer is more constrained.

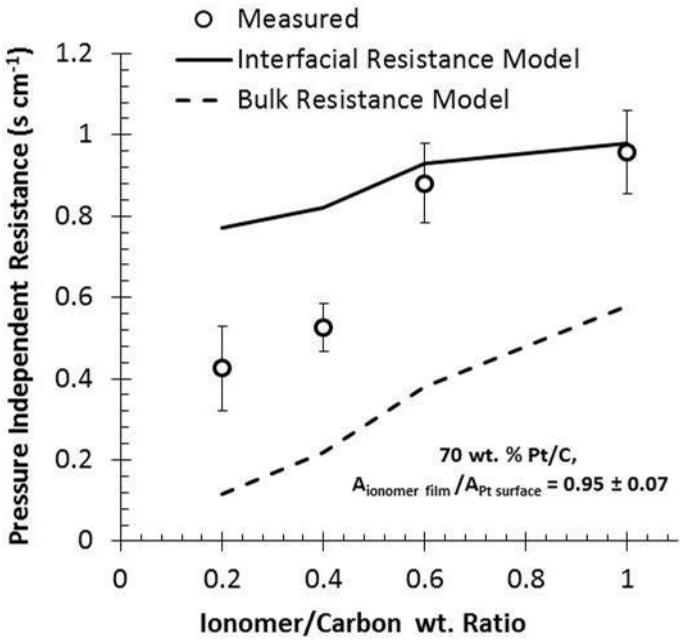

Figure 4.14: 70 wt.% Pt/C dispersion used in ionomer thickness study compare with ionomer transport model developed in Section 4.1.

The thickness of a monolayer of Nafion varies in the literature; Bertoncello measured monolayer thickness Langmiur-Schaefer films via AFM to be 1.3 nm [137]. Neutron reflectivity data of Nafion films produced by spin casting yielded similar results [138] . Modelling of Nafion on spheres of polystyrene yielded monolayer estimation of 2.75 nm [139], which is based on the backbone of the material bending

in half to allow sidechains to adsorb adjacent to each other and extending outward from the styrene spheres. We have assumed a uniform coverage of Nafion over both platinum and carbon black in our thickness calculations. This is based on materials density, electrode geometry and material surface areas with no assumption regarding packing densities, polymer conformation, or sterics.

If the ionomer film was not uniform throughout the catalyst layer, the data in Figure 4.14 suggest that the patchiness becomes pervasive at I/C ratios less than 0.6. However, the ionomer sheet resistivity, calculated from the data in Figure 4.10c with the measured electrode thickness given in Table 7, follows a consistent trend that is similar to that observed by other researchers [10]. Comparing this to the local oxygen transport resistance through the ionomer, Figure 4.15 indicates the step change observed is only related to oxygen transport and there is suitable connectivity in the layer. Figure 4.15 also serves to highlight the practical trade-offs related to fuel cell systems. In the current state-of-the-art, a robust operating range with low proton resistance can only be accomplished with ionomer content that increases oxygen transport resistance.

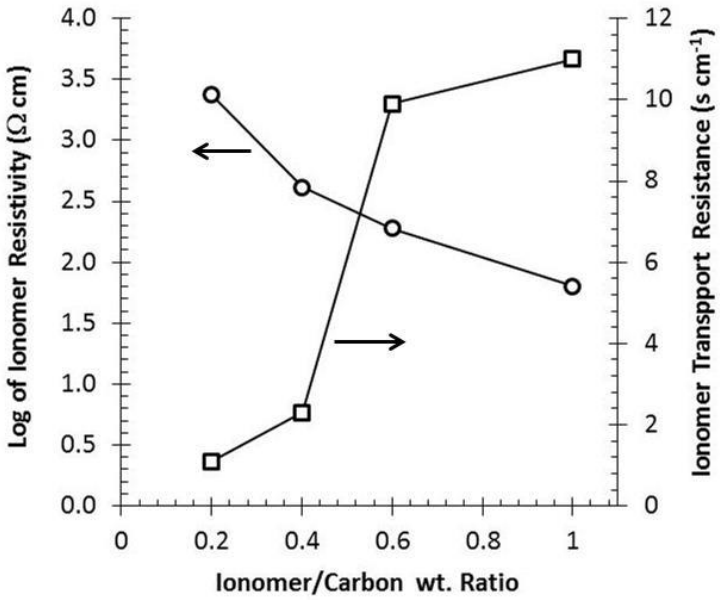

Figure 4.15: Electrode ionomer sheet resistivity at 75% RH compared with local transport resistance through the ionomer ($R_{O_2}^{local}$ in Equation 45).

5. Conclusions

Oxygen transport in the macroporous gas diffusion layer of a PEFC operating under saturated conditions was investigated. The relationship between liquid water content and membrane proton transport resistance first demonstrated that liquid water is required for optimal performance. Next, the water balance and removal of accumulated water was investigated. From these results a novel material was developed to passively shift the water balance toward the cathode where the system can handle it more effectively. For accurate prediction of transport loss through GDL materials, a relationship for the bulk diffusion resistance as a function of saturation was validated using a unique experimental approach that isolated the key parameters involved.

Local oxygen transport resistance near the Pt surface in dispersed fuel cell electrodes was studied with a novel experimental campaign. Platinum nanoparticle dispersions were varied and studied by performance and limiting current methods. Results show that significant performance loss is realized with increased Pt particle density at a given Pt loading and the total transport resistance trends accordingly. Results also indicate that this transport resistance is related not only to the actual Pt surface area but also the surface area of ionomer that covers the Pt and the carbon that surrounds it. The physical origin of this transport resistance through a thin film of ionomer was further investigated by modeling limiting current at a single Pt particle. Comparing the model to the experimental data revealed that an interfacial transport resistance at the gas and Pt interface must be prominent to account for the observed trend as wt.% of Pt/Vulcan increases.

Additional experiments varying ionomer thickness in dispersed electrodes were used to evaluate the interfacial resistance model. Results show the model is valid for I/C ratios above 0.6. A drastic reduction in oxygen transport resistance was observed for lower I/C ratios where thickness approaches a monolayer. It is hypothesized that these thinner films are structurally different and this changes the physical nature of the interfacial resistance observed in thicker films. For ionomer film thicknesses with a reasonable proton resistivity, these experiments and analysis demonstrate that oxygen transport resistance through the ionomer coating is a function of both Pt surface area and Pt particle dispersion. Practically, this work has shown that local oxygen transport loss can be mitigated with electrode design, where oxygen flux through the gas/ionomer interface to the Pt surface must be minimized.

Works Cited

[1] Y. Wang, K. S. Chen, J. Mishler, S. C. Cho and X. C. Adroher, *Applied Energy,* vol. 88, no. 4, pp. 981-1007, 2011.

[2] H. A. Gasteiger, W. Gu, R. Makharia, M. F. Mathias and B. Sompalli, "Beginning-of-Life MEA Performance – Efficiency Loss Contributions," in *Handbook of Fuel Cells – Fundamentals, Technology and Applications*, New York, John Wiley & Sons, 2003, pp. 593-610.

[3] J. P. Owejan, T. A. Trabold, J. J. Gagliardo, D. L. Jacobson, R. N. Carter, D. S. Hussey and M. Arif, *Journal of Power Sources,* vol. 171, pp. 626-633, 2007.

[4] S. He, S. H. Kim and M. M. Mench, *Journal of the Electrochemical Society,* vol. 154, pp. B1024-B1033, 2007.

[5] M. L. Perry, T. W. Patterson and C. Reiser, *ECS Transactions,* vol. 3, pp. 783-795, 2006.

[6] M. M. Mench, Fuel Cell Engines, New York: Wiley, 2008.

[7] W. Gu, D. R. Baker, Y. Liu and H. Gastieger, in *Handbook of Fuel Cells: Fundamentals, Technology, Applications*, New York, John Wiley & Sons, Ltd., 2009.

[8] M. Mathias, J. Roth, J. Fleming and W. Lehnert, in *Handbook of Fuel Cells: Fundamentals, Technology, Applications.*, New York, John Wiley & Sons, Ltd. , 2003.

[9] A. El-Kharouf, T. J. Mason, D. J. L. Brett and B. G. Pollet, *Journal of Power Sources,* vol. 218, pp. 393-404, 2012.

[10] Y. Liu, M. W. Murphy, D. R. Baker, W. Gu, C. Ji, J. Jorne and H. A. Gasteiger, *ECS Transactions,* vol. 11, no. 1, pp. 473-484, 2007.

[11] R. Jiang, C. K. Mittelsteadt and C. S. Gittleman, *Journal of the Electrochemical Society,* vol. 156, no. 12, pp. B1440-B144, 2009.

[12] T. A. Zawodzinski Jr., C. Derouin, S. Radzinski, R. J. Sherman, V. T. Smith, T. Springer and S. Gottesfeld, *Journal of the Electrochemical Society,* vol. 140, no. 4, pp. 1041-1047, 1993.

[13] K. C. Neyerlin, W. Gu, J. Jorne, A. Clark Jr. and H. A. Gasteiger, *Journal of the Electrochemical Society,* vol. 154, no. 2, pp. B279-B287, 2007.

[14] M. Eikerling and A. A. Kornyshev, *Journal of Electroanalytical Chemistry,* vol. 475, no. 107, 1999.

[15] N. Zamel and X. Li, *Progress in Energy and Combustion Science,* vol. 39, no. 1, pp. 111-146, 2013.

[16] Y. Wang, K. S. Chen, J. Mishler, S. C. Cho and X. C. Adroher, *Applied Energy,* vol. 88, no. 4, pp. 981-100, 2011.

[17] J. Yablecki, J. Hinebaugh and A. Bazylak, *Journal of the Electrochemical Society,* vol. 159, no. 12, pp. F805-F809, 2012.

[18] G. Q. Xu, J. M. LaManna, J. T. Clement and M. M. M., *Journal of Power Sources ,* p. submitted, 2013.

[19] D. R. Baker, D. A. Caulk, K. C. Neyerlin and M. W. Murphy, *Journal of the Electrochemical Society,* vol. 156, no. 9, pp. B991-B1003, 2009.

[20] M. Koz and S. G. Kandlikar, *Journal of Power Sources,* vol. 243, pp. 946-957, 2013.

[21] J. M. Sergi and S. G. Kandlikar, *International Journal of Hydrogen Energy,* vol. 36, no. 19, pp. 12381-12392, 2011.

[22] M. J. Martínez, S. Shimpalee and J. W. Van Zee, *Journal of the Electrochemical Society,* vol. 156, no. 1, pp. B80-B85, 2009.

[23] T. Rosén, J. Eller, J. Kang, N. I. Prasianakis, J. Mantzaras and F. N. Büchi, *Journal of the Electrochemical Society,* vol. 159, no. 9, pp. F536-F544, 2012.

[24] G. Unsworth, L. Dong and X. Li, *AIChE Journal,* vol. 59, no. 4, pp. 1409-1419, 2013.

[25] D. A. G. Bruggeman, *Annalen der Physik (Leipzig) ,* vol. 24, pp. 636-664, 1935.

[26] M. J. Martínez-Rodríguez, T. Cui, S. Shimpalee, S. Seraphin, B. Duong and J. W. Van Zee, *Journal of Power Sources,* vol. 207, pp. 91-100, 2012.

[27] D. Malevich, E. Halliop, B. A. Peppley, J. G. Pharoah and K. Karan, *Journal of the Electrochemical Society,* vol. 156, no. 2, pp. B216-B224, 2009 .

[28] J. Fairweather, D. Spernjak, R. Mukundan, J. Spendelow, K. Artyushkova, P. Atanassov, D. Hussey, D. Jacobson and R. L. Borup, *ECS Transactions,* vol. 41, no. 1, pp. 337-348, 2011.

[29] D. A. Caulk and D. R. Baker, *Journal of the Electrochemical Society,* vol. 157, no. 8, pp. B1237-B1244, 2010.

[30] T. Mashio, A. Ohma, S. Yamamoto and K. Shinohara, *ECS Transactions,* vol. 11, p. 529, 2007.

[31] K. Kudo, T. Suzuki and Y. Morimoto, *ECS Transactions,* vol. 33, p. 1495, 2010.

[32] H. Iden, A. Ohma, K. Yamaguchi and K. Shinohara, *ECS Transactions,* vol. 25, p. 907, 2009.

[33] T. A. Greszler, D. Caulk and P. Sinha, *Journal of the Electrochemical Society,* vol. 159, no. 12, pp. F831-F840, 2012.

[34] S. Ge, X. Li, B. Yi and I. Hsing, *Journal of the Electrochemical Society,* vol. 152, no. 6, pp. A1149-A1157, 2005.

[35] D. T. Hallinan Jr. and Y. A. Elabd, *Journal of Physical Chemistry B,* vol. 113, no. 13, pp. 4257-4266.

[36] D. T. Hallinan, M. G. De Angelis, M. Giacinti Baschetti, G. C. Sarti and Y. A. Elabd, *Macromolecules,* vol. 43, no. 10, pp. 4667-4678, 2010.

[37] P. W. Majsztrik, M. B. Satterfield, A. B. Bocarsly and J. B. Benziger, *Journal of Membrane Science,* vol. 301, no. 1-2, pp. 93-106, 2007.

[38] D. R. Morris and X. Sun, *Journal of Applied Polymer Science,* vol. 50, no. 8, pp. 1445-1452, 1993.

[39] D. Rivin, C. E. Kendrick, P. W. Gibson and N. S. Schneider, *Polymer,* vol. 42, no. 2, pp. 623-635, 2001.

[40] T. E. Springer, T. A. Zawodzinski and S. Gottesfeld, *Journal of the Electrochemical Society,* vol. 138, no. 8, pp. 2334-2342, 1991.

[41] X. Ye and M. D. LeVan, *Journal of Membrane Science,* vol. 221, no. 1-2, pp. 163-173, 2003.

[42] T. A. Zawodzinski Jr., M. Neeman, L. O. Sillerud and S. Gottesfeld, *Journal of Physical Chemistry,* vol. 95, no. 15, pp. 6040-6044, 1991.

[43] Q. Zhao, P. Majsztrik and J. Benziger, *Journal of Physical Chemistry B,* vol. 115, no. 2, pp. 2717-2727, 2011.

[44] D. A. Caulk, A. M. Brenner and S. M. Clapham, *Journal of the Electrochemical Society,* vol. 159, no. 9, pp. F518-F529, 2012.

[45] W. Braff and C. Mittelsteadt, *ECS Transactions,* vol. 16, no. Part 1, pp. 309-316, 2008.

[46] B. S. Pivovar, *Polymer,* vol. 47, no. 11, pp. 4194-4202, 2006.

[47] X. Ye and C. Y. Wang, *Journal of the Electrochemical Society,* vol. 154, no. 7, pp. B676-B682, 2007.

[48] R. Anderson, L. Zhang, Y. Ding, M. Blanco, X. Bi and D. P. Wilkinson, *Journal of Power Sources,* vol. 195, no. 15, pp. 4531-4553, 2010.

[49] R. Banerjee and S. G. Kandlikar, *Journal of Power Sources,* vol. 247, pp. 9-19, 2013.

[50] C. E. Colosqui, M. J. Cheah, I. G. Kevrekidis and J. B. Benziger, *Journal of Power Sources,* vol. 196, no. 23, pp. 10057-10068, 2011.

[51] M. Hossain, S. Z. Islam, A. Colley-Davies and E. Adom, *Renewable Energy,* vol. 50, pp. 763-779, 2013.

[52] L. Cindrella, A. Kannan, J. F. Lin, K. Saminathan, Y. Ho, C. W. Lin and J. Wertz, *Journal of Power Sources,* vol. 194, no. 1, pp. 146-160, 2009.

[53] H. Li, Y. Tang, Z. Wang, Z. Shi, S. Wu, D. Song, J. Zhang, K. Fatih, J. Zhang, H. Wang, Z. Liu, R. Abouatallah and A. Mazza, *Journal of Power Sources ,* vol. 178, no. 1, pp. 103-117, 2008.

[54] J. M. LaManna and S. G. Kandlikar, *International Journal of Hydrogen Energy,* vol. 36, no. 8, pp. 5021-5029, 2011.

[55] R. P. Ramasamy, E. C. Kumbur, M. M. Mench, W. Liu, D. Moore and M. Murthy, *International Journal of Hydrogen Energy,* vol. 33, no. 13, pp. 3351-3367, 2008.

[56] P. P. Mukherjee, Q. Kang and C.-Y. Wang, *Energy and Environmental Science,* vol. 4, no. 2, pp. 346-369, 2011.

[57] Q. Yan, H. Toghiani and J. Wu, *J. Power Sources,* vol. 158, p. 316, 2006.

[58] D. R. Sena, E. A. Ticianelli, V. A. Paganin and E. R. Gonzalez, *J. Electroanal. Chem.,* vol. 476, p. 164, 1999.

[59] K. -H. Choi, D. -H. Peck, C. S. Kim, D. -R. Shin and T. -R. Lee, *J. Power Sources,* vol. 86, p. 197, 2000.

[60] G. J. M. Jansen and M. L. J. Overvelde, *J. Power Sources,* vol. 101, p. 117, 2001.

[61] B. Andreaus and G. G. Scherer, *Solid State Ionics,* vol. 168, p. 311, 2004.

[62] Y. Cai, J. Hu, H. Ma, B. Yi and H. Zhang, *Electrochim. Acta,* vol. 51, p. 6361, 2006.

[63] F. Meier and G. Eigenberger, *Electrochim. Acta,* vol. 49, p. 1731, 2004.

[64] G. Q. Lu, F. Q. Liu and C. -Y. Wang, *J. Power Sources,* vol. 164, p. 134, 2007.

[65] H. Nakajima, T. Konomi and T. Kitahara, *J. Power Sources,* vol. 171, p. 457, 2007.

[66] P. K. Sinha and C. -Y. Wang, *Journal of the Electrochemical Society,* vol. 154, p. B1158, 2007.

[67] P. K. Sinha and C. -Y. Wang, *J. Power Sources,* vol. 183, p. 609, 2008.

[68] J. P. Owejan, J. J. Gagliardo, J. M. Sergi, S. G. Kandlikar and T. A. Trabold, *International Journal of Hydrogen Energy,* vol. 34, p. 3436, 2009.

[69] K. Tajiri, C. -Y. Wang and Y. Tabuchi, *Electrochimica Acta,* vol. 53, p. 6337, 2008.

[70] S. -Y. Lee and e. al., *J. Power Sources,* vol. 180, p. 784, 2008.

[71] X. Yu, M. Pingwen, H. Ming, Y. Baolian and Z. G. Shao, *J. Power Sources,* vol. 188, p. 163, 2009.

[72] R. M. Darling and D. Jayne, *ECS Transactions,* vol. 11, p. 975, 2007.

[73] W. Schmittinger and A. Vahidi, *J. Power Sources,* vol. 180, p. 1, 2008.

[74] P. Rama, R. Chen and J. Andrews, *J. Power and Energy,* vol. 222, p. 421, 2008.

[75] C. A. Reiser, T. Skiba and T. W. Patterson, "Hydrogen passivation shut down system for a fuel cell power plant". Patent WO000039877A1, 2 October 2000.

[76] S. G. Goebel and J. P. Owejan, "Anode water separator for a fuel cell system". Patent 8563182, October 2011.

[77] J. P. Owejan, T. Tighe, T. A. Trabold and J. A. Rock, "Water removal system for non-reactive regions in PEFMC stacks". US Patent 8034502, 11 October 2011.

[78] K. Dan, "Fuel cell system and method of operating the fuel cell system". US Patent 8557457, 15 October 2013.

[79] S. G. Goebel and P. W. H., "Passive Water Drain". US Patent 8431278, 30 April 2013.

[80] J. P. Owejan and S. G. Goebel, "Bipolar plate with reduced coolant volume and asymmetric heat removal". US Patent 8389182, 5 March 2013.

[81] Koenekamp, A., D. Rensink, M. Koch and M. Hahn, "Bidirectional water separator". US Patent 8236456, 7 August 2012.

[82] S. Inai, H. Yoshida, H. Kato, K. Hayashi, R. Jinba, N. Matsumoto, T. Takai and M. Utsunomiya, "Stop method for fuel cell system and fuel cell system". US Patent 8221923, 17 July 2012.

[83] G. Winter, G. Vyas, T. A. Trabold and R. Datta, "Hydrophilic coating for fuel cell bipolar plate and methods of making the same". US Patent 7935381, 3 March 2011.

[84] J. Benzinger and C. H. Woo, "Fuel Cell system and method for controlling current". US Patent 7951501, 31 May 2011.

[85] Y. Wang and C.-Y. Wang, *Electrochim. Acta,* vol. 50, p. 1307, 2005.

[86] A. Kongkanand and P. K. Sinha, *Journal of the Electrochemical Society,* vol. 158, p. B703, 2011.

[87] N. P. Subramanian, T. A. Greszler, J. Zhang, W. Gu and R. Makharia, *Journal of the Electrochemical Society,* vol. 159, p. B531, 2012.

[88] S. K. Dishari and M. A. Hickner, *ACS Macro Letters,* vol. 1, p. 291, 2012.

[89] G. Beaucage, R. Composto and R. S. Stein, *Journal of Polymer Science Part B: Polymer Physics,* vol. 31, p. 319, 1993.

[90] J. A. Forrest and K. Dalnoki-Veress, *Adv. Colloid Interface Science,* vol. 94, no. 167, 2001.

[91] B. Frank, A. P. Gast, T. P. Russel, H. R. Brown and C. Hawker, *Macromolecules,* vol. 29, p. 6531, 1996.

[92] J. L. Keddie, R. A. L. Jones and R. A. Cory, *Faraday Discussions,* vol. 98, p. 219, 1994.

[93] A. Kongkanand, *Journal of Physical Chemistry C,* vol. 115, p. 11318, 2011.

[94] J. A. Dura, V. S. Murthi, M. Hartman, S. K. Satija and C. F. Majkrzak, *Macromolecules,* vol. 42, p. 4769, 2009.

[95] H. S. K. Iden, A. Ohma and K. Shinohara, *Journal of the Electrochemical Society,* vol. 158, p. B987, 2011.

[96] Z. Siroma, R. Kakitsubo, N. Fujiwara, T. Ioroi, S. I. Yamazaki and K. Yasuda, *J. Power Sources,* vol. 189, p. 994, 2009.

[97] J. Peron, D. Edwards, M. Haldane, X. Y. Luo, Y. M. Zhang, S. Holdcroft and Z. Q. Shi, *J. Power Sources,* vol. 196, p. 179, 2011.

[98] D. K. Paul, A. Fraser and K. Karan, *Electrochem. Communications,* vol. 13, p. 774, 2011.

[99] R. Madhusudana Rao and R. Rengaswamy, *J. Power Sources,* vol. 158, p. 110, 2006.

[100] D. Harvey, J. G. Pharoah and K. Karan, *J. Power Sources,* vol. 179, p. 209, 2008.

[101] J. Liu and M. Eikerling, *Electrochim. Acta,* vol. 53, p. 4435, 2008.

[102] M. Secanell, K. Karan, A. Suleman and N. Djilali, *Electrochim. Acta,* vol. 52, p. 6318, 2007.

[103] N. P. Siegel, M. W. Ellis, D. J. Nelson and M. R. Von Spakovsky, *J. Power Sources,* vol. 115, p. 81, 2003.

[104] W. Sun, B. A. Peppley and K. Karan, *Electrochim. Acta,* vol. 50, p. 3359, 2005.

[105] W. Yoon and A. Z. Weber, *Journal of the Electrochemical Society,* vol. 158, p. B1007, 2011.

[106] R. N. Carter, S. S. Kocha, F. T. Wagner, M. Fay and H. A. Gasteiger, *ECS Transactions,* vol. 11, p. 403, 2007.

[107] H. A. Gasteiger, S. S. Kocha, B. Sompalli and F. T. Wagner, *Applied Catalysis B: Environmental,* vol. 56, p. 9, 2005.

[108] J. Zhang, B. Litteer, F. Coms and R. Makharia, *ECS Transactions,* vol. 41, p. 1471, 2011.

[109] J. J. Gagliardo, J. P. Owejan, T. A. Trabold and T. Tighe, *Nuclear Instruments and Methods in Physics Research – Section A,* vol. 605, pp. 115-118, 2009.

[110] T. A. Trabold, J. P. Owejan, J. J. Gagliardo, D. L. Jacobson, D. S. Hussey and M. Arif, "Use of Neutron Imaging for PEMFC Performance Analysis and Design," in *Handbook of Fuel Cells – Fundamentals, Technology and Applications*, Chichester, John Wiley & Sons Ltd., 2009.

[111] D. S. Hussey, D. Spernjak, A. Z. Weber, R. Mukundan, J. Fairweather, E. L. Brosha, J. Davey, J. S. Spendelow, D. L. Jacobson and R. L. Borup, *Journal of Applied Physics,* vol. 112, no. 10, p. 104906, 2013.

[112] R. S. Fu, U. Pasaogullari, T. Shiomi, Y. Tabuchi, D. S. Hussey and D. L. Jacobson, *Journal of the Electrochemical Society,* vol. 159, no. 9, pp. F545-F553, 2012.

[113] U.S. Department of Energy, "U.S. Department of Energy,“Hydrogen, Fuel Cells, and Infrastructure Technology Programs: Multi-Year Research, Development and Demonstration Plan,” Section 3.4 – Fuel Cells," October 2007.. [Online]. Available: http://www1. eere.energy.gov/hydrogenandfuelcells/ mypp/.

[114] D. W. Fultz and P. A. Chuang, *ASME J. Fuel Cell Science and Technology,* vol. 8, pp. 1-6, 2011.

[115] J. P. Owejan, J. J. Gagliardo, R. C. Reid and T. A. Trabold, *Journal of Power Sources,* vol. 209, pp. 147-151, 2012.

[116] K. T. Cho and M. M. Mench, *Journal of Power Sources,* vol. 195, pp. 6748-6757, 2010.

[117] K. T. Cho and M. M. Mench, *Journal of Power Sources,* vol. 195, pp. 3858-3869, 2010.

[118] K. T. Cho and M. M. Mench, *International Journal of Hydrogen Energy,* vol. 35, pp. 12329-12340, 2010.

[119] D. S. Hussey, D. L. Jacobson, M. Arif, P. R. Huffman, R. E. Williams and J. C. Cook, *NIM Section A,* p. 542, 2005.

[120] J. P. Owejan, J. J. Gagliardo, S. R. Falta and T. A. Trabold, *Journal of the Electrochemical Society,* vol. 156, no. 12, pp. B1475-1483, 2011.

[121] E. L. Thompson, J. Jorne, W. Gu and H. A. and Gasteiger, *Journal of the Electrochemical Society,* vol. 155, p. B625, 2008.

[122] O. Myklestad, *International Journal of Heat and Mass Transfer,* vol. 11, p. 675, 1968.

[123] J. P. Owejan, P. D. Nicotera, M. M. Mench and R. E. Evans, "Low cost fuel cell diffusion layer configured for optimized anode water management". US Patent 8518596, 27 August 2013.

[124] J. P. Owjean, T. A. Trabold and M. M. Mench, *International Journal of Heat and Mass Transfer,* p. submitted, 2013.

[125] A. Turhan, S. Kim, M. Hatzell and M. M. Mench, *Electrochimica Acta,* vol. 55, pp. 2734-2745, 2010.

[126] J. Park and X. Li, *Journal of Power Sources ,* vol. 163, no. 2, pp. 853-863, 2007.

[127] M. Khandelwal and M. M. Mench, *Journal of Power Sources,* vol. 161, no. 2, pp. 1106-1115, 2006.

[128] G. He, Y. Yamazaki and A. Abudula, *Journal of Power Sources,* vol. 195, no. 6, pp. 1551-1560, 2010.

[129] D. Kramer, S. A. Freunberger, R. Flückiger, R. A. Schneider, A. Wokaun, F. N. Büchi and G. G. Scherer, *Journal of Electroanalytical Chemistry,* vol. 612, no. 1, pp. 63-77, 2008.

[130] J. Becker, C. Wieser, S. Fell and K. Steiner, *International Journal of Heat and Mass Transfer,* vol. 54, no. 7-8, pp. 1360-1368, 2011.

[131] S. G. Kandlikar, Z. Lu, T. Y. Lin, D. Cooke and M. Daino, *Journal of Power Sources,* vol. 194, no. 1, pp. 328-337, 2009.

[132] J. P. Owejan, J. E. Owejan, W. Gu, T. A. Trabold, T. W. Tighe and M. F. Mathias, *Journal of the Electrochemical Society,* vol. 157, no. 10, pp. B1456-B1464, 2010.

[133] R. B. Bird, W. E. Stewart and E. N. Lightfoot, Transport Phenomena, New York: Wiley, 1960.

[134] Y. Tabuchi, T. Shiomi, O. Aoki, N. Kubo and K. Shinohara, *Electrochimica Acta ,* vol. 56, no. 1, pp. 352-360, 2010.

[135] J. P. Owejan, J. E. Owejan and W. Gu, *Journal of The Electrochemical Society,* vol. 160, no. 8, pp. F824-F833, 2013.

[136] C. Sun, K. L. More and T. A. Zawodzinski, *ECS Transactions,* vol. 33, no. 1, pp. 1207-1215, 2010.

[137] P. Bertoncello, M. K. Ram, A. Notargiancomo, P. Ugo and C. Nicolini, *Phys. Chem. Chem. Phys.,* vol. 4, pp. 4036-4043, 2002.

[138] P. Bhargava, "NIST Center for Neutron Research," 15 September 2009. [Online]. Available: http://www.ncnr.nist.gov/programs/CHRNS/pdf/HSI09_Bhargava.pdf. [Accessed 27 February 2014].

[139] L. Zook, M. D. DeJohn and J. Leddy, "Aggregation of ionomer and carbon black during MEA preparation: A model to characterize particle size and catalyst accessibility," in *Proton Conducting Membrane Fuel Cells II: Proceedings of the Second International Symposium on Proton Conducting Membrane Fuel Cells II*, Pennington, The Electrochemical Society, Inc., 1999, pp. 10-19.

Vita

Jon Patrick Owejan was born in Middletown, NY on January 11th, 1979, to Thomas and Maureen Owejan. He graduated from Churchville-Chili High School in 1997 and began undergraduate studies at Rochester Institute of Technology in mechanical engineering. As part of his BS degree, he completed several co-op appointments at NASA's Johnson Space Center in robotics, space tool development, and failure analysis. After completing his BS degree in 2002, he continued his studies at Rochester Institute of Technology focusing on neutron imaging methods for quantification of liquid in operating fuel cells. Upon completing his MS degree in 2004, he joined the General Motors Electrochemical Energy Research Laboratory. There he led electrochemical transport research and served as the Principle Investigator on government sponsored lithium-ion battery and fuel cell projects. He joined Dr. Matthew Mench's Group in the Electrochemical Energy Storage and Conversion Laboratory at the University of Tennessee in 2010 to continue fundamental transport studies. He graduated with his PhD in 2014. He is currently an Assistant Professor in the Mechanical Engineering Technology Department at Alfred State College. He married Jeanette Elizabeth in November 2006 with whom he has two children: Benjamin and Seth.